Numerical Modelling For Diesel Spray Combustion

XiaoHang (Leo) Fang

Exeter College

University of Oxford

A thesis submitted for the degree of

Doctor of Philosophy

Trinity 2019

This thesis is dedicated to
mom and dad
for their endless love, support and encouragement

Acknowledgements

First and foremost, I would like to thank my supervisor, Dr Martin Davy, for giving me the opportunity to work on this project. His constant support and guidance was the key to the success of my study. I would also like to thank Prof. Richard Stone and Dr Joseph Camm for their help at various point of my PhD.

I would like to express my sincere gratitude to my undergraduate supervisor and good friend Prof. Kendal Bushe. None of this would have happened if I had not followed his candid advice. The profound knowledge he has shared with me both in research and career development has helped me with every step of my study. I will be forever grateful to him.

I am very appreciative of the financial support that the COSF, GBCC and the Henry Lester Trust provided me for my stay in Oxford.

I would like to thank the members of the Oxford Combustion and Engines Group, Dr Ben Williams, Dr Chris Willman and Dr Felix Leach and colleagues in the group, Dr Nick Papaioannou, Dr Blane Scott and Dr Riyaz Ismail, who are my great friends and made this journey ever memorable. I will forever cherish all the memories from Cowley where we shared failure, success and the future.

I would also like to thank all my friends back in China and Canada. A special thanks go to Ula for hearing all my stress, complains and happiness over the past three years. Thank you for being with me on this amazing journey.

Last but not least, I want to extend my greatest gratitude to my parents. I want to thank you for always understanding the things I said, the things I didn't say, and the things I never planned on telling you. Thank you for understanding me always. Nothing in my life would have been without your strife. Nothing I can say, can ever truly convey. Nothing that I do can show my gratitude for you. Mom and Dad, you are, the best parents ever.

Abstract

Diesel engines are widely known for their high thermal efficiency, high torque, reliability, durability, fuel economy, and low carbon dioxide emissions in various industrial applications, such as power generation, mass transportation and off-road applications. However, the combination of a stratified air-fuel mixture and a non-premixed flame gives rise to nitrogen oxides (NOx) and particulate matter (PM) emissions for diesel combustion. Studies have shown that diesel engines can achieve very low NOx and PM emissions at high efficiency through the use of a range of low-temperature combustion (LTC) strategies and this thesis seeks to investigate the turbulent mixing influence on spray atomization and combustion processes encountered in compression ignition diesel engines under low temperature conditions. Recent studies indicate that end-of-injection (EOI) processes may support ignition recession back to the injector nozzle, thereby helping to reduce emissions. The first part of the thesis contributes to the physical understanding of this EOI phenomenon, combustion recession, using computational fluid dynamics studies at LTC conditions. Simulations are performed on a single-hole injection of n-dodecane under a range of the Engine Combustion Network's (ECN) "Spray A"conditions. The primary objective of this part is to assess the ability of a Flamelet Generated Manifold (FGM) combustion model in predicting and characterizing the combustion recession. All simulations are performed under the Reynolds-Averaged Navier-Stokes (RANS) framework in a grid-converged Lagrangian spray scenario. The simulation of combustion recession is qualitatively validated against experimental data from the literature, and the efficacy of each model in predicting combustion recession is evaluated. Overall, it was found that the FGM model was able to capture the combustion recession phenomenon well — showing particular strength in predicting distinct auto-ignition events in the near nozzle region.

Following the validation of the FGM model in predicting combustion recession, the importance of the chosen chemical mechanism in predicting diesel fuel spray combustion is also investigated. Studies were again performed under the RANS framework using the Flamelet Generated Manifold (FGM) model with four different chemical mechanisms for n-dodecane that are commonly used in the engine simulation communities - including recently developed reduced chemistry mechanisms.

The flamelet database for each of the chemical mechanism is generated using two distinct methods: 0D homogeneous reactor (HR) ignition flamelets and 1D igniting counterflow diffusion (ICDF) flamelets. The effect of different tabulation approaches is investigated first following the discussion of the impact of chemical mechanisms on the prediction of combustion recession. Further discussions include an evaluation of the performance of the chemical mechanisms in predicting the most relevant reacting spray characteristics compared to the ECN experimental database: ignition delay time (IDT), flame lift-off length (LOL) and the flame reactive region. Results show that the choice of both the tabulation method and chemical mechanism plays a significant role in initial flame stabilization and end of injection (EOI) transient processes. In general, both tabulation techniques were able to qualitatively capture the flame characteristics before EOI; however, ICDF tabulation is better suited for the FGM approach in order to capture the combustion recession. Furthermore, the chemical mechanisms studied indicate that mechanisms with stronger low temperature chemistry predictions are more likely to promote combustion recession under an FGM framework.

In addition, a novel combustion modelling approach is proposed here to further study the transient effects of diesel spray. Conditional Source-term Estimation (CSE) is a combustion model which invokes the Conditional Moment Closure (CMC) hypothesis to provide an approximation of the mean chemical source term in an averaged transport equation. Unlike CMC, where transport equations are solved for conditional moments, CSE recovers these conditional moments through the solution of an inverse problem. Integral equations are inverted for the conditional moments, by assuming spatial homogeneity in the conditional averages where Tikhonov regularization is applied. Previous CSE studies have shown that the model is able to predict the flame characteristics successfully for both premixed and non-premixed combustion modes. However, most of these investigations were based on methane flames. This study will be the first CSE application to a complex hydrocarbon fuel, n-dodecane, under the Engine Combustion Network's (ECN) "Spray A" conditions. Detailed chemistry is included in tabulated form using the Flamelet Generated Manifold (FGM) methodology. The predictions of this study include both the Favre averaged conditional mass fraction of reactive species and temperature. The results are compared with available experimental data and previous numerical results. Both RANS and LES simulations are performed under the same condition. The objectives of this part of the thesis are (i) assessment of the application of CSE on igniting diesel spray (ii) comparison of the CSE numerical results with available experimental results and previous numerical simulations. Overall, the combination of a chemical mechanism that has been tuned to predict "Spray A" conditions with the CSE-FGM model is able to successfully predict autoignition delay time and lift-off length of n-dodecane spray within the scatter of the experimental data. CSE-FGM offers a feasible tool for detailed combustion analysis of diesel spray flames. Both RANS and LES can give reasonably good global predictions of the flame. The LES approach is more data-rich, given the opportunity to explore more local and unsteady phenomenon present in a transient diesel jet.

Contents

List of Figures

List of Tables

List of Abbreviations

AMR	Adaptive Mesh Refinement
ASI	After Start of Injection
ASoR	After Start of Ramp Down
CFD	Computational Fluid Dynamics
CSE	Conditional Source-term Estimation
CMC	Conditional Moment Closure
DNS	Direct Numerical Simulation
EBU	Eddy Break Up Model
ECN	Engine Combustion Network
EGR	Exhause Gas Recirculation
EOI	End of Injection
FGM	Flamelet Generated Manifold Model
FPI	Flame Prolongation of ILDM
HCCI	Homogeneous Charge Compression Ignition
HR	Homogeneous Reactor
IDT	Ignition Delay Time
ICDF	Igniting Counterflow Diffusion
ILDM	Intrinsic Low Dimensional Manifold
KHRT	Kelvin-Helmholtz Raleigh-Taylor
LFM	Lagarangian Flamelet Model
LOL	Lift-Off Length
LTC	Low Temperature Combustion
NTC	No Time Counter Model
ODE	Ordinary Differential Equation
PDF	Probablity Density Function

PIV	Particle Image Velocimetry
PLIF	Planar Laser-induced Fluorescence
PM	Particular Matter
RANS	Reynold-Averaged Navier-Stokes
ROI	Rate Of Injection
RIF	Representative Interactive Flamelet Model
SLFM	Stationary Laminar Flamelet Model
TCI	Turbulent Chemistry Interaction
TGLDM	Trajectory Generated Low Dimensional Manifolds
TKE	Turbulent Kinetic Energy
UHC	Unburned Hydrocarbon
ULFM	Unsteady Laminar Flamelet Model
WSR	Well-Stirred Reactor
a	Strain rate
C	Progress variable
D	Molecular diffusion coefficient
F	Body force
h	Enthalpy
$\mathscr{J}$	Species molecular diffusive flux
K	Stretch rate
Le	Lewis number
Nu	Nusselt number
P_{amb}	Ambient pressure
P_{inj}	Fuel injection pressire
Pr	Prandtl number
Re	Reynolds number
Sc	Schmitt number
Sh	Sherwood nummber
Z	Mixture fraction
δ_{ij}	Kronecker operator
μ	Dynamic viscosity

μ_t	Turbulent viscosity
ρ	Density
ρ_{amb}	Ambient density
τ_{ij}	Viscous stress tensor
χ	Scalar dissipation rate
$\dot{\omega}_k$	Reaction rate of species k

Thermodynamics is a funny subject. The first time you go through it, you don't understand it at all. The second time you go through it, you think you understand it, except for one or two small points. The third time you go through it, you know you don't understand it, but by that time you are so used to it, it doesn't bother you any more.

— Arnold Sommerfeld

1

Introduction

Contents

1.1 Motivation

Diesel engines are widely known for their high thermal efficiency, high torque, reliability, durability, fuel economy, and low carbon dioxide emission in various industrial applications, such as power generation, mass and passenger transportation and off-road applications. However, diesel engines emit high levels of NOx (oxides of nitrogen) emission caused by high localized temperature and PM (particulate matter) emissions due to their combustion with heterogeneous air-fuel mixtures. Because of ever-tightening emission legislations, researchers are now looking into different spray combustion strategies, as the spraying and combustion of liquid fuel jets are the primary means of producing power and also forming engine-related emissions.

One of the solutions to achieve very low NOx and PM emissions at high efficiency in compression-ignition engines is to use low-temperature combustion (LTC) strategies. Some in-cylinder solutions used in LTC include homogeneous charge compression ignition (HCCI) combustion [49], early injection with exhaust-gas recirculation (EGR), as well as late injection with EGR and high swirl [60]. By introducing cooled exhaust gas recirculation, the adiabatic flame temperature is kept under the thermal NOx temperature region, and the soot formation is decreased [66]. In HCCI combustion, pre-combustion mixing is enhanced, reducing the in-cylinder formation of both PM and NOx. Through years of research, these in-cylinder approaches are beginning to be adopted by modern diesel engines to further decrease emissions, particularly at low to medium load conditions. Although LTC strategies have shown promising results in reducing NOx and PM emissions, there is also evidence showing that they can increase some other pollutants including those of unburned hydrocarbons (UHC) - especially in low load operating conditions. In order to further reduce pollutant emissions, comprehensive experiments and modelling have been conducted on reacting diesel spray characteristics. Naber and Siebers [88] studied the effects of ambient gas density and fuel vaporization on the penetration and dispersion of diesel sprays. Nishimura *et al.* [92] examined the effects of fuel injection rate on emissions reduction. Siebers and Higgins [132] studied ambient gas temperature and density as well as injection pressure effects on flame lift-off length. The majority of these studies consider only the start of injection (SOI) and the quasi-steady injection processes as they are considered critical to soot and NOx formation. Historically, significantly less work has considered the end of injection (EOI) processes. However, recent studies have shown that EOI processes also play an important role in diesel engine emissions regardless of their combustion or injection timing strategies. EOI processes have been found to enhance ambient gas entrainment into the fuel spray [86] which is specifically linked to hydrocarbon emissions for both conventional combustion [170] and LTC strategies [87]. EOI processes have also been shown to alter soot formation/oxidation processes as well as carbon monoxide (CO) oxidation kinetics [63]. EOI processes are unsteady and complicated, including multiphase flow, turbulent mixing, chemical kinetics and different combustion phenomena, therefore making it a difficult field to study. With advanced experimental and modelling techniques, different EOI processes are being discovered, and their roles in compression ignition engines become clearer.

One of the EOI processes that was found to be closely linked to the combustion and emission outcomes is injection ramp-down (the rate at which fuel flow is decreased through nozzles) [63]. Musculus and Kattke [86] have shown that a faster injection ramp-down rate could cause greater ambient gas entrainment which forms leaner mixtures near injector more rapidly. This increased entrainment of ambient gas after EOI is known as an "entrainment wave". A detailed study on entrainment wave behaviour shows that it can reduce the jet penetration rate, which could be useful for limiting fuel impingement. With more fuel-lean mixtures in the jet after the passage of the entrainment wave, soot formation is reduced or even eliminated - especially upstream of the jet. On the other hand, the fuel-air mixture may become over-mixed (beyond the flammability limit) which can be detrimental to UHC and CO emissions. The overly lean fuel-air mixture caused by the entrainment wave may reach first-stage ignition forming formaldehyde and other partially oxidized species, it may not achieve second stage ignition which could further increase UHC emissions. In order to reduce these UHC emissions, Knox *et al.* [64] used a controlled ramp-down rate of injection to promote second stage ignition near the injector. The mechanism used to reduce UHC emissions near the injector under these conditions was termed as "combustion recession".

1.1.1 Combustion Recession

The existence of combustion recession was first identified as the end of injection "flashback", where the reaction zone of the lifted flame propagates upstream to the injector [87][12]. Under high-temperature conditions (HTC) such "flashback" also appears in soot luminosity movies when ignition occurs before EOI. As shown in the bottom half of Figure 1.1, under certain conditions, second stage ignition reactions are observed to propagate back to the near nozzle region despite locally enhanced mixing by the entrainment wave. As multiple research groups observed this process, more interesting findings were disclosed. The early identification of this process as "flashback" is likely due to its similarity to lifted-flame phenomenon in gas turbines. Later, when Sandia National Laboratories used planar laser-induced fluorescence (PLIF) and high-speed schlieren imaging to study low and high-temperature autoignition events in a high-pressure n-dodecane spray, it was also observed that high-temperature ignition appears to propagate back to the near nozzle region [134]. From schlieren imaging, however, the rate at which a high-temperature ignition front propagates back to the nozzle exceeds any physically reasonable flame speed. Therefore this process should not be considered as a flashback by flame propagation. Instead, combustion recession is used as a more generic term for this particular phenomenon.

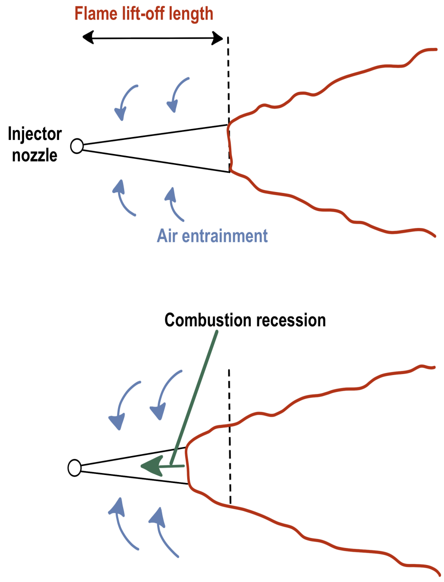

Figure 1.1: Schematic of combustion recession, adapted from [64].

With the help of advanced optically accessible engines, more experimental investigations were performed to understand the physics behind combustion recession. Koci *et al.* [65] discovered that the shape of EOI, or more specifically the deceleration of EOI, is critical to the existence of combustion recession. For a given ambient condition, the strength of combustion recession was found to be inversely ordered by EOI deceleration. Using a reduced-order model Knox *et al.* [64] showed how a controlled ramp-down rate of injection could enhance the likelihood of combustion recession for conditions that would not otherwise exhibit combustion recession. The model predicts that a longer EOI transient duration could promote the existence of combustion recession. Later Knox *et al.* [63] used simultaneous high-speed optical diagnostics to validate the effects of EOI transients on combustion recession predicted by the model. The experiments revealed that at high temperatures and/or high oxygen concentrations longer EOI transients could promote soot recession. Therefore a trade-off between UHC and soot emissions needs to be considered. Although many experimental results have shown the existence of combustion recession, there are only a limited number of numerical studies regarding this phenomenon presented in the literature. As discussed earlier, EOI processes are unsteady and complicated. Knox *et al.*'s model successfully interpreted the experimental trends; however, it is not capable of providing quantitative results compared to the experiment. Moreover, the model only focused on negative ignition dwell conditions where a quasi-steady lift-off length is established prior to EOI. More recently, Blomberg *et al.* investigated the split injection of “Spray A” from the Engine Combustion Network (ECN) using two different turbulence models (RANS and LES) in conjunction with a conditional moment closure (CMC) combustion model [19]. RANS-CMC did not capture full combustion recession towards the upstream nozzle location after the first injection; whereas LES-CMC showed accurate predictions of combustion recession. Although these models were able to capture the combustion recession phenomenon, the controlling parameters of combustion recession were not discovered through the modelling. It is clear that considerable future research is needed, both numerically and experimentally, in order to gain a better understanding of this important phenomenon.

1.2 Objectives

Increasing computational power has made numerical modelling more popular over the past few years. Advanced computational fluid dynamics models enabled us to describe many complex phenomena (such as combustion recession) occurring in diesel engine combustion. However, the present understanding of EOI diesel combustion processes is still limited, and further investigation is needed to better represent these processes numerically.

In this study, different combustion models are explored in order to better predict combustion recession. All models are interfaced with a well-established commercial three-dimensional flow field solver, an approach which allows for the inclusion of detailed chemistry in the simulation of turbulent reacting flows at a reasonable computational cost. The ability to include detailed chemistry forms the basis for quantitative pollutant formation predictions, although pollutant predictions are outside the current project scope. As coupled models are applied to investigate auto-igniting liquid fuel sprays, detailed chemistry is a prerequisite for the accurate description of the ignition processes. The performance and validity of the method employed are tested on the one hand by investigating the influence of air temperature on the ignition delays at diesel engine relevant conditions, for which experimental data from a high pressure and temperature open combustion chamber has been reported. Numerical results are further compared with experimental data gathered from an optically accessible, constant volume closed high-temperature high-pressure chamber, for which the comprehensive set of validation data comprises liquid and gas phase spray penetration, ignition delay and location as well as a pressure signal, indicative of the combustion generated heat release. Furthermore, with respect to the physical mechanisms concerning the interaction between the turbulent flow field and the flame, the study seeks to develop a deeper understanding and identification of the governing parameters and processes in this modelling approach relating to the turbulence-chemistry interaction.

1.3 Thesis Overview

A brief overview of the thesis is provided in the following section. The thesis consists of eight chapters that cover the numerical methods for turbulent reacting spray modelling (Chapter 2 and 3), the discussion of non-reaction spray modelling (Chapter 4), the application of currently available combustion models on diesel combustion under engine relevant conditions (Chapter 5) and the influence of chemical mechanism on the prediction of combustion recession (Chapter 6) and the novel combustion modelling approach developed in this study (Chapter 7). Each chapter begins with a short introduction and some current literature discussion.

Chapter 2 and 3 will summarize the numerical methods used to describe turbulent reacting flows. Chapter 2 focuses on the governing equations for both single and two-phase flows, while Chapter 3 gives a detailed overview of different approaches in combustion modelling. A brief description of spray modelling will also be presented

Chapter 4 studies the effect of sub-models on non-reaction spray predictions. The modelling process and final results are discussed in detail. The chosen model will be used for the following reacting spray studies.

Chapter 5 assesses the ability of a Flamelet Generated Manifold (FGM) combustion model to predict and characterize combustion recession. First, a baseline condition FGM simulation is compared with two other combustion models, namely the well-stirred reactor model (WSR) and the representative interactive flamelet model (RIF) using the commercially-available CFD solver, CONVERGE. Further studies were carried out for FGM model alone, including varying ambient temperature conditions and chemical mechanisms. Two chemical kinetics mechanisms with low-temperature chemistry for n-dodecane are employed to help to predict the occurrence of combustion recession. All simulations are performed under the Reynolds-averaged Navier-Stokes (RANS) framework in a grid-converged Lagrangian spray scenario. The simulation of combustion recession is qualitatively validated against experimental data from the literature and the efficacy of each model in predicting combustion recession is evaluated.

Chapter 6 aims to further the understanding of the effects of different chemical mechanisms in the prediction of a reactive diesel spray and its EOI process: combustion recession. Studies were performed under the Engine Combustion Network's (ECN) "Spray A" conditions using the Reynolds-Averaged Navier-Stokes simulation (RANS) and the Flamelet Generated Manifold (FGM) combustion model with four different chemical mechanisms for n-dodecane that are commonly used in the engine simulation communities - including recently developed reduced chemistry mechanisms. The flamelet database for each of the chemical mechanism was generated using two methods: 0D homogeneous reactor (HR) ignition flamelets and 1D igniting counterflow diffusion (ICDF) flamelets. The effect of different tabulation approaches is investigated first, followed by the discussion of the impact of chemical mechanisms on the prediction of combustion recession. Further discussions include an evaluation of the performance of chemical mechanisms in predicting the most relevant reacting spray characteristics compared to the ECN experimental database: ignition delay time (IDT), flame lift-off length (LOL) and flame reactive region.

Chapter 7 will be the first application of the newly developed combustion model Conditional Source Term Estimation (CSE). The combustion model is applied to a complex hydrocarbon fuel, n-dodecane, under Engine Combustion Network's (ECN) "Spray A" conditions. As such, detailed chemistry is included in tabulated form using the flamelet generated manifold (FGM) methodology. The predictions of this study will include both the Favre averaged conditional mass fraction of reactive species and temperature. Simulations are formed under both Reynolds-averaged Navier-Stokes Simulation (RANS) and Large Eddy Simulation (LES) framework. The objectives of this chapter are to provide (i) assessment of the application of CSE on igniting diesel spray (ii) comparison of the CSE numerical results with available experimental results and previous numerical simulations.

Chapter 8 summarizes the main conclusions from work presented in the thesis. It will also provide suggestions for future work that could improve the quality of the thesis.

1.4 List of Publications

The content presented in Chapter 4,5 and 6 has been peer-reviewed and published in the following:

- Joseph Camm, Martin Davy, XiaoHang Fang, Luke Doherty, Mathew McGilvray and Felix Foreste. "The Oxford Cold Driven Shock Tube (CDST) for Fuel Spray and Chemical Kinetics Research". In: *SAE Technical Paper 2018-01-0222.* SAE International,2018
- Louis Nicholson, XiaoHang Fang, Joseph Camm, David Richardson and Martin Davy. "Comparison of Transient Diesel Spray Break-Up between Two Computational Fluid Dynamics Codes". In *SAE Technical Paper 2018-01-0307.* SAE International, 2018
- XiaoHang Fang, Riyaz Ismail, Joseph Camm and Martin Davy. "Numerical Investigation of Combustion Recession on ECN Diesel Spray A". In *ASME 2017 Internal Combustion Engine Division Fall Technical Conference ICEF 2018-9597.* American Society of Mechanical Engineers, 2018
- XiaoHang Fang, Riyaz Ismail and Martin Davy. "A Study on Kinetic Mechanisms of Diesel Fuel Surrogate n-dodecane for the Simulation of Combustion Recession". In *SAE Technical Paper 2019-01-0202.* SAE International, 2019

The content presented in Chapter 7 has been submitted to Combustion Theory and Modelling and Proceedings of Combustion Institute:

- XiaoHang Fang, Riyaz Ismail, Kendal Bushe and Martin Davy. " Simulation of ECN Diesel Spray A using Conditional Source-term Estimation". In *Combustion Theory and Modelling*
- XiaohHang Fang, Riyaz Ismail, Kendal Bushe and Martin Davy. "Large Eddy Simulation on the End-of-Injection Diesel Spray Combustion". In *Proceedings of Combustion Institute*

In mathematics you don't understand things. You just get used to them.

— Johann von Neumann

2

Governing Equations

Contents

2.1 Overview

Turbulent reacting spray modelling requires both a comprehensive understanding of turbulent reacting flow modelling and spray modelling. Modelling of turbulent reactive flows presents a number of challenges, especially in the context of internal combustion engines, where the flow is compressible, multi-phase, multi-scale, unsteady and three dimensional. Due to strong coupling between the fluid dynamics and chemistry within the domain of interest, any modelling assumption made in order to close one set of equations will have an effect on others which could result in a misrepresentation of physical reality. Even though this strong coupling exists, the historical process is that each aspect of turbulent combustion is investigated and modelled in isolation, so as to limit complexity - with the evaluation of the model and its interactions with and effects on the rest of the system occurring at a later point in time. A formal definition of this process as expressed by Veynante & Vervisch [109] is shown in Figure 2.1. In this section, a brief background introduction for turbulent reacting flow modelling will be provided. Starting from the governing equations for fundamental fluid dynamics and thermodynamics in Section 2.2, followed by some of the most commonly used turbulence modelling strategies in Section 2.3. Finally a brief discussion on spray modelling is provided in Section 2.5. Numerical approaches for combustion modelling will be elaborated more in the following Chapter 3.

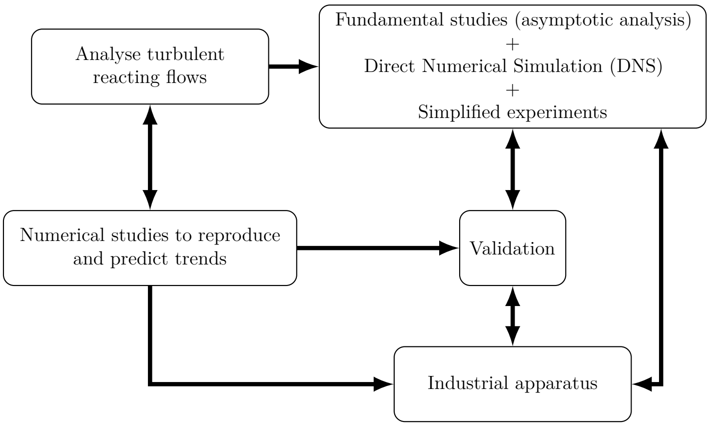

Figure 2.1: Combustion modelling steps, adapted from [109].

2.2 Conservation Equations for A Single Phase Turbulent Reacting Flow

A turbulent reacting flow is a multi-scale and highly non-linear phenomenon. Numerical study of turbulent reacting flow involves solving balance equations such as continuity, Navier-Stokes, species and energy equations. Different forms of these balance equations were developed to resolve the detail scales in turbulent reacting flows. Basic instantaneous local balance equations for a single-phase Newtonian reacting flow with varying density are listed here using the standard Cartesian notation:

- Continuity equation:

$$\frac{\partial \rho}{\partial t} + \frac{\partial}{\partial x_i}(\rho u_i) = 0 \tag{2.1}$$

- Conservation of momentum:

$$\frac{\partial}{\partial t}(\rho u_j) + \frac{\partial}{\partial x_j}(\rho u_i u_j) = -\frac{\partial}{\partial x_i} p + \frac{\partial}{\partial x_j}\tau_{ij} + F_i \tag{2.2}$$

  Where τ_{ij} denotes the viscous stress tensor and F_i denotes the body force acting on fluid. For a Newtonian fluid, assuming Stoke's hypothesis, the stress tensor is:

$$\tau_{ij} = \mu(\frac{\partial u_i}{\partial x_j} + \frac{\partial u_j}{\partial x_i} - \frac{2}{3}\frac{\partial u_k}{\partial x_k}\delta_{ij}) \tag{2.3}$$

  where μ is the molecular viscosity depending on fluid properties. δ_{ij} is the Kronecker delta function: $\delta_{ij} = 1$ if $i = j$, 0 otherwise.

- Species mass conservation:

$$\frac{\partial \rho Y_k}{\partial t} + \frac{\partial \rho u_j Y_k}{\partial x_j} = -\frac{\partial \mathscr{J}_j^k}{\partial x_j} + \dot{\omega}_k \tag{2.4}$$

  where $\mathscr{J}_j^k$ is the species molecular diffusive flux and $\dot{\omega}_k$ is mass reaction of species k per unit volume. From Fick's law of diffusion, $\mathscr{J}_j^k$ can be defined as followed:

$$\mathscr{J}_j^k = -\frac{\mu_l}{\mathrm{Sc}_k}\frac{\partial Y_k}{\partial x_j} \tag{2.5}$$

  where Sc_k is the Schmidt number of species k which describes the ratio of momentum diffusivity (viscosity) over mass diffusivity:

$$\mathrm{Sc}_k = \frac{\mu_l}{\rho D_k} \tag{2.6}$$

  D_k describes the molecular diffusion coefficient of species k in the rest of mixture. Molecular species diffusion due to temperature gradients (Soret) and heat flux due to species mass fraction gradients (Dufour) effects are neglected for this interpretation.

- Enthalpy conservation:

$$\frac{\partial \rho h_t}{\partial t} + \frac{\partial \rho u_j h_t}{\partial x_j} = \frac{\partial p}{\partial t} + \frac{\partial}{\partial x_j}\left(\mathscr{J}_j^h + u_i \tau_{ij}\right) + u_j F_j \tag{2.7}$$

Here h_t is the total enthalpy: $h_t = h + u_i u_i/2$. $\mathscr{J}_j^h$ is the enthalpy diffusion flux which can be described using Fourier's law [114]:

$$\mathscr{J}_j^h = -\frac{\mu_l}{\mathrm{Pr}}\left[\frac{\partial h}{\partial x_j} + \sum_{k=1}^{N}\left(\frac{\mathrm{Pr}}{\mathrm{Sc}_k} - 1\right) h_k \frac{\partial Y_k}{\partial x_j}\right] \tag{2.8}$$

Where Prandtl Number, Pr, describes the ratio of momentum diffusion over thermal diffusion:

$$\mathrm{Pr} = \frac{\mu_l \mathrm{C_p}}{\lambda} \tag{2.9}$$

There the non-dimensional Lewis number of species k, Le_k is introduced to compare the thermal diffusion and mass diffusion:

$$\mathrm{Le}_k = \frac{\mathrm{Sc}_k}{\mathrm{Pr}} = \frac{\lambda}{\rho \mathrm{C_p} D_k} \tag{2.10}$$

Under a unity Lewis number assumption the enthalpy diffusive flux Eq. 2.8 can be further simplified. Under a low Mach number assumption the enthalpy Eq. 2.7 and species conservation Eq. 2.4 are identical.

2.3 Turbulence Modelling

Turbulent flows are chaotic, unsteady, three-dimensional flows that exhibit vorticity. Although there is no universal definition for turbulent flow, it can be treated as a flow composed of eddies with different sizes [114]. The length scale for these eddies can range from the largest turbulent scale l_0 which is comparable to the flow scale $\mathscr{L}$ to the smallest, Kolmogorov scale η:

$$\eta \equiv (\frac{\nu^3}{\epsilon})^{1/4} \tag{2.11}$$

where ϵ is the turbulent dissipation rate. Taking a Fourier transform of the turbulent kinetic energy in space at a particular moment in time, turbulent kinetic energy at different wavelengths can be obtained:

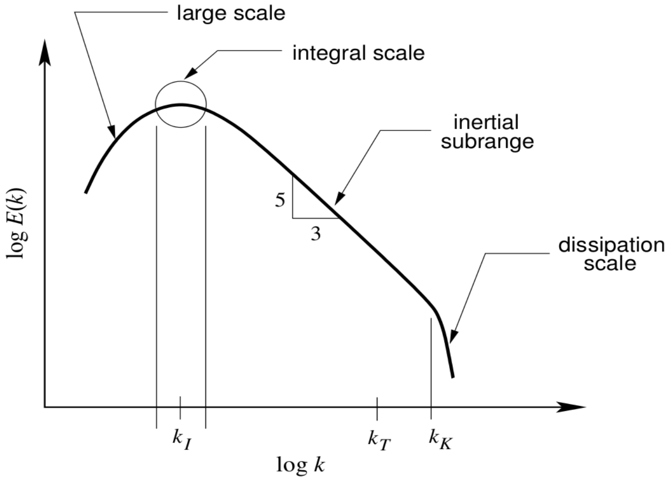

Figure 2.2: Energy Spectrum vs Wavelength, adapted from [114].

Figure 2.2 displays the behaviour of a turbulent energy spectrum, where wave number can be seen as the inverse of a length scale. Typically, the representation shown refers to isotropic and homogeneous turbulence, for which a conceptual theoretical framework is established. Following the hypotheses of Kolmogorov, the energy spectrum contains three distinct ranges, namely:

- Energy containing range. This range contains Integral (dominant length scale) eddies that interact with the mean flow and extract energy from it.

- Inertial sub-range. From Kolmogorov's second similarity hypothesis, motions of eddies in the inertial sub-range are determined by inertial effects. Eddies in this region are independent of both the energy-containing range and the dissipation sub-range, and the flow of energy through this range is expressed by Kolmogorov's $-\frac{5}{3}$ law as expressed in Equation 2.12

$$E(\kappa) = Constant \cdot \epsilon^{\frac{2}{3}} \cdot \kappa^{-\frac{5}{3}} \tag{2.12}$$

- Dissipation sub-range. Motions in the dissipation sub-range will experience significant viscous forces; therefore, this range is responsible for all essential energy dissipations. Eddies here are small and isotropic with scales defined by the Kolmogorov scale.

In order to describe turbulent flows with different scales, substantial research has been conducted. The three major methods used to simulate turbulent flows are Direct Numerical Simulation (DNS), Reynolds-Averaged Navier-Stokes (RANS) simulation, and Large Eddy Simulation (LES). The following section will present an overview of each method.

2.3.1 Direct Numerical Simulations

For Direct Numerical Simulation (DNS), all scales of the Navier-Stokes equations described in Section 2.2 are resolved with initial and boundary conditions appropriate to the flow considered. In addition, time steps in DNS are sufficiently small to accommodate the smallest perturbation in flow. Each simulation in DNS produces a single realisation of the flow. As a result, DNS requires computation cost scales at about Re^3 for both space and time. Extremely high computational cost in DNS made it impractical to solve most flows in engineering applications. Nevertheless, DNS of turbulent flows proves to be an indispensable tool in understanding fundamental processes of turbulent combustion. A number of turbulent reacting flows have been analysed using DNS, most of which studied drop evaporation and combustion in isotropic turbulence. Wang and Rutland [157] reviewed the autoignition process in turbulent n-heptane liquid-fuel spray jets. Later Schroll *et al.* [125] studied the role of evaporative cooling and turbulence mixing in liquid fuel spray jets. Both studies found that ignition kernels occurred at locations with low dissipation rate and leaner mixture fraction. A DNS study of a high-pressure sparse spray in n-heptane also showed that the autoignition occurred in a “spotty” pattern [13]. More recently, three-dimensional direct numerical simulations (DNS) were carried out to investigate the impact of the evaporation of droplets on diesel spray autoignition processes [67]. Moreover, an advanced combustion model coupled with DNS was also used to investigate the ignition processes in diesel engines [154]. A major finding from these recent studies is that diesel relevant combustion can involve a large number of combustion modes. Although these studies have shown great progress in understanding the fundamental physics behind turbulent combustion processes, DNS is still limited to simple combustion processes due to the limitations of current computational power.

2.3.2 Reynolds-Averaged Navier-Stokes (RANS) Simulation

First introduced by Reynolds in 1894, the governing equations of turbulent flow are averaged to describe only the mean flow field. Each varying quantity $\phi(x,t)$ can be decomposed as:

$$\phi(x,t) = \bar{\phi}(x,t) + \bar{\phi}\prime(x,t) \qquad with \;\; \overline{\phi\prime}(x,t) = 0 \tag{2.13}$$

where $\bar{\phi}(x,t)$ is the ensemble average of the quantity and $\phi\prime(x,t)$ is the fluctuation. This technique is widely used in non-reacting fluid flow with constant density.
In reacting turbulent flow, fluid density is constantly changing due to thermal heat release. Using the same technique above will introduce velocity/density fluctuation correlation $\overline{\rho\prime u\prime}$ which causes additional complexity in the problem, a density weighted averaging process (Favre averaging) [114] is introduced to overcome this term. The varying quantity is $\phi(x,t)$ is then decomposed as:

$$\phi(x,t) = \tilde{\phi}(x,t) + \tilde{\phi}(x,t)'' \tag{2.14}$$

where

$$\tilde{\phi} = \frac{\overline{\rho\phi}}{\bar{\rho}} \tag{2.15}$$

$$\tilde{\phi}'' = \frac{\overline{\rho(\phi - \tilde{\phi})}}{\bar{\rho}} = 0 \tag{2.16}$$

Apply the above operation to all governing equations we can get the Reynolds-Averaged Navier-Stokes equations for turbulent reacting flows:

- Continuity equation:

$$\frac{\partial \bar{\rho}}{\partial t} + \frac{\partial \bar{\rho} \tilde{u}_j}{\partial x_j} = 0 \tag{2.17}$$

- Conservation of momentum:

$$\frac{\partial \bar{\rho} \tilde{u}_i}{\partial t} + \frac{\partial \bar{\rho} \tilde{u}_j \tilde{u}_i}{\partial x_j} = -\frac{\partial \bar{\rho} \widetilde{u_i'' u_j''}}{\partial x_j} - \frac{\partial \bar{p}}{\partial x_i} + \frac{\partial \bar{\tau}_{ij}}{\partial x_j} + \bar{F}_i \tag{2.18}$$

- Species mass conservation:

$$\frac{\partial \bar{\rho} \tilde{Y}_k}{\partial t} + \frac{\partial \bar{\rho} \tilde{u}_j \tilde{Y}_k}{\partial x_j} = -\frac{\partial \bar{\rho} \widetilde{u_i'' Y_k''}}{\partial x_j} - \frac{\partial \overline{\mathscr{J}_j^k}}{\partial x_j} + \bar{\dot{\omega}}_k \tag{2.19}$$

- Enthalpy conservation:

$$\frac{\partial \bar{\rho} \tilde{h}_t}{\partial t} + \frac{\partial \bar{\rho} \tilde{u}_j \tilde{h}_t}{\partial x_j} = -\frac{\partial \bar{\rho} \widetilde{u_j'' h_t''}}{\partial x_j} + \frac{\partial \bar{p}}{\partial t} + \frac{\partial}{\partial x_j} \left(\overline{\mathscr{J}_j^h} + \overline{u_i \tau_{ij}} \right) + \overline{u_j F_j} \tag{2.20}$$

After applying the averaging operation to the governing equations, a number of unknown terms are introduced. The primary objective for turbulent combustion modelling is to close these unknown terms:

- *Reynolds Stresses* $\widetilde{u_i'' u_j''}$. The closure for Reynolds Stress will be discussed shortly.

- *Species* $(\widetilde{u_i'' Y_k''})$ and *enthalphy* $(\widetilde{u_j'' h_t''})$ turbulent fluxes. These flux terms can be closed using gradient diffusion hypothesis:

$$\bar{\rho} \widetilde{u_i'' \Phi_k''} = -\frac{\mu_t}{\mathrm{Sc}_{kt}} \frac{\partial \bar{\Phi}_k}{\partial x_j} \tag{2.21}$$

- *Chemical source term* $\bar{\dot{\omega}}_k$ is a major topic in combustion modelling. In Chapter 3 some common models available to close this term will be discussed.

Turbulent Viscosity Models

The most common approach in RANS modelling rely on eddy viscosity concepts developed by Boussineq. The assumption states that Reynolds stress anisotropy is a function of turbulent kinetic energy $\tilde{k}$ and mean velocity gradient. In Favre averaging form, the Reynolds stress can be expressed as:

$$\bar{\rho}\widetilde{u_i''u_j''} = -\mu_t \left(\frac{\partial \tilde{u}_i}{\partial x_j} + \frac{\partial \tilde{u}_j}{\partial x_i} \right) + \frac{2}{3}\bar{\rho}\tilde{k}\delta_{ij} \tag{2.22}$$

The only unknown term here is μ_t which stands for turbulent viscosity or eddy viscosity. There are several modelling methods that can close this term:

- Algebraic models

  These models are the simplest way to close eddy viscosity. They either assume the term being a constant or derive them from algebraic relations.

- One equation models

  One equation models usually solve transport equations for turbulent kinetic energy. The turbulent viscosity is then expressed in turns of turbulent kinetic energy. From these two steps, the turbulent viscosity can be modelled.

- Two equation models

  Two equation models are the most commonly used in RANS simulations. Among all two equation models, $k - \epsilon$ has shown great promise in engine combustion modelling. In this approach the turbulent viscosity is expressed as:

  $$\mu_t = \bar{\rho} C_\mu \frac{k^2}{\epsilon} \tag{2.23}$$

  Where the transport equations for turbulent kinetic energy, k, and its dissipation rate, ϵ, are solved individually:

  $$\frac{\partial \bar{\rho}\tilde{k}}{\partial t} + \frac{\partial \bar{\rho}\tilde{u}_j\tilde{k}}{\partial x_j} = \frac{\partial}{\partial x_j}\left(\frac{\mu_t}{\sigma_k}\frac{\partial \tilde{k}}{\partial x_j} \right) - \bar{\rho}\widetilde{u_i''u_j''}\frac{\partial \tilde{u}_i}{\partial x_j} - \bar{\rho}\tilde{\epsilon} \tag{2.24}$$

  $$\frac{\partial \bar{\rho}\tilde{\epsilon}}{\partial t} + \frac{\partial \bar{\rho}\tilde{u}_j\tilde{\epsilon}}{\partial x_j} = \frac{\partial}{\partial x_j}\left(\frac{\mu_t}{\sigma_\epsilon}\frac{\partial \tilde{\epsilon}}{\partial x_j} \right) - C_{\epsilon_1}\frac{\tilde{\epsilon}}{\tilde{k}}\bar{\rho}\widetilde{u_i''u_j''}\frac{\partial \tilde{u}_i}{\partial x_j} - C_{\epsilon_2}\bar{\rho}\frac{\tilde{\epsilon}^2}{\tilde{k}} \tag{2.25}$$

The model constants in these equations are usually [109] :

$$C_\mu = 0.09 \;\; ; \;\; \sigma_k = 1.0 \;\; ; \;\; \sigma_\epsilon = 1.3 \;\; ; \;\; C_{\epsilon 1} = 1.44 \;\; ; \;\; C_{\epsilon 2} = 1.92 \tag{2.26}$$

$k - \epsilon$ is popular in practical applications due to its simplicity and cost effectiveness. In order to adapt this concept to turbulent combustion modelling, Yakhot *et al.* [165] developed Re-Normalisation Group (RNG) $k-\epsilon$ to capture swirling and sheared turbulent flows. In order to account for smaller scales of motion the transport equation for the dissipation rate is modelled as [47]:

$$\frac{\partial \bar{\rho}\tilde{\epsilon}}{\partial t} + \frac{\partial \bar{\rho}\tilde{u}_j\tilde{\epsilon}}{\partial x_j} = \frac{\partial}{\partial x_j}\left(\frac{\mu_t}{\sigma_\epsilon}\frac{\partial \tilde{\epsilon}}{\partial x_j}\right) - C_{\epsilon_1}\frac{\tilde{\epsilon}}{\tilde{k}}\bar{\rho}\widetilde{u_i''u_j''}\frac{\partial \tilde{u}_i}{\partial x_j} - C_{\epsilon_2}\bar{\rho}\frac{\tilde{\epsilon}^2}{\tilde{k}} - C_{\epsilon_3}\bar{\rho}\tilde{\epsilon}\frac{\partial \tilde{u}_i}{\partial x_j} - R \tag{2.27}$$

The additional term, R, represents the effect of mean flow distortion on the turbulent kinetic energy dissipation rate and it is calculated using the following correlation:

$$R = \frac{C_\mu \tilde{\eta}^3\left(1 - \frac{\tilde{\eta}}{\eta_0}\right)}{1 + \beta\tilde{\eta}^3} \cdot \frac{\bar{\rho}\tilde{\epsilon}}{\tilde{k}} \tag{2.28}$$

where

$$\tilde{\eta} = S\frac{\tilde{k}}{\tilde{\epsilon}} \tag{2.29}$$

$$S = \left[2\left(\frac{1}{2}\left(\frac{\partial \tilde{u}_i}{\partial x_j} + \frac{\partial \tilde{u}_j}{\partial x_i}\right)\right)^2\right]^{1/2} \tag{2.30}$$

Although this model has shown some promising results in combustion simulation [153] [110], some intrinsic drawbacks for $k-\epsilon$ are unavoidable: The balance equations derived earlier for the turbulent kinetic energy, and the dissipation rate requires strong assumptions. For Equation 2.24 and Equation 2.25 the flow are assumed to have high Reynolds numbers, be homogeneous, and be isotropic which is rarely the case for practical flows.

- Reynolds Stress Models

  Reynolds stress models do not require the turbulent viscosity hypothesis to obtain Reynolds Stress. Instead, transport equations for all six components of the tensor stress are solved. One more equation is required to solve the turbulent length or time scale:

$$\frac{\partial \bar{\rho}\widetilde{u_i''u_j''}}{\partial t} + \frac{\partial}{\partial x_k}\left(\bar{\rho}\tilde{u}_k\widetilde{u_i''u_j''}\right) + \frac{\partial}{\partial x_k}T_{ijk} = P_{ij} + R_{ij} - \epsilon_{ij} \tag{2.31}$$

where T_{ijk} is the Reynolds-stress flux, R_{ij} is the pressure rate of strain tensor and ϵ_{ij} is the dissipation which requires modelling. Reynolds stress models have been successfully implemented in the past [138], however they are less commonly employed in RANS simulations due to a high computational cost as additional transport equations are solved. In addition, the model might encounter large discrepancies when dissipation is poorly predicted by its transport equation.

2.3.3 Large Eddy Simulations (LES)

Large eddy simulations explicitly solve large scales of motion in turbulent flow whereas smaller scales are modelled later. This technique has been widely employed in non-reacting flows [29][30][39][53][56]. The underlying idea behind LES is that most large scale flow structures in turbulent flows are geometry dependent whereas small scale structures generally exhibit universal properties. Therefore, LES's approach of modelling only small scale flow structures will provide a more accurate result [150].

LES Filtering

In LES, turbulent properties are filtered either in spectral space where resolved components greater than a given cut-off frequency are limited or in physical space where a weighted average is calculated in a given volume. The filtering operation can be described as:

$$\bar{Q}_i(x,t)s = \int Q_i(x',t)G(x-x')\mathrm{d}x' \tag{2.32}$$

where G is the LES filter. Common LES filters include[109]:

- Cut-off filter

$$\bar{G}(\kappa) = \begin{cases} 1 & if\, \kappa \leq \kappa_c \\ 0 & otherwise \end{cases} \tag{2.33}$$

  Where κ is the spatial wave number and κ_c is the limiting (cut-off) value for the wave number. This filter will eliminate all values less than the limiting wave number κ_c.

- Box filter

$$\bar{G}(\mathbf{x}) = G(x_1, x_2, x_3) = \begin{cases} \frac{1}{\Delta^3} & if\ |x_i| \leq \frac{\Delta}{2} \\ 0 & otherwise \end{cases} \tag{2.34}$$

  The box filter takes an average value of quantity Q over a cubic box size of Δ. here x_1, x_2, x_3 represents the spatial coordinates of location $\mathbf{x}$

- Guassian filter

$$\bar{G}(x) = G(x_1, x_2, x_3) = \left(\frac{6}{\pi\Delta^2}\right)^{1/2} \exp\left(-\frac{6x_i^2}{\Delta^2}\right) \tag{2.35}$$

Similar to RANS simulation, for variable density turbulent flow a mass weighted Favre averaging is introduced:

$$\bar{\rho}\tilde{Q}_i(x,t)s = \int \rho Q_i(x',t)G(x-x')\mathrm{d}x' \tag{2.36}$$

The filtered quantity $\bar{Q}$ is directly resolved in numerical simulation whereas the unresolved part $Q' = Q - \bar{Q}$ (i.e. the sub-grid scale part) will be modelled.

Flitered Governing equations

After applying Favre averaged filtering operations to instantaneous governing equations in Section 2.2 we can get the corresponding equations for LES:

- Continuity equation:

$$\frac{\partial \bar{\rho}}{\partial t} + \frac{\partial \bar{\rho}\tilde{u}_j}{\partial x_j} = 0 \tag{2.37}$$

- Conservation of momentum:

$$\frac{\partial \bar{\rho}\tilde{u}_i}{\partial t} + \frac{\partial \bar{\rho}\tilde{u}_j\tilde{u}_i}{\partial x_j} = -\frac{\partial}{\partial x_j}\left[\bar{\rho}\left(\widetilde{u_i u_j} - \tilde{u}_i\tilde{u}_j\right)\right] - \frac{\partial \bar{p}}{\partial x_i} + \frac{\partial \bar{\tau}_{ij}}{\partial x_j} + \bar{F}_i \tag{2.38}$$

- Species mass conservation:

$$\frac{\partial \bar{\rho}\tilde{Y}_k}{\partial t} + \frac{\partial \bar{\rho}\tilde{u}_j\tilde{Y}_k}{\partial x_j} = -\frac{\partial}{\partial x_j}\left[\bar{\rho}\left(\widetilde{u_j Y_k} - \tilde{u}_j\tilde{Y}_k\right)\right] - \frac{\partial \overline{\mathscr{J}^k}}{\partial x_j} + \bar{\dot{\omega}}_k \tag{2.39}$$

- Enthalpy conservation:

$$\frac{\partial \bar{\rho}\tilde{h}_t}{\partial t} + \frac{\partial \bar{\rho}\tilde{u}_j\tilde{h}_t}{\partial x_j} = -\frac{\partial}{\partial x_j}\left[\bar{\rho}\left(\widetilde{u_j h_t} - \tilde{u}_j\tilde{h}_t\right)\right] + \frac{\partial \bar{p}}{\partial t} + \frac{\partial}{\partial x_j}\left(\overline{\mathscr{J}_j^h} + \overline{u_i\tau_{ij}}\right) + \overline{u_j F_j} \tag{2.40}$$

In this set of equations, the following unclosed quantities require additional modelling:

- Unresolved Reynolds stress:
  $(\widetilde{u_i u_j} - \tilde{u}_i\tilde{u}_j)$, which requires a subgrid turbulence model (e.g. Smagorinnsky model)

- Unresolved enthalpy and species fluxes:
  $\left(\widetilde{u_j h_t} - \tilde{u}_j\tilde{h}_t\right)$, $\left(\widetilde{u_j Y_k} - \tilde{u}_j\tilde{Y}_k\right)$

- Filtered laminar diffusion fluxes for enthalpy and species
  $\overline{\mathscr{J}_j^h}$, $\overline{\mathscr{J}_j^k}$

- Filtered chemical source term: $\bar{\dot{\omega}}_k$

Although LES presents fewer details of turbulent reacting flow compare to DNS, it undoubtedly shows more details compared to RANS. As critical features such as flow instability and unsteady mixing are governed by large scale structures in turbulent flows, LES can demonstrate these phenomena while reducing the computation cost by modelling small scales. However, LES implementation on turbulent reactive flows of even canonical industrial problems is still challenging due to the high computational expense caused by complex geometry and a detailed fuel chemical mechanism. More importantly for reactive flows, especially with respect to non-premixed combustion, most of the turbulence chemistry interactions occur at scales which are modelled in both RANS and LES.

2.4 Conservation Equations for Two-Phase Turbulent Reacting Flow

In practical combustion systems such as diesel engines, fuels are stored in liquid form for convenience. When liquid fuels are used, additional physical processes are needed for the simulation. First governing equations for two-phase flow will be discussed followed with spray modelling in Section 2.5.

The governing equations mentioned in Section 2.2 are suitable for single-phase reacting flows. When considering two-phase flows, some modifications are required. Formulating a conservation or balance equation for two-phase flow can be done from either an Eulerian or Lagrangian viewpoint. An Eulerian viewpoint describes time changes in the flow field at a specific location. Meanwhile, a Lagrangian viewpoint describes flow characteristics by following an individual fluid particle as it moves through space and time. For two-phase flows, Eulerian-Eulerian (two-fluid) and Eulerian-Lagrangian models are widely used. The classical two-fluid models treat both liquid and gas phases as continua. This approach is more suitable for dense two-phase flows as it posses difficulties in modelling turbulent diffusion of the dispersed phase and momentum transfer between the phases [26]. Therefore the Eulerian-Lagrangian approach is more applicable to sprays as it treats fluid as a continuum and particles droplets as discrete entities [9]. Combined Eulerian-Lagrangian methods divide the solution process into two stages. First, the Eulerian part is solved, and then the dispersed portion is calculated. Coupling between these two stages is performed via variable source terms calculated at every control volume [120].

2.4.1 Gas (Eulerian) Phase

For gas phase:

- Continuity equation:

$$\frac{\partial \rho}{\partial t} + \frac{\partial}{\partial x_i}(\rho u_i) = \rho S \tag{2.41}$$

  Where S is the liquid fuel evaporation source term. The definition of this term and how it can be modelled will be discussed in Section 2.5.

- Conservation of momentum:

$$\frac{\partial}{\partial t}(\rho u_j) + \frac{\partial}{\partial x_j}(\rho u_i u_j) = -\frac{\partial}{\partial x_i} p + \frac{\partial}{\partial x_j}\tau_{ij} + F_s \tag{2.42}$$

  F_s represents the momentum gain/loss due to the gas-liquid interactions

- Species mass conservation:

$$\frac{\partial \rho Y_k}{\partial t} + \frac{\partial \rho u_j Y_k}{\partial x_j} = -\frac{\partial \mathscr{J}_j^k}{\partial x_j} + \dot{\omega}_k + \rho S_k \tag{2.43}$$

  where S_k is the evaporation source term for specie k.

- Enthalpy conservation:

$$\frac{\partial \rho h_t}{\partial t} + \frac{\partial \rho u_j h_t}{\partial x_j} = \frac{\partial p}{\partial t} + \frac{\partial}{\partial x_j}\left(\mathscr{J}_j^h + u_i \tau_{ij}\right) + u_j F_j + S_h \tag{2.44}$$

  Where S_h is the enthalpy induced

These equations can be introduced into turbulence modelling with both RANS and LES models. The modified models will then account for compressibility and spray interactions.

2.4.2 Liquid (Lagrangian) Phase

The governing equations for the liquid phase can be expressed in a Lagrangian view point. Although various forces may act on liquid droplets, only Stokesian drag and gravitational forces are considered [154]. For a single droplet d with x_d as its position, U_d as the velocity and T_d being the temperature, equations of motion and energy can be expressed as:

$$\frac{\mathrm{d}x_d}{\mathrm{d}t} = U_d \tag{2.45}$$

$$\frac{\mathrm{d}U_d}{\mathrm{d}t} = f_1 \frac{U(x_d, t) - U_d}{\tau_d} + g = \frac{3C_D}{2r_d}\frac{\rho_\infty}{\rho_L}|U_\infty - U_d|(U_\infty - U_d) + g \tag{2.46}$$

$$\frac{\mathrm{d}T_d}{\mathrm{d}t} = \frac{\mathrm{Nu}}{3\mathrm{Pr}}\frac{\mathrm{C_p}}{C_L}\frac{f_2}{\tau_d}(T_g - T_d) + \frac{\dot{m}_d}{m_d}\frac{L_V}{C_L} \tag{2.47}$$

Where f_1 represents an empirical constant for the Stokes'drag law [154]. $V(x_d, t)$ is the gas velocity at droplet position and g is the gravitational force. C_D the drag coefficient is commonly defined as [1]:

$$C_D = \begin{cases} \frac{24}{Re_d}(1 + \frac{\mathrm{Re}_d^{2/3}}{6}) & \mathrm{Re} < 1000 \\ 0.424 & \mathrm{Re} > 1000 \end{cases} \tag{2.48}$$

where

$$\mathrm{Re}_d = \frac{\rho |U_d - U| D}{\mu} \tag{2.49}$$

r_d as a transient property is directly related to mass evaporation rate $\dot{m}$ using:

$$\frac{\mathrm{d}r_d}{\mathrm{d}t} = -\frac{\dot{m}}{4\pi \rho_L r_d^2} \tag{2.50}$$

Sc and Pr are the Schmidt Number and Prandtl Number for the gas phase. Where Nu and Sh are the corrected Nusselt and Sherwood numbers with convection effects on evaporation. Clift*et al.* [23] used the following correlation:

$$\mathrm{Sh} = 1 + (1 + \mathrm{Re}_d \mathrm{Sc})^{1/3} f(\mathrm{Re}_d) \tag{2.51}$$

$$\mathrm{Nu} = 1 + (1 + \mathrm{Re}_d \mathrm{Pr})^{1/3} f(\mathrm{Re}_d) \tag{2.52}$$

where $f(\mathrm{Re}_d) = 1$ when $\mathrm{Re} \leq 1$ and $f(\mathrm{Re}_d) = \mathrm{Re}_d^{0.077}$ when $\mathrm{Re} \leq 400$. When $\mathrm{Re} \geq 400$ the correlation becomes[115]:

$$\mathrm{Sh} = 2 + 0.6 \mathrm{Re}_d^{1/2} \mathrm{Sc}^{1/3} \tag{2.53}$$

$$\mathrm{Nu} = 2 + 0.6 \mathrm{Re}_d^{1/2} \mathrm{Pr}^{1/3} \tag{2.54}$$

All properties mentioned above are evaluated using the 1/3 rule:

$$\bar{T} = T_s + \frac{1}{3}(T_\infty - T_s) \tag{2.55}$$

where the subscription s stands for the drop surface.

f_2 is a correction to the heat transfer due to evaporation. The value of both $\dot{m}$ and f_2 depend on the evaporation model which will be discussed in Subsection 2.5.1.

2.5 Spray Modelling

Two phase flow modelling considers various processes occurring within the liquid phase and on the liquid surface as well as the droplet break-up and atomization processes. The source term on the RHS of Equation 2.41 is a result of production and destruction of droplets which arise from all these processes. However, including all physical aspects of the two phase flow will be computationally challenging. Therefore, it is necessary to reduce certain processes and properties in modelling. In this section, three major processes will be discussed: drop evaporation, drop atomization and drop break-up. The evaporation process includes the interaction of droplets in spray with the surrounding gas while atomization and break-up processes reflect the spray formation.

2.5.1 Drop Evaporation

Heat and mass transfer during the evaporation process are characterized by the Spalding transfer numbers for mass (B_m) and energy (B_T)

$$B_m = \frac{Y_{v,s} - Y_{v,\infty}}{1 - Y_{F=v,s}}; \qquad B_T = (T_\infty - T_d)\frac{C_{p,v}}{L_v}, \tag{2.56}$$

Where Y_v is the mass fraction of fluid vapour in the gas phase and L_ν is the latent heat of evaporation. Subscripts s and ∞ stand for droplet surface and free stream respectively. Drop evaporation models can be categorized into two types: one based on the heat-mass transfer analogy and the other based on non-linear relationships between heat-mass transfer. The heat-mass transfer analogy assumes mass and heat transfer rate are the same at the droplet surface. The most widely used model based on this assumption is constant-droplet-temperature-model also known as the "D^2 law", where the diameter of droplet squared decreases linearly with time [137][43]:

$$\frac{\mathrm{d}D^2}{\mathrm{d}t} = C_{evap} \tag{2.57}$$

More commonly, the evaporation rate is expressed in terms of mass, or diameter. For example, the rate of evaporation for a single droplet can be expressed as:

$$\frac{\mathrm{d}m_d}{\mathrm{d}t} = -\pi D \mathscr{D} \rho_v \mathrm{Sh} ln \frac{p - p_{v,\infty}}{p - p_{v,s}} = -\pi D \mathscr{D} \rho_v \mathrm{Sh} ln(1 + \frac{Y_{v,s} - Y_{v,\infty}}{1 - Y_{v,s}}) \tag{2.58}$$

In order to solve the evaporation rate, the evaporation relaxation time, τ_e, is introduced:

$$\tau_e = \frac{m_d}{\pi D \mathscr{D} \rho_v \mathrm{Sh} ln(1 + B_m)} \tag{2.59}$$

With this concept, evaporation rate can be obtained by implicitly solving the following equations:

$$\frac{\mathrm{d}m_d}{\mathrm{d}t} = -\frac{m_d}{\tau_e}, \qquad \frac{\mathrm{d}D}{\mathrm{d}t} = -\frac{D}{-3\tau_e} \tag{2.60}$$

These equations are suitable for typical diesel engine conditions which are below the fuel's critical conditions. However, if the fuel starts boiling, Equation 2.58 is no longer valid. At boiling conditions the evaporation rate is governed by how fast heat can be transferred to the liquid. Therefore the evaporation rate needs to be modelled as follows:

$$\frac{\mathrm{d}m_d}{\mathrm{d}t} = -\frac{\pi D_k \mathrm{Nu}}{c_{p,v}} ln(\frac{c_{p,v}}{h_v}(T_\infty - T_d) + 1) \tag{2.61}$$

the boiling relaxation time, τ_{boil}, is introduced here:

$$\tau_{boil} = \frac{D^2 \rho_d c_{p,v}}{2k \mathrm{Nu} ln(\frac{c_{p,v}}{h_v}(T_\infty - T_d) + 1)} \tag{2.62}$$

The evaporation rate can be expressed in a similar fashion as previously:

$$\frac{\mathrm{d}D}{\mathrm{d}t} = -\frac{D}{\tau_{boil}} \tag{2.63}$$

2.5.2 Atomization

The attractiveness of the Lagrangian approach for spray modelling is that it can effectively remove the necessity of detailed modelling of the injector and nozzle. The objective of atomization models is then to describe the droplet properties at the nozzle exit, thereby providing initial conditions for the spray parcels. The simplest way to describe the droplets at nozzle exit is to set the droplet properties (i.e. diameter) and spray angles as constants. In Reitz and Diwakar's [117] [118] model, uniform droplet diameters are computed using the nozzle diameter multiplied by a prescribed contraction constant. The droplet velocity is calculated from prescribed injector properties such as: the injection rate profile, L/D ratio and surface roughness. Despite the assumption of a uniform diameter at the nozzle exit, a variety of drop sizes are found shortly after injection due to air fuel interactions which leads to break-up models as discussed in Subsection 2.5.3. There also exist more complex atomization models, for example the one proposed by Huh and Gosman [52], which is capable of predicting spray angles, drop size distributions and drop velocities at the nozzle exit. Although using a more elaborate model seems more promising for spray modelling, the advantage of using such models can be easily lost due to the uncertainties created in later break-up models. Moreover, intrinsic limitations in taking experimental data in the near nozzle region makes validating atomization models challenging. Specifying initial conditions with prescribed parameters will be both simpler and faster, and most likely no less accurate.

2.5.3 Break-Up Models

After injection the surrounding gas creates a non-uniform distribution of pressure and shear stress on the moving particle surface which leads to droplet deformation and eventually break-up. The purpose of the break-up model is then to represent the reduction of droplet characteristic size and if possible introduce new droplets detached from the original droplet. Disturbances acting on the droplet surface can be characterized using either Rayleigh-Taylor (RT) or Kelvin-Helmholtz (KH) instabilities [6]. Different models are built on top of these two modes:
The KH model describes the newly formed droplet with radius r_c using the following equations:

$$r_c = B_0 \Lambda_{KH} \tag{2.64}$$

The parent droplet size r is then reduced according the following expressions [97]:

$$\frac{\mathrm{d}r}{\mathrm{d}t} = -\frac{r - r_c}{\tau_{KH}}, \qquad \tau_{KH} = \frac{3.788 B_1 D}{\Omega_{KH} \Lambda_{KH}} \tag{2.65}$$

where $B_0 = 0.61$, and B_1 being an arbitrary number in the range 10 to 60. Λ_{KH} is the wavelength for the wave Ω_{KH} with its maximum growth rate. The frequency and wavelength for this wave is described as:

$$\Omega_{KH} = \frac{0.34 + 0.38\mathrm{We}^{1.5}}{(1+\mathrm{Oh})(1+T^{0.6})}\sqrt{\frac{\sigma}{\rho_d r^3}} \tag{2.66}$$

$$\Lambda_{KH} = 9.02r\frac{(1+0.45\sqrt{Oh})(1+0.4T^{0.7})}{(1+0.865We^{1.67})^{0.6}} \tag{2.67}$$

The non-dimensional Weber number (We) and Ohnesorge number (Oh) are defined as:

$$\mathrm{We} = \frac{\rho|u_{rel}|^2 r}{\sigma}, \qquad \mathrm{Oh} = \frac{\sqrt{\mathrm{We}_l}}{\mathrm{Re}_l} \tag{2.68}$$

where u_{rel} is the relative velocity between liquid and gas, We_l is the liquid Weber number and Re_l is the liquid Reynolds number. The Taylor number T is then calculated via:

$$T = \mathrm{Oh}\sqrt{\mathrm{We}_g} \tag{2.69}$$

The RT model predicts instability in a different way, it tracks the growth of RT waves on the surface of droplets until it reaches the characteristic RT time when the droplet suddenly breaks-up into smaller droplets. Similarly, the RT model is also based on a wave instability where the frequency of the fastest growing wave is defined as:

$$\Omega_{RT} = \sqrt{\frac{2}{\sqrt{27\sigma}}\frac{|g_t(\rho_l - \rho)|^{3/2}}{\rho_l + \rho}} \tag{2.70}$$

The characteristic RT time is then the inverse of this frequency $\tau_t = 1/\Omega_{RT}$ and the wavelength Λ_{RT} is defined as:

$$\Lambda_{RT} = \frac{\pi}{K} \tag{2.71}$$

Where

$$K = \sqrt{\frac{|g_t(\rho_l - \rho)|}{3\sigma}}, \qquad g_t = (g + \frac{du_d}{dt}) \cdot \frac{u_d}{|u_d|} \tag{2.72}$$

Once the drop is to break-up, the new droplet radius is modelled as:

$$r_{new} = \frac{\pi C_{RT}}{K_{RT}} \tag{2.73}$$

where C_{RT} again is an adjustable constant. In practice, these two models are commonly combined together. The KH model is applied to predict the initial break-up of the injected "blobs", and then the RT model is used to predict the secondary break-up [163].

In addition to the KH and RT models, there are also popular models that are based on the Taylor analogy break-up (TAB) approach [95]. Additional improvements were made to the TAB method to account for different break-up regimes present in diesel environment [142]. Some of them also include atomization models within break-up models [143][144]. Pilch [108] also developed a model using break-up data and velocity history data to predict the maximum stable size of the droplet.

The greatest obstacle to discovery is not ignorance – it is the illusion of knowledge. Never tell people how to do things. Tell them what to do and they will surprise you with their ingenuity.

— General George S. Patton

3

Combustion Modelling

Contents

3.1 Overview

Combustion, even without turbulence, is a complicated process involving a large range of chemical, time and length scales. Turbulent reacting flow modelling is present in most practical combustion systems including industrial furnaces, internal combustion engines and aircraft engines. As combustion processes are difficult to capture using analytical strategies, numerical analysis is of great interest. There are two principal modes for combustion which are based on the mixing state of fuel and oxidiser prior to combustion. Non-premixed combustion describes combustion where fuel and oxidiser are not mixed prior to combustion whereas premixed combustion provides a fuel oxidiser mixture prior to combustion. In practical cases, most turbulent reacting flows exhibit a hybrid behaviour of these two modes of combustion. However, due to the complexity of analysing partially-premixed combustion, the combustion modelling discussed here will mainly focus on the non-premixed mode of turbulent combustion. In this chapter, a detailed review for the chemical source term will be presented in Section 3.2 followed by some commonly recognised combustion modelling tools in Section 3.3.

3.2 Chemical Source Term

In terms of numerically solving turbulent reacting flow equations discussed in Section 2.2, the biggest challenge is to close the chemical source term $\dot{\omega}$ due to its non-linearity. First introduced by Borghi [15] a “moments approach” is to tackle the closure of this term. Similar to Borghi, Veynante and Vervisch [150] also performed a Taylor expansion of the chemical source term which clearly demonstrates its non-linear characteristics. A single step irreversible chemical reaction between fuel F and Oxidizer O is assumed here:

$$F + sO \Longrightarrow (1+s)P \tag{3.1}$$

Based on an Arrhenius law and Taylor expansion, the mean fuel mass reaction rate $\bar{\dot{\omega}}_F$ is described as:

$$\begin{aligned}\bar{\dot{\omega}}_F =& -A\bar{\rho}^2\tilde{T}^b\tilde{Y}_F\tilde{Y}_O exp\left(-\frac{T_A}{\tilde{T}}\right)\\ &\times\left[1+\frac{\widetilde{Y_F''Y_O''}}{\tilde{Y}_F\tilde{Y}_O}+(P_1+Q_1)\left(\frac{\widetilde{Y_F''T''}}{\tilde{Y}_F\tilde{T}}+\frac{\widetilde{Y_O''T''}}{\tilde{Y}_O\tilde{T}}\right)\right. &&(3.2)\\ &\left.+(P_2+Q_2+P_1Q_1)\left(\frac{\widetilde{(Y_F''T'')^2}}{(\tilde{Y}_F\tilde{T})^2}+\frac{\widetilde{(Y_O''T'')^2}}{(\tilde{Y}_O\tilde{T})^2}\right)+...\right] &&(3.3)\end{aligned}$$

where P_n and Q_n represent:

$$P_n = \sum_{k=1}^{n}(-1)^{n-k}\frac{(n-1)!}{(n-k)![(k-1)!]^2k}\left(\frac{T_A}{\tilde{T}}\right)^k \tag{3.4}$$

$$Q_n = \frac{b(b+1)...(b+n-1)}{n!} \tag{3.5}$$

Although the mean fuel mass reaction rate can be successfully described in Equation 3.3, a number of obstacles have been raised in terms of solving this equation. First, this equation has introduced multiple new moment terms such as $(\widetilde{Y_k''T''})^n$, which require either algebraic expansion of transport equations. It is possible to model the mean fuel mass reaction rate by dropping out the higher-order terms in Equation 3.3, however, due to its non-linearity, the truncation would result in large errors in simulation especially when the activation energy is high [150]. Moreover, the rather complicated expression in Equation 3.3 is only valid for a single irreversible reaction and can be difficult to implement in realistic chemical schemes. Because of such considerations, the 'moments approach' has been abandoned for most combustion modelling cases.

3.3 Models

A comprehensive review of current combustion models can be found in Veynante and Vervisch [150], and persisting challenges can be found in Bray [16]. In this section, a selected number of models applicable to non-premixed combustion are presented. Non-premixed combustion models can be mainly divided into two groups: infinitely fast chemistry and finite rate. The distinction between these two groups is based on Damköhler number, which compares the turbulent mixing time scale and the chemical reaction time scale.

3.3.1 Eddy Break Up Model

One of the simplest and yet most widely used models for infinitely fast chemistry ($Da \gg 1$) is the Eddy Break Up (EBU) model which was first proposed by Spalding [136]. The model is based on the idea that combustion is mainly controlled by turbulent mixing processes. The characteristic turbulent time scale for a mixing process can be estimated using the ratio of turbulent kinetic energy to its dissipation rate:

$$\tau_t = \frac{k}{\epsilon} \tag{3.6}$$

In the Eddy Break Up context, the mean reaction rate can be expressed as:

$$\bar{\dot{\omega}}_F = \bar{\rho} C_{EBU} \frac{1}{\tau_t} \sqrt{\widetilde{Y_F''^2}} \tag{3.7}$$

where C_{EBU} is the Eddy Break Up model constant and $\widetilde{Y_F''^2}$ is the mass fraction fluctuation which requires an additional transport equation to close.

The Eddy Break Up model and other similar models are used due to their simplicity and generally low computational cost. However, as the modelled reaction rate assumes homogeneous as well as isotropic turbulence and is independent of chemical time scales, it tends to overpredict in high strain flow regions [150]. Additionally, due to the infinitely fast chemistry assumption characteristics such as ignition, reignition and flame stability can not be captured using these models. Moreover, some adjustments need to be implemented for model constants to mimic practical chemical features [121].

3.3.2 Laminar Flamelet Models

First proposed by Peters [100] [101], laminar flamelet models are more sophisticated models which utilize finite rate chemistry. Flamelet models are applicable to combustion regimes with high Damköhler number where chemical time-scales are much shorter than turbulence scales. If the flame thickness is much smaller than the turbulent scale, the flame can be treated as a locally one-dimensional laminar flame sheet embedded in the flow. In order to construct flamelet models, mixture fraction Z and scalar dissipation rate χ are used as control parameters. Using asymptotic analysis the flamelet equations for species and temperatures are as follows:

$$\rho \frac{\partial Y_k}{\partial t} = \frac{\rho}{2} \chi \frac{\partial^2 Y_k}{\partial Z^2} + \dot{\omega}_k \tag{3.8}$$

$$\rho \frac{\partial T}{\partial t} = - \sum_{n=1}^{N} \frac{h_n \dot{\omega}}{C_p} + \chi \left(\frac{\partial^2 T}{\partial Z^2} \right) \tag{3.9}$$

In order to capture flame properties (temperature, species composition, mean reaction rate), flamelet equations are pre-calculated using detailed chemical mechanisms and stored as flamelet libraries. Mean properties of the flame are then obtained by using the flamelet library combined with a joint Probability Density Function (PDF) model of Z and χ using the following equations [150]:

$$
\begin{align}
T =& T(z,t) \tag{3.10}\\
Y_k =& Y_k(z,t) \tag{3.11}\\
\bar{\rho}\tilde{Y_k} =& \int_0^{+\infty}\int_0^1 \rho Y_k(Z,\chi)p(Z,\chi)dzd\chi \tag{3.12}\\
\bar{\rho}\tilde{T} =& \int_0^{+\infty}\int_0^1 \rho T(Z,\chi)p(Z,\chi)dzd\chi \tag{3.13}
\end{align}
$$

One of first developed flamelet models is the Stationary Laminar Flamelet Model (SLFM), which neglects the transient terms in Equation 3.8 and Equation 3.9. SLFM models have been successfully used to study steady spray diffusion flames [50]. However, neglecting the transient behaviour of the dissipation rate makes it insufficient in predicting unsteady flame characteristics such as extinction and reignition. The effects of unsteadiness are later included in the Representative Interactive Flamelet (RIF) approach, which uses time-varying parameters to integrate flamelet equations. Different ignition phenomena are captured in diesel engines using RIF models [36] [152]. Capable of including the transient pressure in flamelet equations (not shown in Equation 3.9), RIF allows a better representation for practical engine simulations. Flamelet models are widely used in non-premixed combustion modelling. Efforts have been made to improve flamelet models in capturing effects of unsteadiness, flame curvature and other transient phenomena, newer models such as the Lagrangian Flamelet Model (LFM) and the Unsteady Laminar Flamelet Models (ULFM) have shown great success in studying extinction and reignition for non-premixed flame [83][5]. Different flamelet methods have been applied to various flame structures; in the following chapters, more detailed information will be included for those flamelet models applicable to engine combustion modelling.

3.3.3 Probability Density Function (PDF) Methods

A statistical tool for closing the mean reaction rate term is Probability Density Function Modelling. If the joint probability density function of all unknown scalars is provided, mean reaction rate can be recovered by a simple integration. That is:

$$\overline{\omega}_{\phi_1}(\overrightarrow{x},t) = \int_{\phi_1} ... \int_{\phi_N} \omega_{\phi_1}(\phi_1^*, ...\phi_N^*)\bar{P}(\phi_1^*, ...\phi_N^*; \overrightarrow{x}, t)d\phi_1^*...d\phi_N^* \tag{3.14}$$

Where ϕ^* is the sample space variable for ϕ and it obeys the following relationships [112]:

$$\int_\phi \bar{P}(\phi^*; \vec{x}, t)d\phi^* = 1 \tag{3.15}$$

$$\int_\phi (\phi^* - \bar{\phi})^2 \bar{P}(\phi^*; \vec{x}, t)d\phi^* = \widetilde{\Psi'^2}(\vec{x}, t) \tag{3.16}$$

$P(\phi_1, ...\phi_N)$ in Equation 3.14 is the joint probability density function. One approach to obtain this PDF is to provide a given shape (Presumed PDF) based on available mean quantities [111]. In non-premixed combustion context, the presumed PDF shape is often chosen as a $\beta - function$. The $\beta - function$ PDF method has been applied to various practical non-premixed combustion cases [42],[74]. However, presumed PDF shape tends to oversimplify the real PDF which can lead to large errors in simulation.

A more rigorous way to obtain this joint PDF is to solve its transport equation [111][112]. The transport equation proposed by Pope follows [150]:

$$\begin{aligned}
\frac{\partial}{\partial t}\left[\bar{P}(\mathbf{u}^*, \phi^*; \vec{x}, t)\right] &+ \mathbf{u}^* \cdot \nabla \bar{P}(\mathbf{u}^*, \phi^*; \vec{x}, t) + \left(\nu \nabla^2 \bar{u}_i - \frac{1}{\bar{\rho}}\frac{\partial \bar{p}}{\partial x_i}\right)\frac{\partial}{\partial u_i^*}\left[\bar{P}(\mathbf{u}^*, \phi^*; \vec{x}, t)\right] \\
&+ \frac{\partial}{\partial \phi^*}\left[\dot{\omega}(\phi^*)\bar{P}(\mathbf{u}^*, \phi^*; \vec{x}, t)\right] \\
&= \underbrace{\frac{\partial}{\partial u_i^*}\left[\left(\overline{\frac{1}{\bar{\rho}}\frac{\partial p'}{\partial x_i}\,|\mathbf{u} = \mathbf{u}^*, \phi = \phi^*}\right)\bar{P}(\mathbf{u}^*, \phi^*; \vec{x}, t)\right]}_{Pressure\,fluctuations} \\
&\quad \underbrace{-\frac{\partial}{\partial u_i^*}\left[\left(\overline{\nu \nabla^2 u_i' \mid \mathbf{u} = \mathbf{u}^*, \phi = \phi^*}\right)\bar{P}(\mathbf{u}^*, \phi^*; \vec{x}, t)\right]}_{Viscous\,dissipation} \\
&\quad - \underbrace{\frac{\partial}{\partial \phi^*}\left[\left(\overline{D \nabla^2 \Psi\,|\mathbf{u} = \mathbf{u}^*, \phi = \phi^*}\right)\bar{P}(\mathbf{u}^*, \phi^*; \vec{x}, t)\right]}_{Molecular\,diffusion}
\end{aligned} \tag{3.17}$$

The attractiveness of Transported PDF methods can be seen here as all terms at the left hand side of Equation 3.17 are closed. These terms represent: the change of PDF over time, convection, transport in physical space due to velocity fields and the chemical source term respectively. Terms at the RHS representing pressure fluctuation, viscous dissipation and molecular diffusion, however, are not closed. One major characteristics for Equation 3.17 is high dimensionality which could lead to exponentially increasing memory size for methods such as finite volume and finite difference [114]. Although Monte-Carlo methods [112] have been successfully used to reduce the memory size in PDF methods, with current technology PDF methods are still computationally intensive and too expensive to be used in pratical cases.

3.3.4 Conditional Moment Closure

Established individually by Klimenko [62] and Bilger [11], conditional moment closure is based on the fact that fluctuations in scalar quantities can be significantly reduced after conditioning with one principal quantity. Mixture fraction Z is used as a conditional variable for non-premixed combustion because experiments have shown that mixture fraction plays an integral role in determining quantities such as mean reaction rates and temperature [81][37]. In the absence of transient combustion behaviour, Z is found to considerably reduce the non-linearity of the mean reaction rates. Although the final governing equations are the same, Bilger used a decomposition method to derive them whereas Klimenko started with joint possibility density function (PDF) methods. Detailed derivations and comparison for these two methodologies can be found in the joint paper [61]. CMC solves transport equations for mean mass fraction (Y_α) and temperature (T) conditioned on mixture fraction noted as:

$$Q_\alpha(\vec{x},t,\eta) = \langle Y_\alpha(\vec{x},t) | \zeta(\vec{x},t) = \eta \rangle \tag{3.18}$$

$$Q_T(\vec{x},t,\eta) = \langle T(\vec{x},t) | \zeta(\vec{x},t) = \eta \rangle \tag{3.19}$$

where $Q_\alpha(\vec{x},t,\eta)$ and $Q_T(\vec{x},t,\eta)$ are the conditional mass fraction and conditional temperature respectively. η is the mixture fraction sample space variable.

$$\langle \cdot | \zeta(\vec{x},t) = \eta \rangle \tag{3.20}$$

Equation 3.20 represents the operation of taking ensemble averages of quantity subject to a mixture fraction condition.

Following the decomposition strategy proposed by Bilger, mean quantities can be decomposed as (only mean species mass fraction is shown here):

$$Y_\alpha(\vec{x},t) = Q_\alpha(\eta,\vec{x},t) + Y_\alpha''(\vec{x},t) \tag{3.21}$$

Similar to the Reynolds Averaging concept, here the conditional mean Q_α is treated as a non-fluctuating quantity. Then apply this concept to Favre average species Equation 2.19 and energy Equation 2.20, the CMC equations are as follows:

$$\frac{\partial Q_\alpha}{\partial t} + \underbrace{\langle u_j|\eta\rangle \frac{\partial Q_\alpha}{\partial x_i}}_{convective\,term} - \underbrace{\langle N|\eta\rangle \frac{\partial^2 Q_\alpha}{\partial \eta^2}}_{mixing\,term} + \underbrace{\frac{1}{\bar{\rho}\tilde{P}(\eta)} \frac{\partial}{\partial x_j}\left[\left\langle \rho u_j'' Y_\alpha'' | \eta \right\rangle \tilde{P}(\eta)\right]}_{diffusive\,term} = \underbrace{\langle \dot{\omega}_\alpha | \eta \rangle}_{chemical\,source\,term} \tag{3.22}$$

$$\begin{aligned}
\frac{\partial Q_T}{\partial t} + \langle u_j|\eta\rangle \frac{\partial Q_T}{\partial x_j} = {} & -\frac{1}{\bar{\rho}\tilde{P}(\eta)} \frac{\partial}{\partial x_j}\left[\left\langle \rho u_j'' T'' | \eta \right\rangle \tilde{P}(\eta)\right] + \langle N|\eta\rangle \frac{\partial^2 Q_\alpha}{\partial \eta^2} \\
& + \langle N|\eta\rangle \frac{\partial Q_T}{\partial \eta}\left[\frac{1}{\langle c_p|\eta\rangle}\left(\frac{\partial \langle c_p|\eta\rangle}{\partial \eta} + \sum_{\alpha=1}^{N} c_{p,\alpha} \frac{\partial Q_\alpha}{\partial \eta}\right)\right] \qquad (3.23) \\
& + \frac{\langle \dot{\omega}_H|\eta\rangle}{\langle \rho|\eta\rangle \cdot \langle c_p|\eta\rangle} + \frac{1}{\langle c_p|\eta\rangle}\left\langle \frac{1}{\rho}\frac{\partial P}{\partial t} | \eta \right\rangle \qquad (3.24)
\end{aligned}$$

Assuming small fluctuations of mean reaction rate around its conditional averages, the chemical source term can be closed using first order closure [61]:

$$\langle \dot{\omega}_\alpha | \eta \rangle \approx \dot{\omega}_\alpha(Y_k|\eta, T|\eta, \rho|\eta) \tag{3.25}$$

The unconditional source term can be calculated with a mixture fraction PDF:

$$\bar{\dot{\omega}}_\alpha = \int_0^1 \langle \dot{\omega}_\alpha | \eta \rangle \, P(\eta) d\eta \tag{3.26}$$

Assuming homogeneous turbulence with constant density Equation 3.22 can be further reduced to:

$$\frac{\partial Q_\alpha}{\partial t} - \langle N|\eta\rangle \frac{\partial^2 Q_\alpha}{\partial \eta^2} = \langle \dot{\omega}_\alpha|\eta\rangle \tag{3.27}$$

It can be noticed that CMC equations closely resemble flamelet Equation 3.8 as they both have a rate of change term, a mixing term and a chemical source term. However, unlike the flamelet model, the CMC model has no constraint regarding to flame regime which allows it to accommodate more practical cases. Solutions of CMC equations will provide conditional temperature and mass fractions of all species at any location and time in the flow field. Moreover, CMC models can greatly reduce computational cost as less stochastic realisations are necessary in CMC models compared to PDF models. The solving process for CMC is depicted in Figure: 3.1.

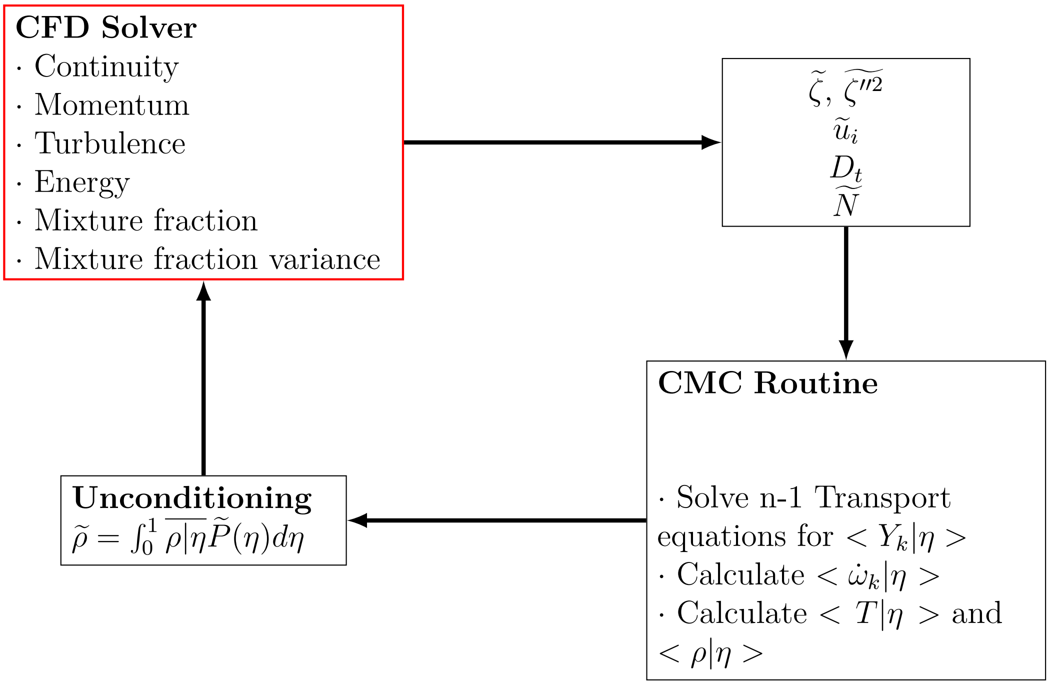

Figure 3.1: CMC routine structure

CMC has been a great success in a wide variety of non-premixed combustion problems including turbulent lifted flame [98], autoigniting methane [122] and turbulent pilot flames [33]. CMC has also been suitable for both soot formation prediction in a turbulent non-premixed methane jet flame [69] and two-phase flows

[161]. In terms of diesel spray studies, CMC successfully captured spray evolution, ignition delay and pressure development in a closed combustion chamber at diesel engine conditions [162]. Good agreement between computational results and experimental results were observed for n-heptane spray autoignition characteristics using CMC under diesel engine conditions [14]. More recently, Blomberg *et al.* [19] investigated n-dodecane split injections of “Spray A” using a CMC combustion model with both RANS and LES turbulence treatments. LES-CMC was able to capture the combustion recession after the end of the first injection, whereas RANS-CMC was not successful in obtaining all combustion recession details. Among all these models, the first moment CMC hypothesis is used. However, when extinction and reignition phenomena are present, first-moment closure in CMC will break down. One refinement is to use higher-order closure which is also derived in Bilger and Klimenko’s joint paper [61]. Han and Huh [46] used both first and second-order Lagrangian CMC methods to study piloted jet diffusion flames near extinction. The second-order CMC model showed a noticeable improvement of species mass fraction compared to the first order CMC model. Kim *et al.* [130] applied a second-order CMC model to a turbulent non-premixed hydrocarbon flame where significant local extinction and reignition are present. The model has shown improvements in predicting intermediate species; however, additional modelling is required for unclosed terms which makes it less appealing. Another approach is to introduce a second conditioning variable in conjunction with the mixture fraction. Pitsch *et al.* [21] introduced a scalar dissipation rate as the variable due to its physical significance in extinction/reignition phenomena [100]. The method describes extinction in the flame reasonably well; however, the onset of reignition prediction in the study is too early. More recently, Kronenberg [68] adopted sensible enthalpy as a second conditioning variable and presented excellent computational results in agreement with DNS results at all times. The success of capturing extinction and reignition makes CMC a preferred candidate for modelling combustion recession; however, CMC models are still computationally expensive, not only due to the modelling of unclosed terms in transport equations (Equation

3.23 and Equation 3.22), but also the additional dimension in CMC equations introduced by second conditional variable. Therefore it is of interest to find another combustion model that inherits CMC's advantage of having fewer constraints on combustion regimes but requires less computational resources when higher-order closure or a second conditioning variable is introduced.

3.3.5 Conditonal Source-Term Estimation

Conditional source-term estimation (CSE) was first introduced by Bushe and Steiner [18], and it seeks closure of chemical source term using the same first-moment hypothesis in CMC. However, instead of solving transport equations for conditionally averaged scalars, CSE estimated conditional means from unconditionally averaged scalars. CSE assumes spatial homogeneities exist on defined surfaces in the flow field, leading to the recovery of the conditional averages through inversion of Equation 3.26. CSE is more computationally efficient compared to CMC owing to this inversion process. It also possesses the advantage of CMC that no assumptions are made regarding flame regimes. Similar to CMC, doubly conditional source-term estimation (DCSE) using scalar dissipation rate can also be used to predict combustion instabilities such as reignition and extinction. Dovizio *et al.* [28],[27] studied both turbulent stratified V-shaped flame and series of lifted turbulent jet flames using DCSE. The local ignition/extinction phenomenon was successfully captured in both cases. Apart from all the advantages of CSE, directly including detailed chemistry in CSE is still challenging, especially with hydrocarbon fuels which involve hundreds of species and reactions. Inverting each species in these fuels would be computationally prohibitive, and species transport equations will be too stiff for any current ODE solvers to handle. Therefore a reduced chemistry model of some sort is necessary so that a limited number of scalars can represent the detailed chemistry. A typical CSE solving process for a methane combustion simulation is depicted in Figure 3.2, which includes interactions of each component in CSE. Further details on CSE and its extension to spray combustion will be presented in Chapter 7.

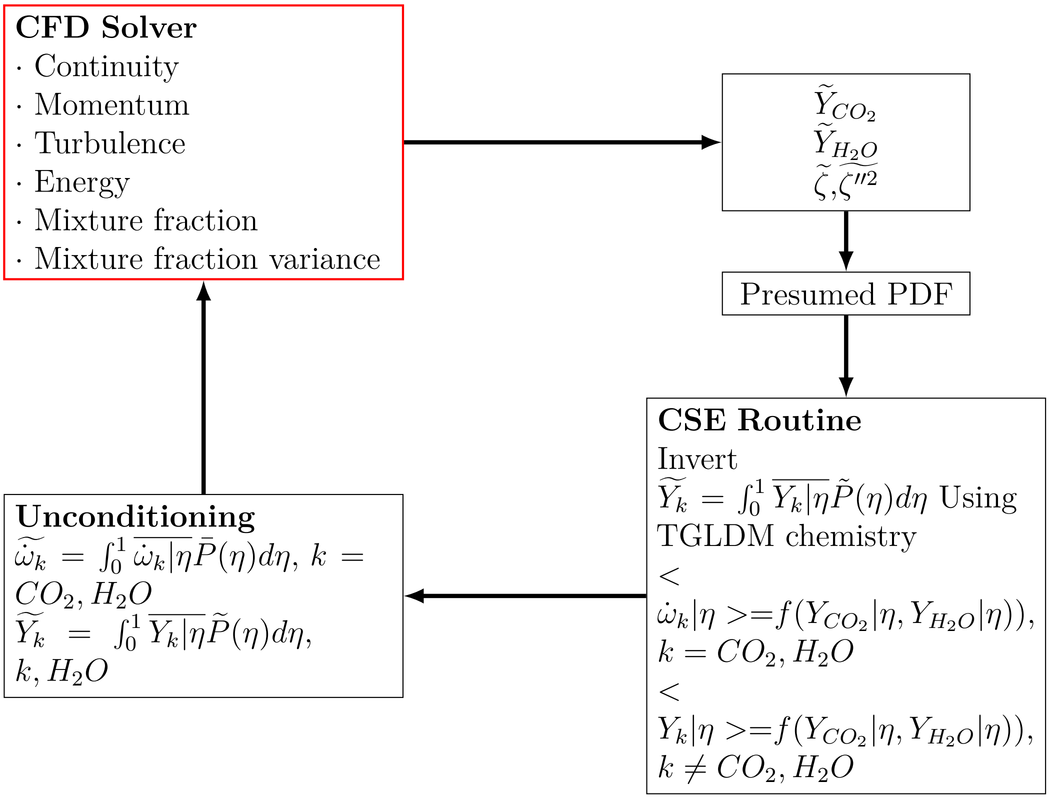

Figure 3.2: CSE routine structure for a typical methane-air flame

3.4 Summary

Turbulent reacting spray simulation is particularly challenging due to the coupling of different phenomena such as fluid dynamics, chemical kinetics, phase changes and liquid-gas interactions. Depending on the application and characteristics of combustion phenomena, different combustion models can be used to tackle the problem.

The great thing about science is that you can get it wrong over and over again because what you're after - call it truth or understanding - waits patiently for you. Ultimately, you'll find the answer because it doesn't change.

— Dudley Herschbach

4

Non-reacting Spray

Contents

The content in this chapter is a result of the collaborative efforts of the author, Dr Riyaz Ismail and Louis Nicholson. The author is responsible for all studies in this chapter. The content in this chapter has been published in [91].

4.1 Overview

Among all modelling processes involved in diesel combustion, spray modelling has always been a key component due to its significant impact on fuel injection processes which vastly varies combustion and emission characteristics. On this note, it is essential to develop models that could well predict spray characteristics. The primary objective of this chapter is, therefore (1) to investigate the effect of the grid resolution in high-velocity fuel spray, and (2) to understand the sensitivity of different physical models to integral spray quantities and mixture formation.

The evaporating non-reacting spray results are validated by the comparison of key physical characteristics (liquid penetration, vapour penetration and radial mean mixture fraction) with literature data.

4.2 ECN Diesel “Spray A”

The engine combustion network (ECN) is a recent initiative within the engines community designed to promote collaborative spray and combustion studies both experimentally and numerically [104]. The ECN database includes different physical properties of diesel sprays including spray liquid and vapour penetration length, IDT and flame LOL. Experimental luminosity data is also available for different spray conditions with different diesel fuel surrogates. In this study, ECN “Spray A” simulations will be investigated and validated against ECN’s high-quality and high-fidelity dataset. “Spray A” is a low-temperature combustion condition relevant to engines that use moderate EGR and have minimal NOx emissions. The injector specifications pertain to modern advanced injection systems with high pressure capability. A sample experimental configuration of “Spray A” can be found in Figure 4.1. In order to yield good combustion recession predictions, a non-reacting spray case is calibrated against the ECN experimental data taken from a constant volume, quiescent, pre-burn combustion vessel. Both liquid penetration and vapour penetration will be examined to ensure a valid non-reacting spray case setup. A detailed description of the experimental setup and test cell conditions can be found in Pickett *et al.*[105]. The combustion vessel is modelled as an 108 mm cubical geometry following the specifications defined by ECN. For reacting studies, different physical characteristics are validated against ECN database including IDT, flame LOL, and temperature luminosity image. All important global measurement definitions for high-velocity fuel sprays are listed in: Table 4.1. All “Spray A” conditions tested within this thesis are listed in Table 4.2.

Table 4.1: Non-reacting parameter definitions

Parameter	Definition
Liquid penetration	Axial distance encompassing 97% of injected fuel mass
Vapour penetration	Maximum distance from the injector to where the fuel mass fraction is 0.001

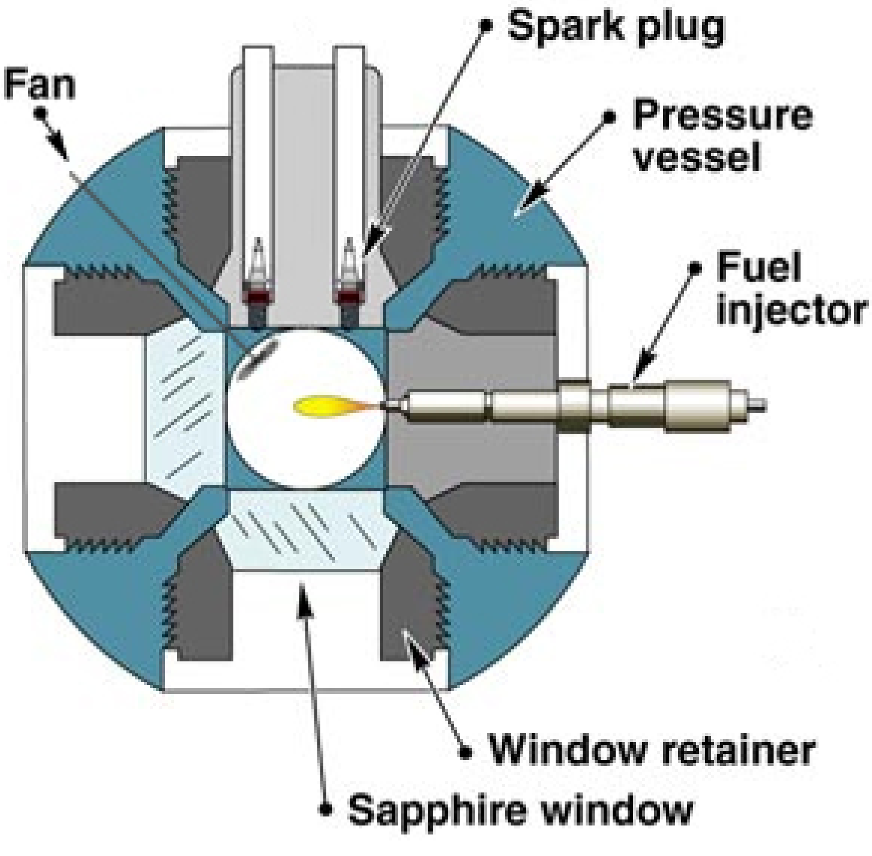

Figure 4.1: "Spray A" experimental setup for Sandia Spray A test rig, adapted from [107].

Table 4.2: "Spray A" testing conditions

Test Type	**Non-reacting**	**Reacting**
Fuel surrogate	n-dodecane	
Ambient gas density (kg/m^3)	22.8	
Ambient gas pressure (bar)	60	
Fuel injection pressure (bar)	1500	
Fuel injection temperature (K)	363	
Nozzle diameter (μm)	90	
Injection duration (ms)	1.5	
Injection mass (mg)	3.5	
Ambient temperature (K)	900	800,900,1000
Ambient gas composition [by vol.]	0% O_2 89.71% N_2 3.77% H_2O 6.52% CO_2	15% O_2 75.15% N_2 3.62% H_2O 3.62% CO_2

4.3 Non-reacting Spray Simulation

In this section, the modelling processes of non-reacting sprays are presented in the following order. First, a grid dependency test is performed to select the most appropriate grid size for sub-model tests. Then the influence of collision models, turbulence models as well as turbulence model constants on non-reacting spray liquid and vapour penetration profiles is investigated. A comparison between Sandia data and chosen CONVERGE model simulation results is then presented. Finally, a grid convergence test is conducted to ensure the accuracy of the chosen model. All tests performed in this section follow non-reacting "Spray A" conditions listed in Table 4.2.

4.3.1 Grid Dependency Test

Sprays have been widely modelled using either Eulerian-Eulerian (two-fluid model) or Eulerian-Lagrangian models. One of the biggest challenges associated with these models is uncertainties caused by grid dependency. The reason for these uncertainties lies in the large range of both time and space scales involved in spray sub-models.

Tonini *et al.* pointed out that accurate numerical results require a spatial resolution that offers a bigger volume compared to droplet size while still be accurate enough to solve the gas phase development near nozzle [146]. A great amount of research work has been conducted to resolve the grid dependency of spray modelling while keeping the simulation cost low. Beard *et al.* extended the conventional Eulerian-Lagrangian approach specifically to diesel spray, which improved the liquid vapour transport behaviour and the momentum coupling between liquid-gas interactions [7]. Different approaches were also proposed to overcome this challenge through implementing new sub-models [123][124] or combining Eulerian-Eulerian and Eulerian-Lagrangian methods [148]. Although these methods were able to achieve grid-independent solutions, the increasing grid density made them unsuitable for engine calculations. With this in mind, adaptive mesh refinement (AMR) becomes more appealing for diesel spray simulations. Previous works from different researchers have also shown great accuracy in engine spray modelling using AMR [126][73]. Therefore for testing the effects of different sub-models and model constants in this study, AMR will be used as the primary spatial discretization method. Simulations performed in this study are carried out using a commercially-available CFD code, CONVERGE. CONVERGE uses an innovative, modified cut-cell Cartesian method, which allows automated grid generation. For non-reacting cases, AMR is applied to the velocity field, and in reacting cases, AMR is applied to both velocity and temperature fields. AMR is activated when the sub-grid fluctuations of the velocity or the temperature field rise above a certain user-defined value; in this study, it was set at 0.1 ms^{-1} and 2.5 K respectively. Fixed grid embedding is also applied to a small volume near the nozzle exit to increase grid resolution in this high-velocity region. A sample grid configuration can be found in Figure 4.2.

Studies have also shown spray penetration in near nozzle regions depends heavily on the rate of injection (ROI) characteristics. Therefore, instead of using the measured ROI profile for “Spray A”, a modified profile from ECN database which accounts for noise and vibrations is used in the current study.

As mentioned earlier, grid dependency plays an essential role due to its direct

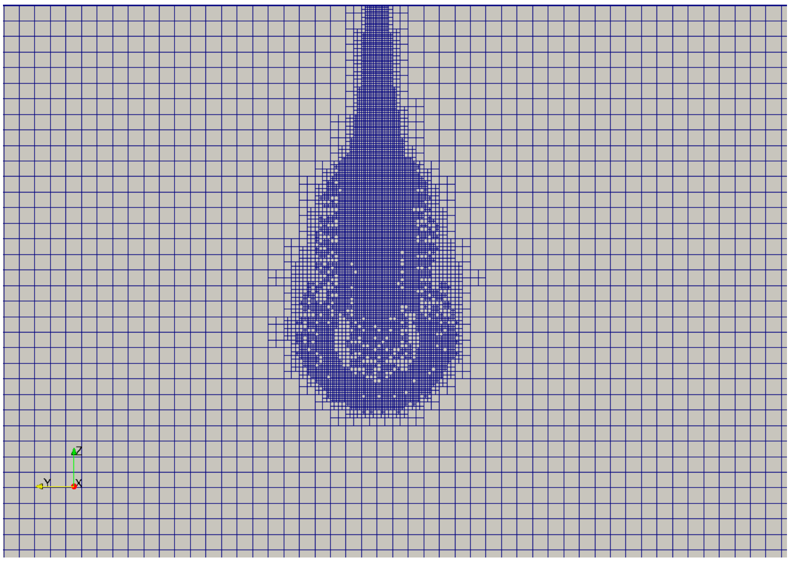

Figure 4.2: “Spray A” computational domain with minimum 0.25 mm grid size

linkage to the Eulerian-Lagrangian spray approach. In order to determine the best grid size for testing non-reacting cases, a grid sensitivity test was conducted using the standard “Spray A” case setup in CONVERGE. The case uses the RNG $k-\epsilon$ turbulence model, the NTC collision model and the KH-RT break-up model. The KH-RT model is very sensitive; therefore the model constants B_1 (KH break-up timescale constant) and C_τ (RT break-up timescale constant) are tuned to match the transient and quasi-steady non-reacting liquid length as well as the vapour penetration length of the baseline “Spray A” conditions. The inherent grid sensitivity of the KH-RT model shows that for each case setup, specific adjustment of break-up model constants is required to match the experimentally measured liquid and vapour length. However, for the study of grid sensitivity, the constants within the KH-RT model remain unchanged. With these in mind, a grid sensitivity test was conducted using the smallest grid size of 0.0625 mm and the biggest 2 mm. Six different mesh resolutions were tested using the CONVERGE case setup. The AMR embed scale and its corresponding minimum cell size and number of injected parcels are listed in Table 4.3.

Table 4.3: AMR embed scale corresponding cell size and number of injected parcels

Embed Scale	Cell Size (mm)	Number of Injected Parcels
0	2.0	2,000
1	1.0	16,000
2	0.5	128,000
3	0.25	512,000
4	0.125	2,048,000
5	0.0625	8,192,000

Figure 4.3 shows the grid dependency of the liquid and vapour penetration. For vaporizing non-reacting spray cases, the measured liquid penetration increases until it reaches a quasi-steady liquid length of 10 mm. However, with a grid size greater than 0.5 mm, the quasi-steady state liquid length is significantly higher than the experimental data and the results show a very high level of instability. For cell sizes 0.25 mm and finer, the liquid length is accurately captured. Figure 4.4 plots the quasi-steady liquid penetration over the range of grid sizes. It is clear that liquid length exhibits grid convergence characteristics behaviour with promising results starting from 0.25 mm (embed scale 3) grid size. Similarly, vapour penetration is also better represented using a grid size less or equal to 0.25 mm. From these studies we can draw the conclusion that an AMR mesh with a minimum cell size 0.25 mm can predict sufficiently accurate spray characteristics with acceptable runtime. This conclusion is identical to the findings of Senecal *et al.* in grid convergent tests on spray models [126]. With this conclusion, the following studies on spray sub-models were conducted using 0.25 mm as the minimum AMR grid size.

4.3.2 Physical Computational Models

Although studies have been carried out for governing physical phenomena for decades, when it comes to simulations, results are still very dependent on the accuracy and setup of individual sub-models. A complete physical model study would involve processes like: turbulence, spray injection and liquid droplet dynamics. However, only collision models and turbulence models are studied here as significant

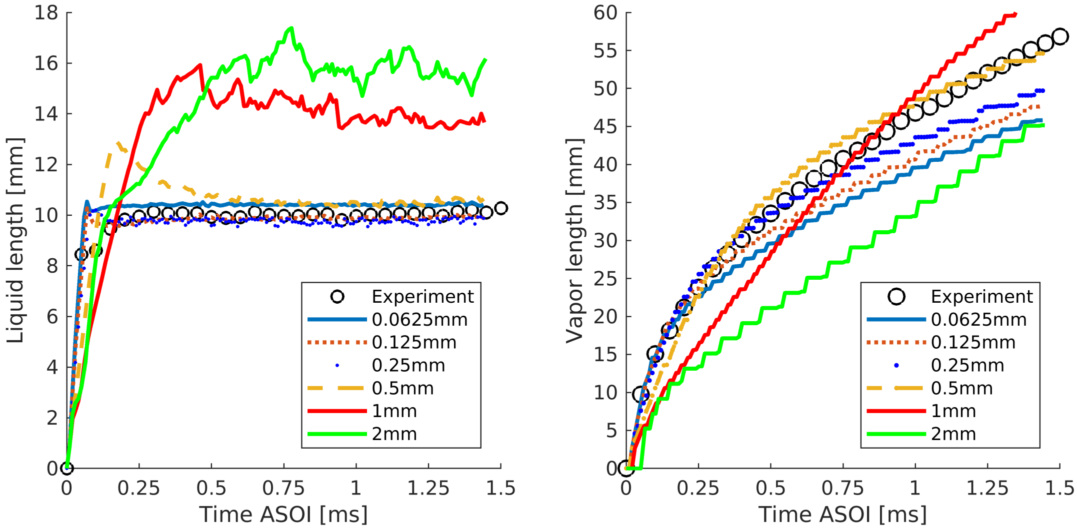

Figure 4.3: Non-reacting spray grid convergence, left: liquid length, right: vapour length

research has been conducted on spray droplet dynamics models. Here the widely adopted "blob" injection model with a semi cone angle of 10 degree is used, in which "parcels" of liquid with a characteristic size identical to the nozzle diameter are injected into the domain [118]. The subsequent atomization and break-up of the liquid blobs is then modelled based on Kelvin-Helmholtz (KH) and Rayleigh-Taylor (RT) instability mechanisms without the use of predefined break-up length [129]. A droplet evaporation model using the Frossling correlation is implemented. A dynamic drag model is used to accurately determine the drag coefficient. A stochastic dispersion model is incorporated to capture the effects of turbulence on droplets. A summary of physical sub-models applied can be found in Table 4.4. For all studies a minimum grid size of 0.25 mm and a variable time step are used.

Collision Models Study

High computational cost and large numerical errors have made droplet collision modelling a great challenge. The most widely used collision model is the O'Rourke model which allows the collision of droplets to occur in a "collision cell" [93]. When determining the probability of colliding parcels, a sub-sample of droplets are tracked;

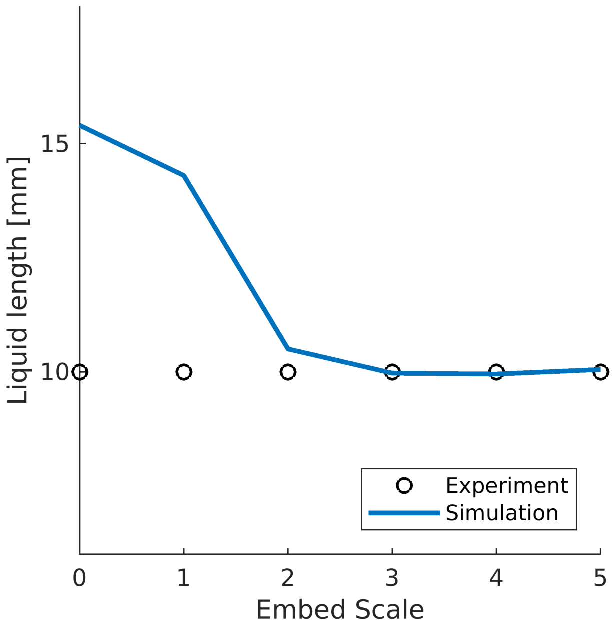

Figure 4.4: Liquid penetration vs embed scale for non-reacting spray at 900 K conditions. The embed size is detailed in 4.3.

only parcels with the same gas-phase cell are allowed to collide with each other. Although this approach gives a second-order accuracy in space, it further raises the grid dependency problem mentioned earlier. The tracking mechanism used in this method also incurs a computational cost that increases with the square of the number of parcels.

A more recent collision model from Schmidt and Rutland is the no time counter (NTC) model [123]. The NTC model includes stochastic sub-sampling of parcels within each drop, which significantly reduces computational costs. Another advantage of the NTC model lies in the usage of a collision mesh. Unlike the O'Rourke model, the NTC model does not use the gas-phase mesh for collision calculations. Instead, an automatically generated mesh around the axis of injection is calculated. The fine mesh resolution allows the NTC model to have high-resolution collision calculations.

Figure 4.5 shows the influence of the collision models on both the liquid and vapour penetrations. Two collision models, the O'Rourke and the NTC are implemented

Table 4.4: Modeling setup for non-reacting simulations at 900 K conditions

Model Setup	**Tested models**
Turbulence Models	Standard $k-\epsilon$, RNG $k-\epsilon$, Realizable $k-\epsilon$
Spray Models	
Injection models	Blob
Atomization and Break up	KH-RT
Collision	NTC, No Collision, O'Rourke
Drag	Dynamic
Evaporation	Frossling
Dispersion	Stochastic
Heat Transfer	Ranz-Marshall
Grid	
Type	Structured with AMR
Dimensionality	3D
Grid Sizes	0.0625mm - 2mm
Time Step	Variable Time Step

under the same conditions. The results indicate that the NTC model predicts liquid penetration well, whereas the O'Rourke model gives an overprediction on liquid penetration. This can be explained by the higher collision mesh resolution generated by the NTC model, which allows more accurate gas-liquid interactions. Also, the assumption made by the O'Rourke model that multiple collisions between parcels are governed by a Poisson distribution is less physical. The Poisson distribution only stands when collisions have no impact on the parcels. Since the collision of parcels will inherently change a parcel's velocity, size, and number, the method of repeated sampling from the NTC model would give a better and more physical result. Based on these tests, the vapour penetration is found to be independent of the collision model. In addition, the NTC model has a computational cost that is linear with the number of spray parcels, while the O'Rourke model has a cost that increases with the square of the number of the parcels. As a result, the NTC model allows for a better statistical and physical representation of the spray with less computational time. Therefore, the NTC model is chosen as the collision model.

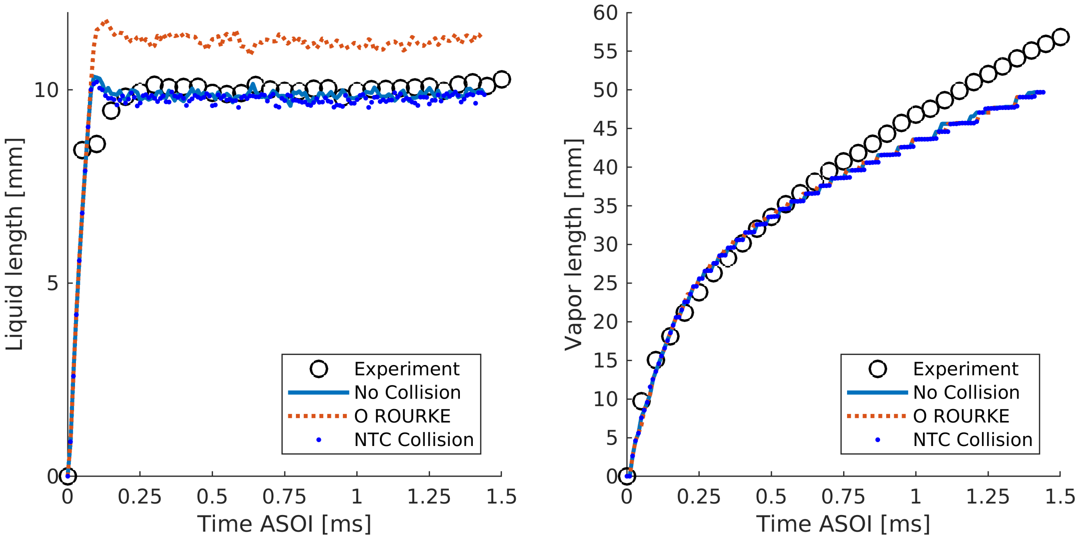

Figure 4.5: Non-reacting spray collision models study at 900 K conditions, left: liquid length, right: vapour length

Turbulence Models Study

Among all RANS turbulence models, the two-equation $k - \epsilon$ model has shown great promise in spray modelling. The $k - \epsilon$ model is popular in practical applications due to its simplicity and cost-effectiveness. Pandurangi *et al.* studied transient soot formation processes in high-pressure n-dodecane sprays under diesel engine conditions using the standard $k - \epsilon$ turbulence model [96]. The results were well matched in reactive jet penetration. Kim *et al.* examined the end of injection combustion transients in diesel sprays using the standard $k - \epsilon$ model, which qualitatively captured the combustion recession process [59]. Based on non-reacting validation tests in this study, both the liquid and vapour penetrations are consistent with experimental data. Blomberg *et al.* studied n-dodecane split injection under "Spray A" conditions using the standard $k - \epsilon$ model with modified constants [19]. The obtained liquid and vapour penetrations from the simulation were consistent with both experimental and LES simulation results.

To extend the usage of the $k-\epsilon$ model, Yakhot *et al.* developed the so-called RNG $k-\epsilon$ model to capture features of swirling and sheared turbulent flows [165]. In order to account for smaller scales of motion, the effect of mean flow distortion on turbulent kinetic energy dissipation rate is also included in the model. The RNG $k-\epsilon$ model has been successfully adapted to non-reacting and reacting spray modelling. Senecal *et al.* used the RNG model to verify key components of grid convergence for non-reacting and reacting spray cases [126]. Senecal *et al.* also used the RNG model together with a detailed chemistry model to accurately predict ignition delay and engine cylinder-averaged pressure [128]. Som *et al.* compared the spray characteristics predicted by different CFD software using the RNG $k-\epsilon$ turbulence model [135]. The results show good agreement between two different commercial programs in most key parameters, although the flame lift-off length is better captured in CONVERGE.

One last two-equations model examined in this study is the realizable $k-\epsilon$ model. First proposed by Shih, the realizable $k-\epsilon$ model is the newest variation of the standard $k-\epsilon$ turbulence model [131]. New turbulent viscosity and dissipation rate transport equations were adopted. The realizable $k-\epsilon$ model allows a variable empirical constant C_μ, which is a function of mean strain and rotational rates, turbulent kinetic energy and its dissipation rate. This $k-\epsilon$ model shows better prediction in flows with separation features as well as with complex secondary flow features. Recent application of the realizable $k-\epsilon$ by Jarrahbashi *et al.* shows good agreement with the experimental results in both reacting and non-reacting sprays [55]. The model was also able to qualitatively capture end-of-injection transients based on past experiments.

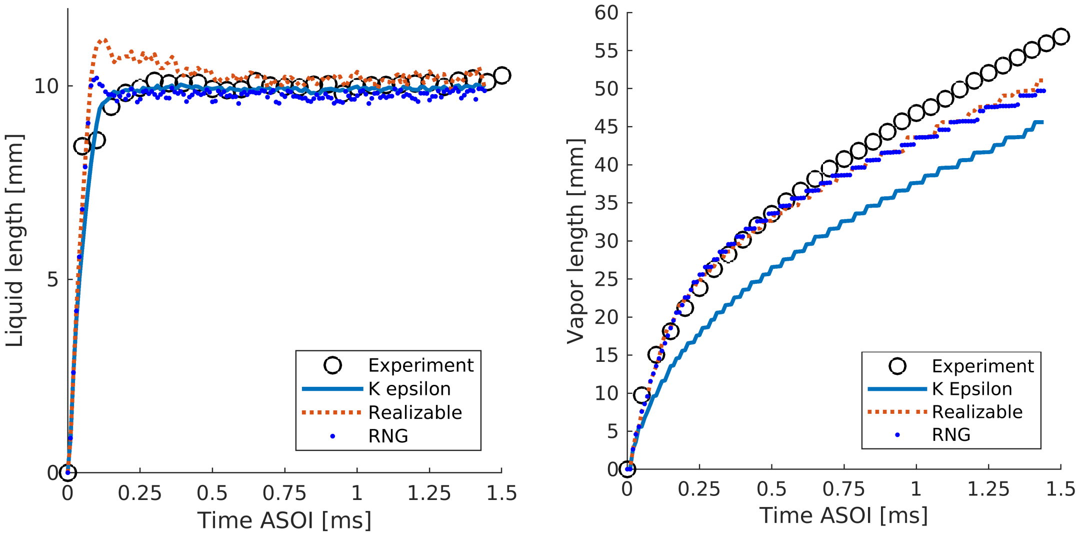

Figure 4.6: Non-reacting spray turbulence models study at 900 K conditions, left: liquid length, right: vapour length

Figure 4.6 shows the influence of the RANS turbulence models on both the liquid and vapour penetration. Three different RANS turbulence models were tested as mentioned earlier: Standard $k-\epsilon$, RNG $k-\epsilon$ and Realizable $k-\epsilon$. The test results show that the liquid penetration is essentially independent of the chosen turbulence model with the Realizable $k-\epsilon$ slightly overshooting during the initial transient, while the standard $k-\epsilon$ model better matches the experimental results. However, turbulence models play a significant role in predicting vapour penetration. With standard coefficients, the RNG $k-\epsilon$ model presents a better prediction among the three turbulent models tested, whereas the standard $k-\epsilon$ model significantly underpredicts the vapour penetration. However, all three models underpredict the vapour penetration at the end of injection time, which is of great interest to this study. As mentioned before, both RNG $k-\epsilon$ and Realizable $k-\epsilon$ models include additional terms required to accurately solving the dissipation rate. Therefore it is also worth investigating the influence of modelling constant in the standard $k-\epsilon$ model where dissipation rate is solved. To isolate this effect, the constant $C_{\epsilon 1}$ describing the production of turbulent dissipation in the $k-\epsilon$ dissipation rate transport equation is altered.

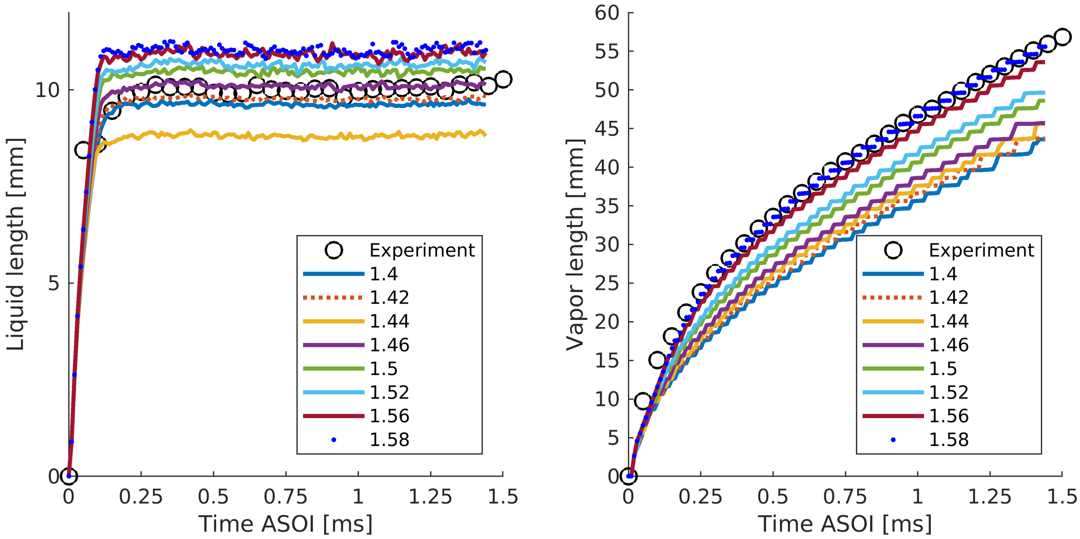

Figure 4.7: Non-reacting spray $k-\epsilon$ turbulence model constant study at 900 K conditions, left: liquid length, right: vapour length

Figure 4.7 shows the impact of constant $C_{\epsilon 1}$ on the standard $k-\epsilon$ model. Both liquid and vapour penetration increase with increasing $C_{\epsilon 1}$ constant. The results show that with a constant value of 1.58, accurate prediction of the vapour penetration is achieved; however, the steady-state liquid penetration is overpredicted. In order to overcome the overprediction of liquid penetration, additional modelling efforts were conducted to alter the break-up constants within the KH-RT model to give the most accurate liquid penetration as well as vapour penetration. Based on previous studies, different $k-\epsilon$ model constants were also implemented to achieve better non-reacting spray results. Blomberg et al. used 1.52 as their $C_{\epsilon 1}$ constant which accurately captured vapour penetration [19], whereas Kim *et al.* implemented standard coefficients for the $k-\epsilon$ model [59]. Similar constant tests were also conducted on the RNG $k-\epsilon$ and the Realizable $k-\epsilon$ models to improve the model performance in predicting initial transient liquid penetration and end of injection vapour penetration. However minimal impact was found, with both models resulting in overshoot during the initial transient stage in liquid penetration and a slightly lower vapour penetration at the end of injection. Therefore, the standard $k-\epsilon$ model with modified model constants was chosen for spray simulations.

4.4 Summary

The non-reacting spray study focused on demonstrating the influence of several key components in spray modelling. The resulting model uses a minimum grid size of 0.25 mm, variable time step with 10^{-8} s initial time step, the standard $k-\epsilon$ model with modified constants and an NTC collision model. Figure 4.8 shows good agreement between the measured and simulated liquid and vapour penetration during both initial ramp-up period and steady state period. The slight underprediction for transient vapour penetration is likely caused by CONVERGE's binning strategy which can be optimized for future studies. Additionally, mixture fraction distributions both axially and radially are compared to the available ECN Rayleigh scattering measurements. The radial mixture fraction distribution is predicted reasonably well for both two axial locations as shown in Figure 4.8. It can be seen that the RANS model slightly overpredicts the mixture fraction at the liquid core which is consistent with other simulations using similar models and gird resolutions [19]. As shown in the right of Figure 4.8 the overprediction in liquid core are greatly improved when moving away from the centerline and overall the predictions are well within the variance of experimental measurements. It is evident that the selected model can accurately represent the fuel-air distribution under steady state "Spray A" conditions. Although transient condition fuel-air distribution is not validated due to the lack of measured data, a good prediction of air-fuel distribution at steady state and a good vapour penetration during transient stage can constitute an accurate representation of spray air-fuel distribution for reacting cases.

Finally a grid convergent test is again performed to ensure the convergence of each selected model. The grid size is chosen from a maximum of 0.5 mm to a minimum of

0.0625 mm. Figure 4.9 concludes that when the grid size is less or equal to 0.25 mm the selected model is indeed converged for both liquid and vapour penetration.

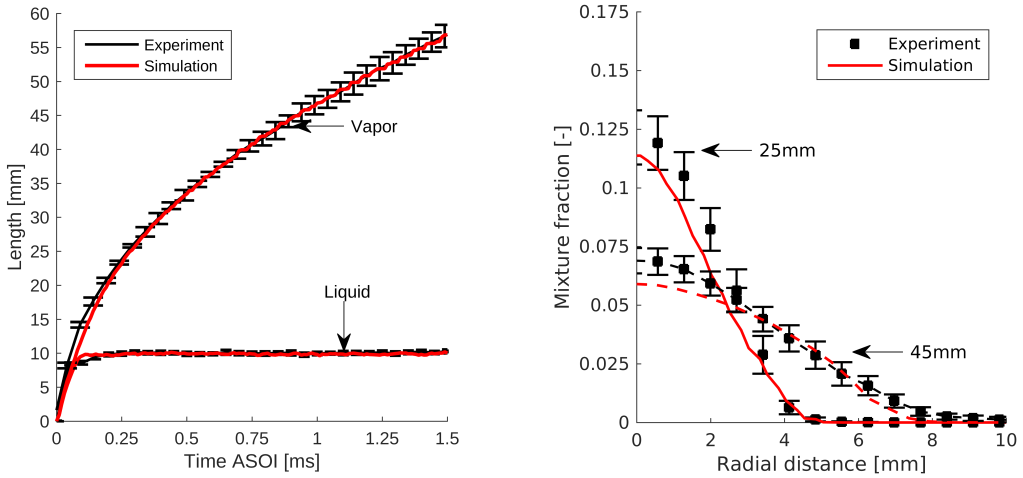

Figure 4.8: Non-reacting spray final model at 900 K conditions, left: liquid and vapour length, right: radial mixture fraction distribution

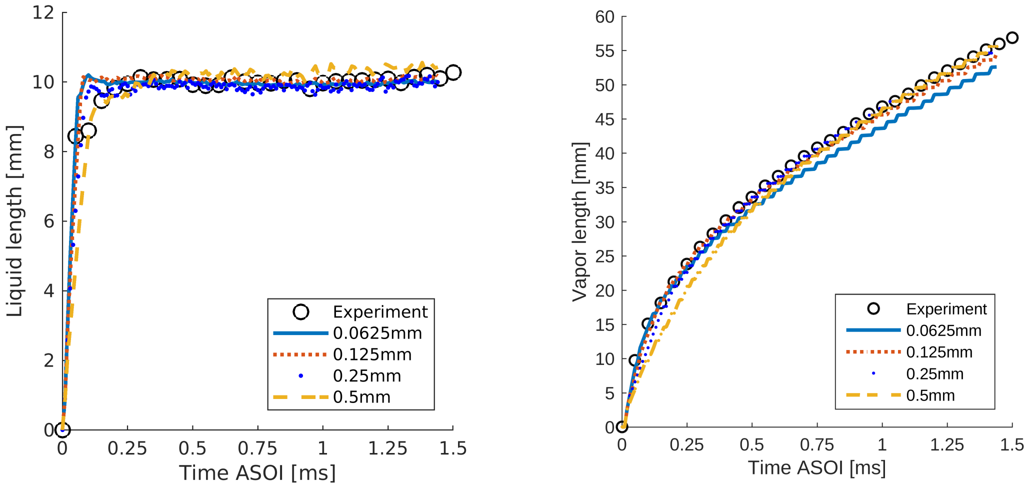

Figure 4.9: Non-reacting spray final model grid convergence study at 900 K conditions, left: liquid length, right: vapour length

Research is what I'm doing when I don't know what I'm doing.

—Wernher von Braun

5

Application of a Tabulated Chemistry Combustion Model in Simulation of Combustion Recession

Contents

The content in this chapter is a result of the collaborative efforts of the author, Dr Riyaz Ismail and Dr Joseph Camm. The author is responsible for all studies using CONVERGE software. The content in this chapter has been published in [35].

5.1 Overview

The primary objective of this chapter is to assess the ability of a flamelet generated manifold (FGM) combustion model to predict and characterise combustion recession. The non-reacting case set-up is taken from previous work detailed in Chapter 4.

First, a detailed study on an FGM modelled reacting spray is conducted with a study of ignition delay time (IDT), flame lift-off length (LOL) and general flame structure. A baseline FGM simulation is compared with two other combustion models, namely the well-stirred reactor model (WSR), the representative interactive flamelet model (RIF) using the commercially-available CFD solver, CONVERGE. Further studies are performed to investigate the FGM model's performance subject to the variation of "Spray A" temperature conditions and the application of two different n-dodecane chemical kinetics mechanisms: Cai *et al.* [20] with 57 species and 197 reactions (referred to as the Cai mechanism), and Yao *et al.* [166] with 54 species and 268 reactions (referred to as the Yao mechanism). All simulations are performed under the Reynolds-averaged Navier-Stokes (RANS) framework in a grid-converged Lagrangian spray scenario. The simulation of the FGM model is qualitatively and quantitatively validated against experimental data from the literature, and the efficacy of FGM model in predicting combustion recession is evaluated.

5.2 Combustion Models

In this section, a brief description of the different combustion models used in this study is presented. The CONVERGE-implemented SAGE and RIF combustion models will be discussed first, followed by a more detailed description of the FGM model, which is the focus of this chapter. The results of reacting spray using FGM will then be discussed afterwards with a study of ignition delay, flame lift-off length and general flame structure.

5.2.1 Well Stirred Reactor Model (SAGE)

The principal idea behind the well-stirred reactor model is that the mixing in a turbulent field is considered infinitely fast compared to chemistry and the species within each cell are assumed to be homogeneously distributed. SAGE is a well-stirred reactor combustion model implemented in CONVERGE, where the mean reaction rates for each elementary reaction are directly integrated based on Arrhenius type correlations. Only first-order moments, or the mean of scalars, are considered in this calculation. Given an accurate chemical mechanism, SAGE can be used for different combustion regimes. Previous studies have shown successful predictions of diesel spray liquid length and flame LOL [128] [135]. SAGE has also been used in practical engine simulations with favorable results [72]. Despite successful simulations in diesel sprays, studies using the well-stirred reactor assumption can have large errors due to the highly non-linear behavior of the mean chemical source term and the lack of turbulent chemistry interactions within the model. Furthermore, the computational cost for the SAGE model can be greatly increased if detailed chemical kinetics are used.

5.2.2 Representative Interactive Flamelet Model (RIF)

RIF is based on the laminar flamelet concept detailed in Chapter 3, where a turbulent diffusion flame is treated as an ensemble of laminar flamelets. The local chemical composition is determined through the statistical description of the laminar flamelet solution associated with the mixture fraction variable, Z. Species equations are transformed into mixture fraction space, with an assumption that mixture fraction sub-grid distribution can be represented by a β-pdf. The transformed species mass fraction equations and β probability density function are written as:

$$\tilde{Y}_i(x_i,t) = \int_0^1 \tilde{P}(Z;x_i,t)Y_i(Z,t)dZ \tag{5.1}$$

$$P(Z,\tilde{Z},\widetilde{Z''^2};x_i,t) = \frac{Z^{\alpha-1}(1-Z)^{\beta-1}}{\Gamma(\alpha)\Gamma(\beta)}\Gamma(\alpha+\beta) \tag{5.2}$$

where $\alpha = \bar{Z}\gamma$, $\beta = (1-\tilde{Z})\gamma$, and $\gamma = \tilde{Z}(1-\tilde{Z})/\widetilde{Z''^2} - 1$

As shown in Equation 5.1, accounting for turbulent chemistry interactions, RIF requires solving the local statistics of the Favre averaged mixture fraction $\tilde{Z}$ and its variance $\widetilde{Z''^2}$. The conservation equations for the mean and variance of the mixture fraction are given by:

$$\frac{\partial(\tilde{\rho}\tilde{Z})}{\partial t} + \frac{\partial}{\partial x_i}(\tilde{\rho}\tilde{u}_i\tilde{Z}) = -\frac{\partial}{\partial x_i}(\tilde{\rho}\widetilde{u_i''Z''}) + S \tag{5.3}$$

$$\frac{\partial(\tilde{\rho}\widetilde{Z''^2})}{\partial t} + \frac{\partial}{\partial x_i}(\tilde{\rho}\tilde{u}_i\widetilde{Z''^2}) = -\frac{\partial}{\partial x_i}(\widetilde{\tilde{\rho}u''_i Z''^2}) - 2(\widetilde{\tilde{\rho}u''_i Z''^2})\frac{\partial\tilde{Z}}{\partial x_i} - \tilde{\rho}\tilde{\chi} \tag{5.4}$$

Where S is the spray source term and the scalar dissipation rate $\tilde{\chi}$ can be modeled as:

$$\tilde{\chi} \cong C_\chi \frac{\tilde{\epsilon}}{\tilde{k}} \widetilde{Z''^2} \tag{5.5}$$

where C_χ is a constant and $\tilde{\epsilon}$ is the turbulent dissipation.

Unlike laminar flamelet models, RIF can also incorporate different unsteady flamelet histories in order to capture rapid change of the mixing field, this is particularly important in the RIF model's application to diesel combustion. Each flamelet within a RIF calculation represents a certain portion of injected fuel mass and the chemical composition in each cell is computed from the mixture fraction. For the simulations performed in this study 20 flamelets are incorporated to reflect the unsteady nature of turbulent diffusion flames. The chosen number of flamelets is based on prior studies carried out by Kim *et al.* [59].

5.2.3 Flamelet Generated Manifold Model (FGM)

The principal idea of FGM [94] based models is derived from reduced chemistry models that are based on dimensional reduction techniques and flamelet models. The FGM method describes the turbulent flame structure by pre-tabulating one-dimensional flamelets using a reduced number of control variables. It decouples the solving procedure of the flame structure from the turbulent flow field by mapping the representative flamelet solutions on a low-dimensional manifold in composition space. The resultant FGM table can be used to simulate multi-dimensional reacting flow without solving additional transport equations for all species. The flamelet equations as given by Stahl and Warnatz [139] read:

$$\frac{\partial\rho}{\partial t} + \frac{\partial}{\partial x}(\rho u) = -\rho K \tag{5.6}$$

$$\frac{\partial\rho Y_i}{\partial t} + \frac{\partial\rho u Y_i}{\partial x} = \frac{\partial}{\partial x}\left(\rho D\frac{\partial Y_i}{\partial x}\right) + \dot{\omega}_i - \rho K Y_i \tag{5.7}$$

$$\frac{\partial \rho h}{\partial t} + \frac{\partial \rho u h}{\partial x} = \frac{\partial}{\partial x}\left(\frac{\lambda}{c_p}\frac{\partial h}{\partial x}\right) - \rho K h \tag{5.8}$$

where K, is the stretch rate of flame stretch field and unity Lewis number is assumed thereby the diffusion coefficient, $D = \frac{\lambda}{\rho c_p}$.

In this study, the choice of flamelet is that of a 1D non-premixed laminar counterflow diffusion flame (shown in Figure 5.1) with solutions computed in physical space and time using the Chem1D code [22]. FGMs can be generated in many different ways. For stationary flames, the manifold can be generated using a sequence of steady flames solutions with strain rates varying from the lowest value to the quenching value. However, for a spray simulation, it is unsteady and initially non-reacting. Therefore, additional information is required to account for unsteady events in spray simulation. Several ways exist to cover the transient events in FGM models. One way is to solve a time-dependent flamelet with a higher strain rate than the highest possible non-quenching strain rate, which forces the flame to extinguish and in the meantime filling the manifold with quenching flamelet solutions. Another approach is to solve time-dependent flamelets from a mixed, but non-reacting initial state. The ignition behaviour is followed in time until a steady-state flame is reached. Figure 5.2 shows the schematic of completing the Z-c space manifolds using these two different approaches.

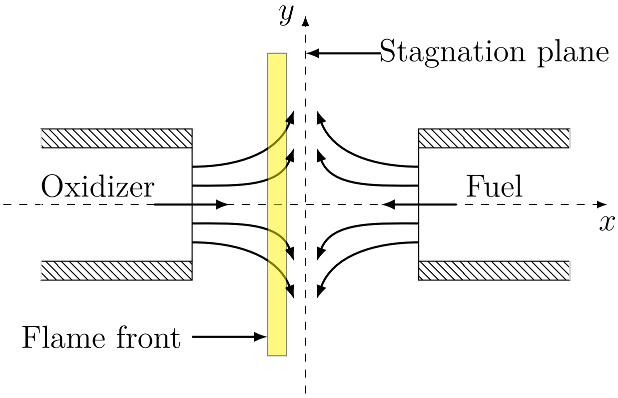

Figure 5.1: Schematic of laminar non-premixed counterflow diffusion flame

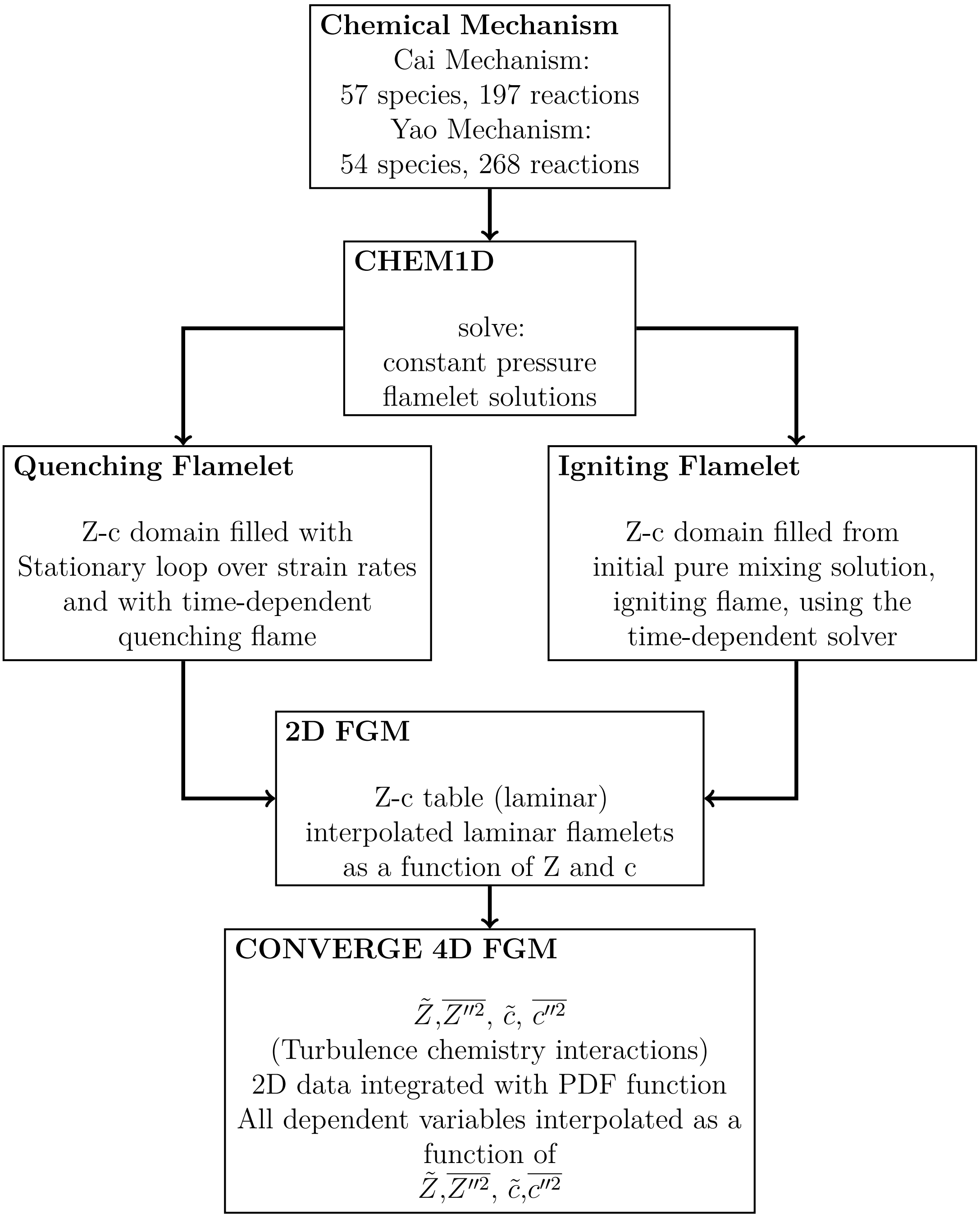

Figure 5.2: FGM solution construction scheme

Previous study has shown that generating unsteady flamelets using quenching flamelets does not lead to ignition of diesel sprays. Therefore, for this study, an FGM is constructed using an igniting flamelet database. The one-dimensional laminar counterflow diffusion flame is solved in physical spaces with the CHEM1D code, where an example of temperature evolution as a function of space and time can be found in Figure 5.3. The generation of the manifold first starts with solving a transient counterflow diffusion flame at a strain rate of 500 s^{-1} from an initially mixed, but non-reacting state and then tracking this flame through ignition up until quasi-steady-state (QSS). Following this, steady-state flamelets are solved from 500 s^{-1} down 1 s^{-1} to complete the manifold close to chemical equilibrium. The choice of 500 s^{-1} as the highest non-quenching strain rate has been determined from literature where Wehfritz *et al.* [159] showed ignition delay times to be insensitive to strain rate in the range of $a < 1000$ s^{-1}. Bekdemir *et al.* [8] also found that for moderately strained configurations, a single unsteady flamelet was able to adequately capture the ignition process.

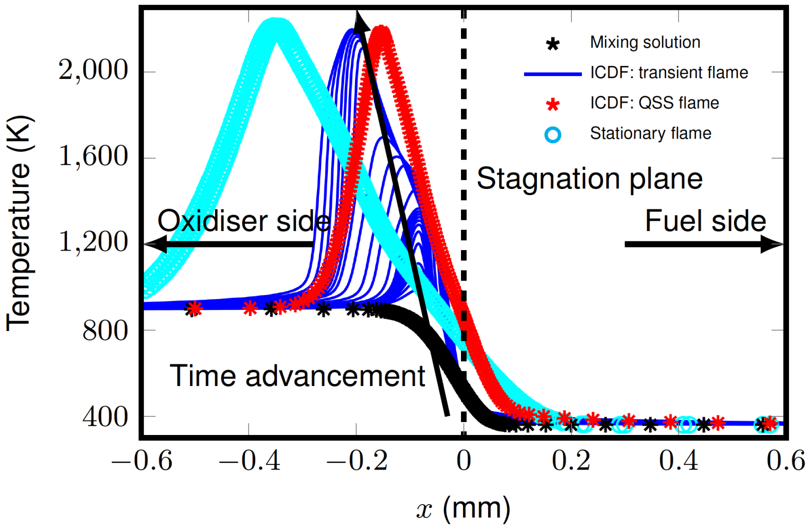

Figure 5.3: Temperature evolution T(x,t) obtained for the Cai mechanism at 900k reacting “Spray A” conditions

Once the flamelet solutions are computed, they are parameterized against mixture fraction, Z, mixture fraction variance, Z''^2 and reaction progress variable, c

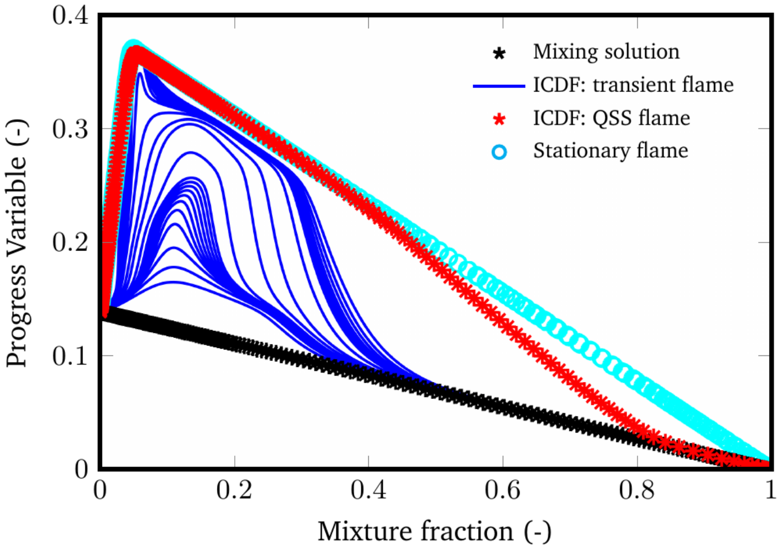

Figure 5.4: Flamelet solutions in progress variable-mixture fraction space for a counterflow diffusion flame using the Cai mechanism at 900 K reacting "Spray A" conditions

with a manifold resolution of 100x10x100 quadratically spaced points respectively. Quadratic spacing ensures refinement near stoichiometry, ensuring interpolation accuracy during the early phases of ignition as described by Eguz *et al.* [32]. The reaction progress is a monotonic variable that captures each stage of combustion evolution, which is defined as a linear combination of three key species (CO, CO_2 and CH_2O) normalized by their equilibrium value:

$$c = \frac{\sum \alpha_i Y_i}{\sum \alpha_i Y_i^{eq}} \tag{5.9}$$

The inclusion of CH_2O is inspired by the notion that it is significant at the start of the ignition process, where CO represents the intermediate stage of combustion and subsequently CO_2 represents the end of combustion process. The values of the weights in this study were kept at the default recommended values of CONVERGE-CFD, which are 1 for all species. It is to be noted here that the definition of progress variable, c, will not affect results as long as the chemistry parameterization (selection of species) represents each stage of chemistry evolution and is monotonic. The monotonicity of the progress variable is ensured during the parametrization process leading to a consistent FGM. A sample resultant manifold in Z-c space can be seen in Figure 5.4. To account for turbulence chemistry interactions, the manifold is integrated with a β-function for Z and delta-functions for Z''^2 and c. Note that effect of c''^2 is omitted due to its insignificant effect on ignition prediction, hence δ-function is used for c''^2 .

It should be noted that unlike conventional FGM implementations [159], the mean reaction progress source term is not looked-up in the FGM database but it is computed via a kinetic rate model as:

$$\bar{\rho}\bar{\dot{c}} = \int_0^1 \int_0^1 \left(\frac{\sum \alpha_i \dot{\omega}_i}{\sum \alpha_i Y_i^{eq}} \right) P(Z_{FGM}) \delta(c - \tilde{c}) dc dZ_{FGM} \tag{5.10}$$

In Equation 5.10, $\dot{\omega}_i$ is the reaction rate of the i^{th} species, $P(Z_{FGM})$ is the Z-PDF and $\delta(c - \tilde{c})$ the c-PDF. Further details on this model can be found in [128]. The coupling of the FGM database with the CONVERGE flow solver is achieved via a represented set of species mass fractions which is stored in a manifold as a function of Z, Z''^2 and c. For this study, 15 representative species are considered for the respective chemical mechanism. Figure 5.5 shows sample hydroxide (OH) manifolds at “Spray A” conditions for both chemical mechanisms tested in this study.

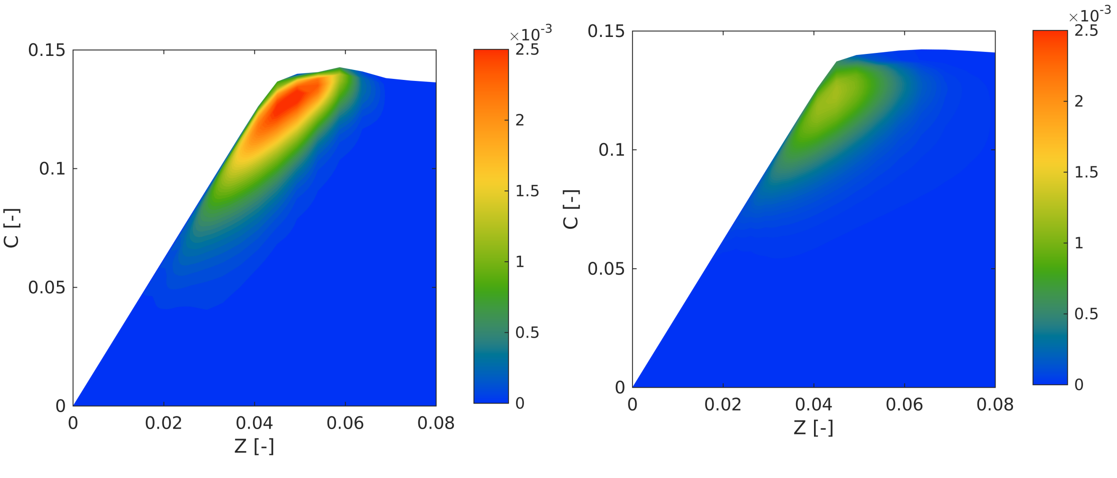

Figure 5.5: FGM Y_{OH} mass fraction for both chemical mechanisms at 900K reacting test conditions, left: Cai, right: Yao

5.2.4 Results and Discussions

The validity of the implemented FGM model is first examined by comparing the model with current CONVERGE combustion models under the “Spray A” baseline conditions (900 K reacting conditions listed in Table 4.2) with the Cai mechanism. In standard ECN experimental measurements, both flame lift-off length and ignition delay are measured using high-temperature chemiluminescence to detect light emitted from the OH* radical. For flame lift-off length, the OH* signal is integrated over a 0.5 ms duration when the flame has stabilised to provide a time-averaged OH* image. The flame lift-off length is then computed by taking the first axial location in this image that reaches 50% of the levelled-off OH* signal intensity. In a similar manner to flame lift-off length, the ignition delay is computed as the first time instance that the OH* signal intensity level reaches the 50% levelled-off intensity threshold value. Further details on experimental diagnostics can be found in [103]. As most n-dodecane mechanisms do not include OH* reactions, the agreed-upon definitions for flame lift-off length and ignition delay by ECN members for CFD comparisons are given in Table: 5.1.

Table 5.1: Reacting spray parameter definitions

Ignition delay time (IDT)	First time at which Favre averaged OH mass fraction reaches 2% of the domain maximum after steady state is established
Flame lift-off length (LOL)	Distance from the injector to the first location where the Favre averaged OH mass fraction reaches 14% of the instantaneous maximum during the steady state period

Table 5.2: Baseline combustion model comparison

Model	SAGE	RIF	FGM	Experiment
IDT (ms)	0.547	0.569	0.281	0.40-0.45
LOL (mm)	24.00	24.55	17.71	15.80-17.90

Table 5.2 shows both IDT and LOL for the three different combustion models under the above mentioned conditions. All models are able to capture the IDT reasonably well, with the SAGE and RIF models overpredicting and the FGM model slightly underpredicting the IDT when compared to the experimental data. When looking at the LOL predictions, the SAGE and RIF models significantly over-predict the LOL when compared to the experimental data, whereas the FGM

model prediction of LOL shows a close match with only a ∼1 mm deviation from the mean experimental results. Interestingly, previous studies of Jarrahbashi *et al.* [55] and Kim [59] have shown similar results for both SAGE and RIF models with slight overpredictions in both IDT and LOL. In the SAGE model, the inaccuracy is likely to be caused by the lack of representation of turbulence and strain effects on the diffusion flame, which is an inherent problem with well-stirred reactor models. Due to the incorporation of presumed PDF statistics in the RIF model, a wider reaction zone and a more diffused OH field resulting in higher IDT and overprediction of LOL are expected. For the FGM model, the underprediction of IDT is likely caused by higher formaldehyde and hydroxyl concentration in mixture fraction and progress variable space presented in the FGM manifolds. Figure 5.5 shows that under the same mixing conditions, the tabulated flamelet solutions for the Cai mechanism tend to have a higher hydroxyl mass fraction compared to the mechanism of Yao. Previous studies [159] have also shown that onset production of formaldehyde prior to ignition could vary between each mechanism. With this in mind, Figure 5.6 shows the temperature contours for the baseline flame at t=1.3 ms (-0.1 ms ASoR) and t=1.8 ms (+0.4 ms ASoR) for all three chemical models. For the steady-state flame (t=1.3 ms), all three models show similar flame penetration length with the SAGE model predicting the highest temperature as expected due to the exclusion of higher-order non-linear mixing in turbulent chemistry and the RIF model predicting a more diffused temperature field. Compared to other models, the FGM model produces a slight narrower span of the reaction zone with the predicted temperature being lower compared to that of the SAGE model. The narrower reaction zone can be linked to the progress variable source term being calculated using a kinetic model. This phenomenon can also be seen in a recent study using a traditional RANS-FGM modelling approach conducted by Kim *et al.*[58].

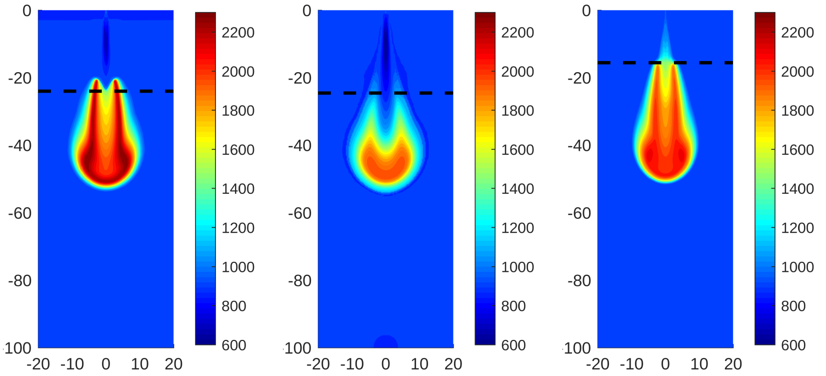

(a) SAGE (b) RIF (c) FGM

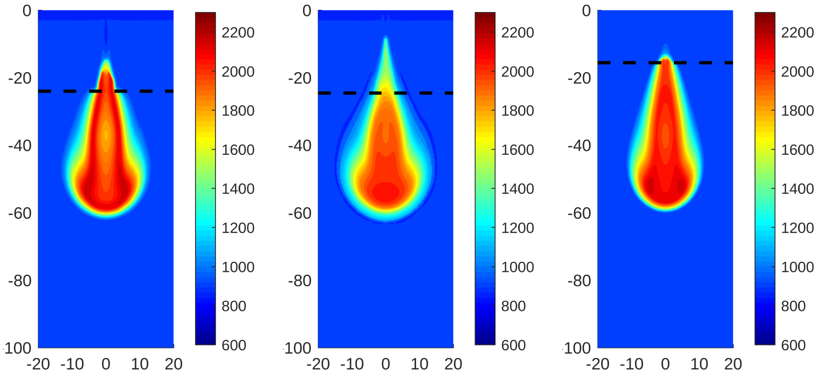

(d) SAGE (e) RIF (f) FGM

Figure 5.6: 900 K reacting test with the Cai mechanism, temperature contours, (a) (b) (c): 1.3 ms, (d) (e) (f): 1.8 ms. The dotted black line represents the calculated LOL.

In order to investigate the accuracy of FGM model reaction zone simulation results, all three models' temperature contour at "Spray A" baseline conditions are plotted against experimental chemiluminescence imaging results. It can also be seen from Figure 5.7 that the FGM model is able to qualitatively match the experimental images with a good prediction of the reaction zone. From the temperature contours shown in Figure 5.6 (where the dotted black line represents the calculated LOL) and Figure 5.7, clear flame recession can be seen in all three models with the SAGE and FGM models predicting further recession back to the nozzle at ASoR 344 μs. To further illustrate the second stage ignition initiated by combustion recession, the variation of OH mass fraction along the spray centre line is shown in Figure 5.8

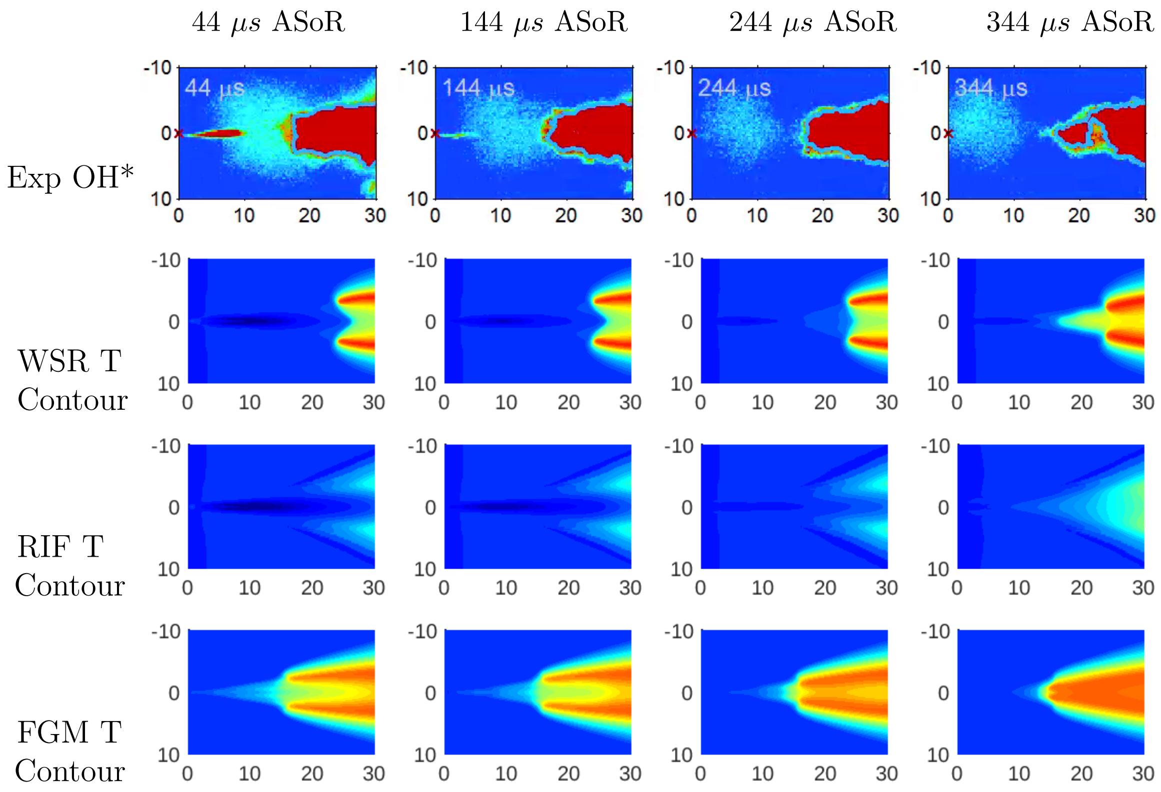

Figure 5.7: 900 K reacting test with the Cai mechanism, simulation temperature contours compared with experimental chemiluminescence OH* imaging After Start of Ramp Down (ASoR)

(where again the dotted black line represent the calculated LOL). The increase in OH mass fraction near the nozzle for all models clearly shows that the mixture has reached second-stage ignition, which corresponds to a combustion recession. The distinct spikes in OH mass fraction shown in both RIF and FGM models can be seen as separate autoignition pockets upstream of the LOL, which is consistent with the experimental study conducted by Knox *et al.* [64]. Although all three models were able to capture combustion recession, RIF was found to have a better prediction upstream of the LOL. However, when compared to time sequence experimental data for combustion recession, both the SAGE and FGM models were found to be more accurate in terms of predicting the presence of combustion recession in time, whereas the RIF model showed a slight delay. By accounting for turbulent chemistry interactions, the FGM model was able to capture combustion recession with separate autoignition events visible in the axial OH mass fraction distributions which are not captured by the SAGE model. Based on these results, it can be concluded that the current FGM model is able to predict satisfactorily the likelihood of combustion recession under baseline “Spray A” conditions.

In order to further study the ability of the FGM model to predict combustion recession, the model was investigated under the full range of reacting conditions listed in Table 4.2. Since previous studies have shown the choice of chemical mechanism to have a strong impact on the results of both FGM combustion simulations and predictions of combustion recession, both the Cai and the Yao chemical mechanisms were included in the study. Figure 5.9 shows the IDT and LOL for both chemical mechanisms under three different ambient temperatures.

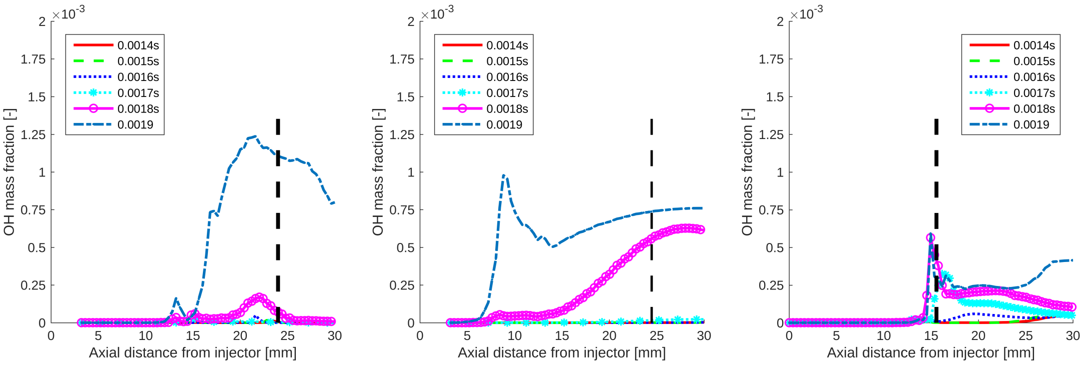

(a) SAGE (b) RIF (c) FGM

Figure 5.8: Axial OH distribution for all combustion models at 900 K reacting conditions with the Cai Mechanism (a) SAGE (a) RIF (c) FGM. Dotted line represents the calculated flame LOL

It can be seen that the FGM model was able to provide acceptable predictions with both chemical mechanisms at the higher ambient temperatures, with the Cai mechanism giving more accurate results in terms of the LOL. The IDT follows the same trend as other studies where higher ambient temperature can result in shorter IDT. It is worth noting that, although Yao mechanism, is more reactive and is tuned for spray A conditions, previous studies have also shown later IDT of Yao compared to Cai. The IDT inaccuracy occurred can be explained by the

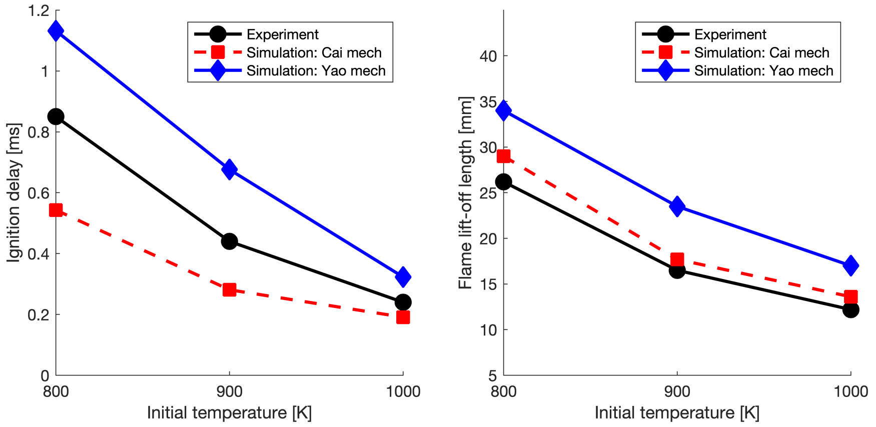

(a) Ignition Delay Time (b) Lift-Off Length

Figure 5.9: IDT and LOL for Cai and Yao mechanisms under different initial temperatures

definition of progress variable as the relative weighting will be different between each mechanism. Figure 5.10 and Figure 5.12 show temperature contours for both the Cai and the Yao mechanisms at 900 K and 1000 K. Additionally, OH mass fraction along the spray centre line is shown in Figure 5.11 and Figure 5.13. Although previous studies have shown that neither the SAGE model nor the RIF model was able to capture the combustion recession using the Yao mechanism, the FGM model was able to successfully capture the combustion recession. Both the temperature contours and OH centre line plot clearly show indications of combustion recession for both chemical mechanisms. This result is in agreement with RANS-CMC studies conducted by Blomberg *et al.* [19] showing that the Yao mechanism is also capable of predicting EOI transient effects. Furthermore, at 800 K, both Cai and Yao simulations did not pick up the combustion recession, which is also consistent with both experimental [64] and numerical studies [54] in the literature. There are, of course, differences between the results from the two mechanisms. For the current FGM model implementation, the combustion recession seen from Yao mechanism travels much further towards the tip of the injector nozzle. Interestingly, for both mechanisms under 1000 K conditions, greater fluctuations of OH mass fraction are visualised upstream of the flame LOL which can be identified as indications of distinct autoignition events directly correlated to combustion recession. However, differences between the Cai and Yao mechanisms can still be visualised in OH mass fraction distributions, as Yao's mechanism displays much lower OH mass fraction indicating that it is too weak to promote second stage ignition–which suppresses combustion recession. This finding is consistent with earlier studies using SAGE and RIF combustion models [55]. These results then suggest that although the current implementation of FGM is able to capture the likelihood of combustion recession for both chemical mechanisms, low temperature chemistry still strongly affects the local mixing and chemical processes.

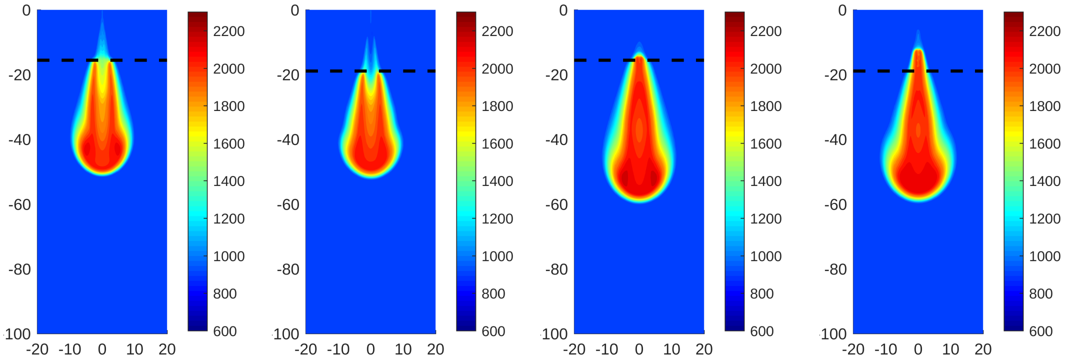

(a) FGM-Cai (b) FGM-Yao (c) FGM-Cai (d) FGM-Yao

Figure 5.10: 900K temperature slices for both mechanisms, (a) (b):1.3ms, (c) (d):1.8ms. Dotted black line represents the calculated LOL.

5.3 Summary

The primary goal of this study was to investigate whether the end-of-injection transient phenomenon, combustion recession, could be captured using a tabulated chemistry combustion model with a flamelet generated manifold. Simulations were performed with widely-used Eulerian-Lagrangian spray models within a RANS framework. A range of low-temperature diesel combustion conditions corresponding to the "Spray A" experiments was tested.

Non-reacting evaporating spray characteristics were validated against experimental

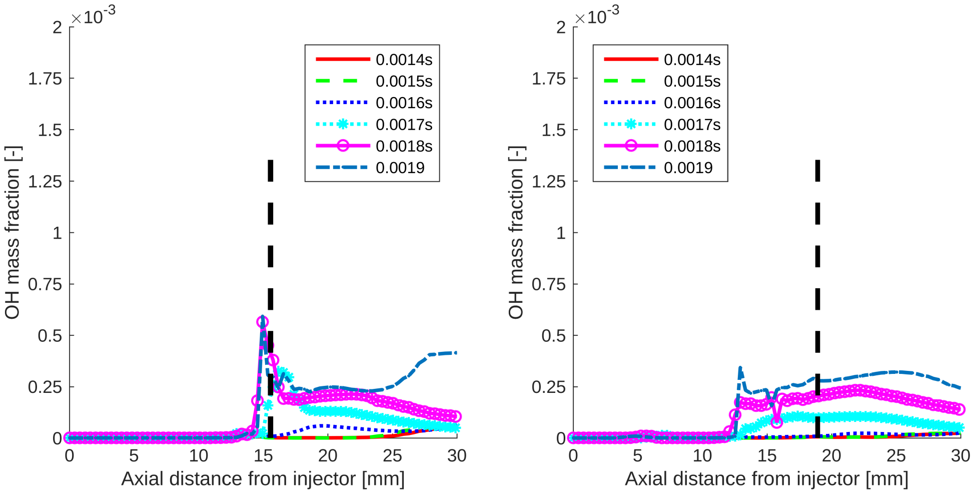

(a) FGM-Cai (b) FGM-Yao

Figure 5.11: Axial OH distribution for both chemical mechanisms at 900 K conditions. Dotted black line represents the calculated LOL.

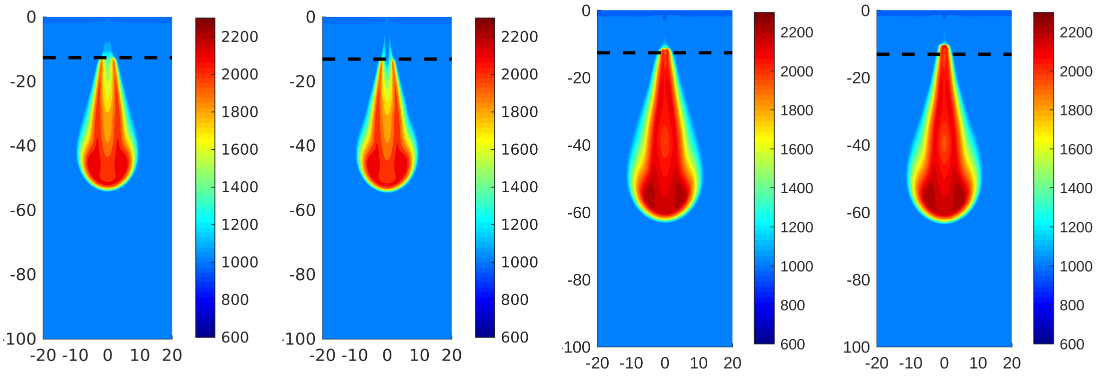

(a) FGM-Cai (b) FGM-Yao (c) FGM-Cai (d) FGM-Yao

Figure 5.12: 1000 K temperature slices for both mechanisms (a) (b):1.3ms, (c) (d):1.8ms. Dotted black line represents the calculated LOL.

results from the ECN database with the chosen spray sub-models showing good agreement for global parameters such as liquid and vapour penetration and also local parameters of radial mixture fraction distribution. Reactive simulations were then carried out for "Spray A" baseline conditions using the FGM model and also two combustion models available in CONVERGE, the well-stirred reactor SAGE model and the RIF model, for comparison. It was found that SAGE and RIF

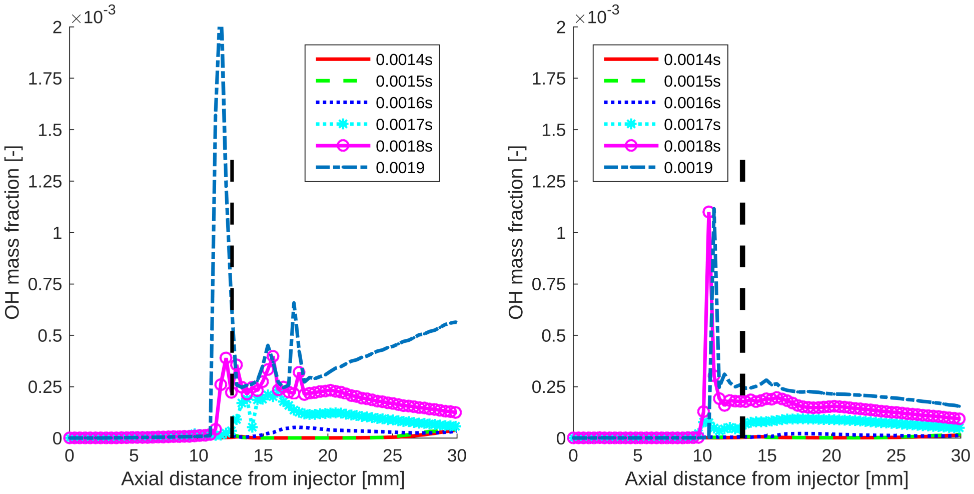

(a) FGM-Cai (b) FGM-Yao

Figure 5.13: Axial OH distribution for both chemical mechanisms at 1000 K conditions. Dotted black line represents the calculated LOL.

models both overpredicted the ignition delay time and flame lift-off length. The FGM model underpredicted the ignition delay time but gave the best prediction for flame lift-off length. Combustion recession was predicted by all three models with the RIF and FGM models being able to better capture individual pockets of OH inline with experimental observations.

The FGM model performance was further examined using two different chemical kinetics mechanisms for n-dodecane, the Cai mechanism [20] with 57 species and 197 reactions and the Yao mechanism [166] with 54 species and 268 reactions, over different ambient temperature conditions. For low temperature conditions, 800 K, the Yao mechanism overpredicted both IDT and LOL whereas the Cai mechanism predicted autoignition but underpredicted the IDT while closely matching the flame LOL. Combustion recession was not captured according to the Cai mechanism at 800 K, which is consistent with the previous modelling works using both the SAGE and RIF models as well as the available experimental data.

Both mechanisms captured the IDT and flame LOL with acceptable accuracy at the higher ambient temperatures of 900 K and 1000 K, with the Cai mechanism slightly underpredicting the IDT and the Yao mechanism slightly overpredicting the IDT. These minor differences can be explained by the differences in species manifolds for these two chemical mechanisms. In terms of combustion recession, both mechanisms were able to capture the second stage ignition required for this transient phenomenon in the FGM model, whereas the SAGE and RIF models were not able to capture second stage ignition using the Yao mechanism. The Yao mechanism was able to predict combustion recession further upstream towards the near nozzle region. Both mechanisms show clear signs of separated ignition pockets through OH mass fraction plots along the spray centre line. In general, the study shows that the tabulated chemistry FGM model is able to capture similar trends of combustion recession to those shown in the experimental data available in the literature. The results of this work also indicate that low temperature reaction mechanisms play a significant role in predicting the likelihood of second-stage ignition and combustion recession events near the injector nozzle region.

Finally, even though the current FGM model was able to predict combustion recession, this work illustrates the difficulties of using a simplified kinetic rate model—as shown by the models' relatively poor prediction of ignition delay time and its inability to fully capture the sequence of ignition events propagating towards the near nozzle region as shown in the experimental observations of combustion recession. Therefore it is worth tabulating the mean reaction source term, thereby overcoming the limitations of the kinetic rate model. Additional chemical mechanisms studies are also worth investigating using FGM methods.

The greatest obstacle to discovery is not ignorance –
it is the illusion of knowledge.

—General George S. Patton

6

A Study on Kinetic Mechanisms of Diesel Fuel Surrogate n-Dodecane for the Simulation of Combustion Recession

Contents

The content in this chapter is a result of the collaborative efforts of the author, Dr Riyaz Ismail. The author is responsible for all studies presented. The content in this chapter has been published in [34].

6.1 Overview

Chapter 5 explored the capability of a Flamelet Generated Manifold (FGM) model in predicting combustion recession, where different ambient temperature conditions and two chemical mechanisms (Yao and Cai) were studied. The results favoured the newly implemented FGM over the RIF model and the WSR model in terms of the predictions of flame lift-off length and its capability to predict combustion recession using two different chemical mechanisms. Although these studies have come to the same conclusions concerning the influence of ambient thermodynamic conditions on the prediction of combustion recession, discrepancies were found in the capabilities of different chemical kinetic models. Therefore, this study aims to elucidate further the effects of different chemical mechanisms for n-dodecane – including the reduced chemical mechanism from Ranzi *et al.* [116] (130 species and 2395 reactions referred to as to the Polimi mechanism) – in the prediction of combustion recession.

In the following chapter, standard “Spray A” conditions from ECN will be investigated under a RANS framework. Firstly, the non-reactive liquid and vapour penetration, as well as mixing properties, will be analyzed. Four different chemical mechanisms for n-dodecane that are commonly used in the engine simulation communities will be employed to study the influence of chemical mechanisms on combustion recession. These chemical mechanisms will be investigated using a 1D flame solver first to understand their characteristics, peculiarities and reliabilities under diesel engine conditions. Multidimensional reactive spray simulations will then be performed using both an FGM model based on the homogeneous reactor tabulation method and a newly implemented FGM model based on the igniting counterflow diffusion flame tabulation method using the CONVERGE CFD solver. A description of the computed flamelet database will be included together with an analysis comparing the results of the simulations to experimental data from the literature. The effect of the tabulation method on reactive spray prediction will be detailed. Finally, the efficacy in predicting combustion recession by each chemical mechanism under an FGM framework will be discussed.

6.2 Methods

6.2.1 Spray Modelling

Detailed model constants and boundary conditions set up for non-reacting spray can be found in Chapter 4. A brief non-reacting spray simulation description will be included here. A conventional “Blob”injection model is employed to simulate the spray injection process where“parcels” are injected into the computational domain with the same characteristic size as the nozzle diameter. Droplet break-up and atomization are modelled using the Kelvin-Helmholtz Rayleigh-Taylor (KH-RT) model. The inherent grid sensitivity of the KH-RT model has been studied previously for the non-reacting “Spray A” conditions and validated against another commercial CFD solver [91]. Droplet collision is described using the No Time Counter (NTC) model, and the droplet drag is accounted for using the dynamic drag model. The evaporation process is modelled using the Frossling correlation. The effects of turbulence on droplets are characterized using the stochastic dispersion model, where turbulence is modelled using the standard $k - \epsilon$ model with modified constants.

6.2.2 Combustion Modelling

Two different Flamelet Generated Manifold (FGM) model-based approaches are used for spray combustion simulations. As described previously, the attractiveness of FGM models is their ability to incorporate detailed chemistry with a reduced computational cost. Two types of representative flamelets for non-premixed combustion are compared to study the influence of chemical mechanisms in predicting combustion recession. The first flamelet type is based on 0D ignition flamelets, where the flamelet manifold is obtained by solving an experimental homogeneous reactor (HR). A homogeneous reactor is a simplified zero-dimensional configuration in which the mixture is considered stagnant and perfectly mixed. The governing equations for the HR flamelet can be derived through eliminating the variables associated with the x-coordinate, K, and a from equations (5.6 - 5.8). The HR flamelet solution is calculated through the CONVERGE CFD 0D solver with a tabulation against mixture fraction, Z, and a reaction progress variable, c. In this study, the definition of Z follows the well known Bilger correlation [10]. The reaction progress is a monotonic variable that captures each stage of combustion evolution, which is defined as a linear combination of three key species (CH_2O, CO and CO_2) normalized by their equilibrium value. The inclusion of CH_2O is inspired by the notion that it is significant at the start of the ignition process, whereas CO represents the intermediate stage of combustion and subsequently CO_2 represents the end of the combustion process. It is to be noted here that the definition of progress variable will not affect results as long as the chemistry parametrization (selection of species) represents each stage of chemical evolution and is monotonic. The monotonicity of the progress variable is ensured during the parametrization process leading to a consistent FGM. A detailed description for the implementation can be found in [128].

The second type of flamelet studied herein is the 1D non-premixed laminar counterflow diffusion flame (CDF) where solutions are computed in physical space and time using the CHEM1D code [22]. The detailed generation process of this flamelet has been detailed in Chapter 5. The CDF tabulation method makes fundamentally different assumptions compared to the HR tabulation method, whereby diffusion and transport processes are considered to have a minor role during ignition. For a stationary CDF, the manifold is generated using a sequence of steady flames solutions with strain rates varying from the lowest value to the quenching value. However, as spray simulations are unsteady and initially non-reacting, time-dependent flamelets are solved from a mixed but non-reacting initial state in order to capture transient events in diesel sprays. The ignition behaviour is followed in time until a steady-state flame is reached. Previous studies have shown that generating unsteady flamelets using quenching flamelets does not lead to ignition of diesel sprays. Therefore, for this study, the FGM is constructed using the igniting counterflow diffusion flame (ICDF) flamelet solution.

Coupling of the FGM database with the CONVERGE flow solver is achieved via a representative set of species mass fractions and the chemical source term of the reaction progress variable, c. For this study, 15 representative species are considered for each respective chemical mechanism. The retrieval of the chemical properties from the FGM is achieved via linear interpolation. A schematic of FGM and turbulent flow field coupling can be found in Figure 6.1.

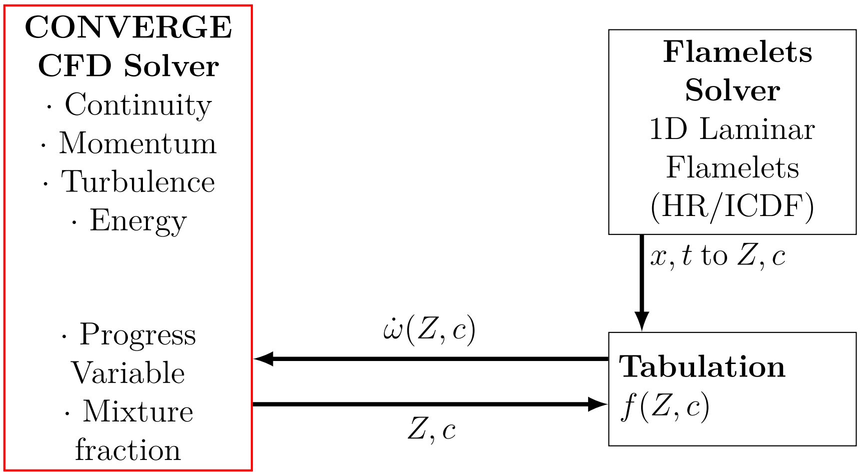

Figure 6.1: FGM combustion model coupling with CONVERGE CFD solver

6.3 Case Setup

6.3.1 ECN "Spray A"

Simulations are performed for the ECN "Spray A" , and the results are validated against the ECN's high-quality and high-fidelity data-sets. Both non-reacting and reacting conditions for "Spray A" tested in this study are listed Table 4.4. All simulations are conducted using the commercially-available CFD solver, CONVERGE. All non-reacting parameters are set to be the same as the previous chapter.

6.3.2 Flamelet Solutions Study

This section presents a comparative study of the combustion mechanisms' behaviour in 1D, i.e. the fundamental behaviour of the mechanisms removed from the spray environment (essentially considering the top right-hand box in Figure 6.1 in isolation). Note that all flamelet solutions within this section are computed using the one-dimensional flame code - CHEM1D and that only flamelet solutions generated from the ICDF approach are investigated.

The four different chemical mechanisms for n-dodecane that are investigated are listed in Table 6.1. All mechanisms are derived from detailed mechanisms with thousands of species and reactions. The differences between each mechanism come from its initial mechanism and reduction methodology. All these mechanisms have been validated and developed with accuracy targeting engine-related conditions. It is worth noting that the Yao mechanism, though very compact, is specifically tuned for “Spray A” conditions [166].

Table 6.1: Baseline combustion model comparison

Mechanism	Number of species	Number of reactions	Original mechanism
Cai *et al.* [20]	57	197	[160]
Yao *et al.* [166]	54	268	[169]
Luo *et al.* [76]	105	420	[160]
Ranzi *et al.* [116]	130	2395	[116]

Figure 6.2 shows the maximum temperature evolution of the unsteady flamelet solutions under the reacting “Spray A” baseline conditions for all four chemical mechanisms. All chemical mechanisms are able to capture different stages of combustion. Stage 1 of combustion initiated by the premixed spray region low temperature heat release is well represented by the Cai, Luo and Polimi mechanisms at around 0.3 ms ASOI, whereas the Yao mechanism predicts early first stage combustion. Stage 2 of combustion is seen as a steep temperature rise after stage 1. Stage 2 is observed at around 0.4 ms ASOI for both the Cai and Polimi mechanisms, whereas the Luo mechanism prolonged the respective time to about 0.5 ms ASOI. The Yao mechanism is seen to give earlier second stage combustion at around 0.25 ms ASOI. A more quantitative study of ignition delay time (IDT) using the definition from the ECN is shown in Table 6.2. According to the recommended ECN guidelines, the ignition delay time is calculated as follows:

$$\tau_{IDT} = \tau(max(\frac{dT_{max}}{dt})) - \tau_{SOI} \tag{6.1}$$

Table 6.2: Ignition delay time from the unsteady flamelet calculations

Mechanisms	Cai	Yao	Luo	Polimi	Experiment
IDT (ms)	0.394	0.285	0.599	0.323	0.40-0.45

The early ignition prediction by the Yao mechanism has been attributed to an increased accumulation of HO_2 — a key species in tracking first stage ignition. Reactions producing HCO are enhanced, thereby leading to increased HO_2 and predictions of reduced ignition [25]. Additionally, reactions relevant to the production of H_2O_2 are greatly enhanced in the Yao mechanism compared to the other mechanisms leading to earlier predictions of the high-temperature ignition stage. The differences between the chemical mechanisms are further studied through the chemical source term of the progress variable $\dot{\omega}_c$ for each mechanism. The source term of the progress variable has a significant effect on the predictions of combustion and ignition delay time. All chemical mechanisms generate three well-defined reaction zones representing the different stages of combustion with lower regions depicting the early ignition stage species (CH_2O), intermediate regions representing an intermediate stage of combustion species (CO) and top regions representing the end of combustion species (CO_2). Figure 6.3 gives significant prior insight into the expected behaviour of each mechanism before embarking on the detailed 3-D RANS simulations of the reacting spray. As expected from the temperature evolution and ignition delay study, the Yao mechanism clearly shows much higher values of the chemical source term in low progress variable regions, representing the ignition stage of combustion, than the other mechanisms. The Luo mechanism shows a relatively lower source term values in regions associated with ignition and the intermediate stages of combustion stages which corresponds to the prolonged temperature rise in flamelet solutions. The Polimi mechanism and the Cai mechanism present similar magnitudes in all three regions with the Cai mechanism having higher source term values in the intermediate region and the Polimi mechanism having higher source term values in the ignition region.

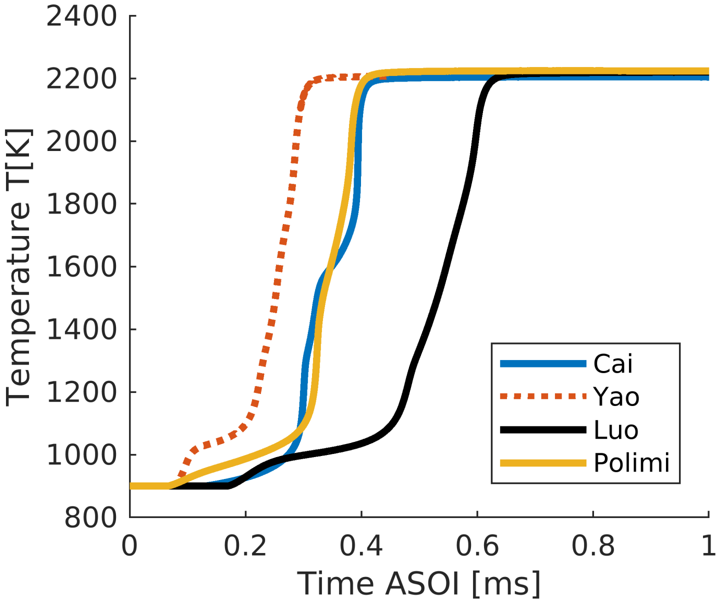

Figure 6.2: Maximum temperature evolution for 1D Igniting Counterflow Diffusion (ICDF) flame simulations at the reacting "Spray A" baseline conditions for all mechanisms: T$_{ambient}$ = 900 K, 15%O_2.

6.4 Results and Discussions - 3D Spray Simulations

Following the same validation procedures as previous chapters, the non-reacting evaporating "Spray A" condition was first validated against the ECN experimental data for liquid and vapour penetration. Details of the grid dependency and physical sub-model testing can be found in Chapter 4. Reacting spray simulations were performed under the conditions outlined in Table 4.4. Two canonical combustion configurations representing the spray flame chemical processes were used: homogeneous reactor (HR) and igniting counterflow diffusion flame (ICDF). Firstly, the predictions from an HR based FGM (referred to as the 0D FGM) model are compared with those of an ICDF based FGM (referred to as the 1D FGM) model to show the relative performances of the two FGM methods based on a comparison of ignition delay time, lift-off length and EOI combustion recession. This comparative study is followed by an investigation into the performance of the different chemical mechanisms using the best performing FGM model.

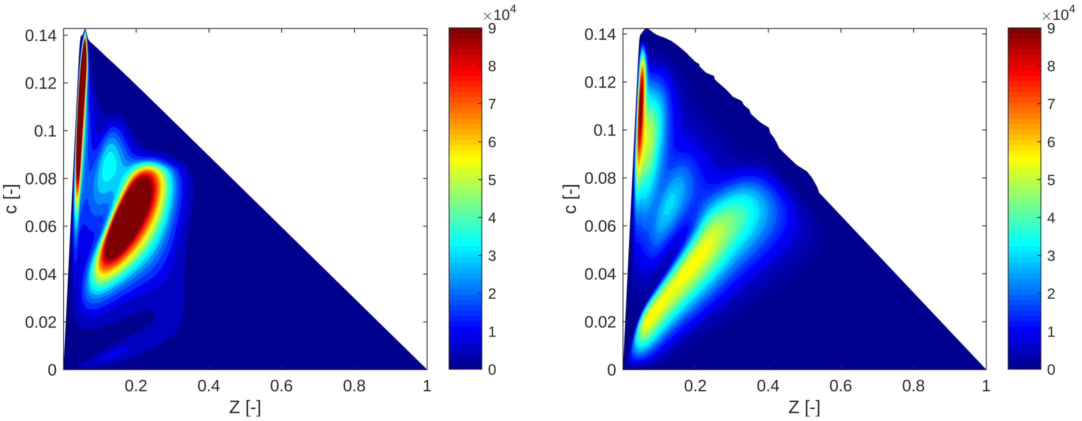

(a) Cai (b) Yao

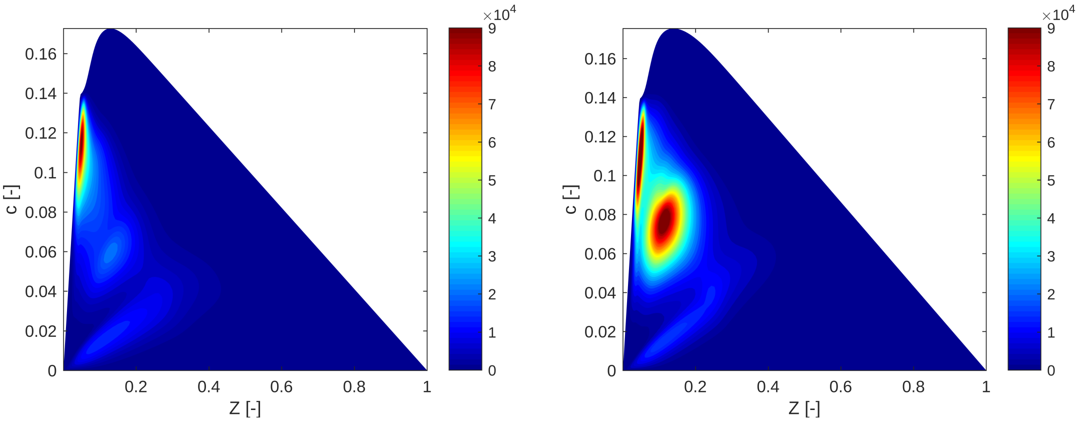

(c) Luo (d) Polimi

Figure 6.3: 900 K reacting case chemical source term (ω) of the progress variable with different mechanisms.

Comparing 0D FGM and 1D FGM Simulations

As previously discussed, the generation of the 0D FGM manifold is achieved by using a homogeneous reactor assumption solved within the CONVERGE software. Figure 6.4 shows the maximum temperature evolution of both 0D and 1D FGM simulations under the "Spray A" conditions for the Cai mechanism. As seen from the figure, the two stages of combustion were captured by both approaches. However, the 0D FGM model predicts ignition much earlier than 1D FGM case and remains at a much higher temperature at all times throughout the simulation. The predicted ignition delay is then shorter for the 0D FGM than for the 1D FGM case. The findings obtained in this study are then very similar to the study that was performed by Eguz *et al.* [32]

where the HR FGM is found to give shorter ignition delay times for ECN “Spray H ”.

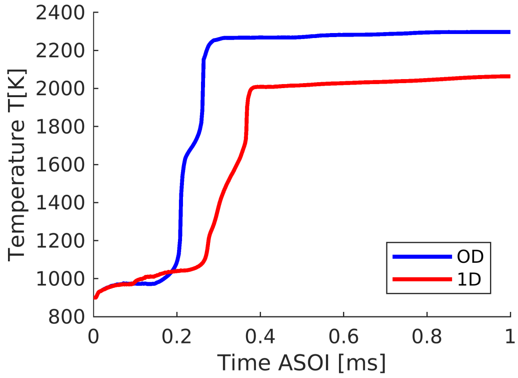

Figure 6.4: “Spray A ” baseline conditions time evolution of maximum temperature with HR based 0D FGM and ICDF based 1D FGM for the Cai chemical mechanism

In order to study further the differences between two FGM approaches, the flame lift-off length and combustion recession characteristics are investigated. The definition of LOL used in this work is consistent with the ECN standard for simulations and is thus defined as the distance from the injector to the first location where the Favre-averaged OH mass fraction reaches 14% of the instantaneous maximum during the steady state period. Figure 6.5 shows the temperature contours of both FGM approaches at two different timesteps. It is clear that the LOL for the 0D FGM case (LOL=12.84 mm) is much shorter than that predicted by the 1D FGM case (LOL=19.34 mm), which follows the same trend of IDT observations discussed earlier. A similar trend was also found by Eguz *et al.* [31] while studying tabulation methods for “Spray A” where LOL is found to have an almost linear correlation with the IDT. The reasons for this can be explained by the higher production of the progress variable in the near nozzle region caused by early ignition in the 0D FGM.

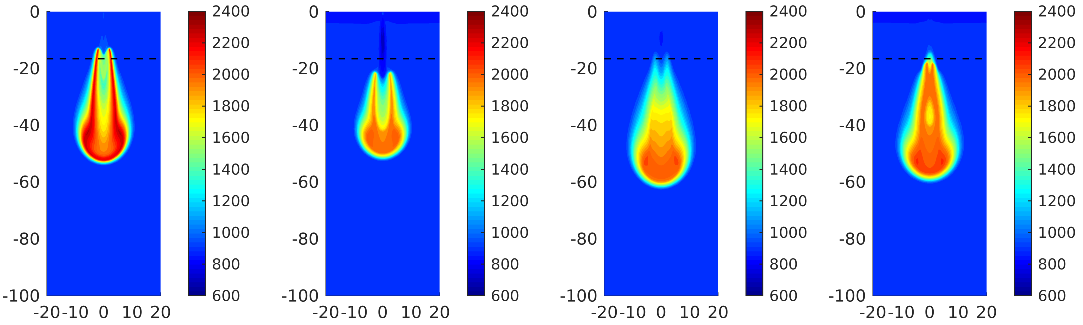

(a) 0D (b) 1D (c) 0D (d) 1D

Figure 6.5: “Spray A” baseline conditions with the Cai mechanism with temperature distribution. (a) (b) 1.3 ms (c)(d) 1.8 ms. Black line: measured mean lift-off length (16.5 mm) from ECN database

More importantly and to the great interest of this present study, combustion recession was not captured by the 0D FGM whereas clear flame retraction after the end of injection is observed in the 1D FGM results as shown in Figure 6.5. This can be explained by the HR tabulation method’s exclusion of diffusion and transport phenomenon. Owing to this fundamental difference between the HR and ICDF tabulation methods, the HR tabulation is found to have higher source term values across all regions of progress variable and mixture fraction space [94]. Therefore, higher temperatures and less radially extended flame regions are found in 0D FGM results, which align with the discussions earlier in terms of shorter IDT and LOL. Combustion recession was not captured by 0D FGM despite the higher chemical source term presented in the HR tabulation. This is likely to be due to the nature of the HR tabulation, where the influence of strain effects on diffusion flames is not included. In addition with a narrower reaction zone, a higher axial velocity is found upstream of the LOL which reduces the residence time for fuel mixtures that otherwise could reach second stage ignition and hence promote combustion recession [54]. Based on the findings presented in this section, while the HR based FGM approach is capable of capturing both IDT and LOL with good accuracy, the ICDF based FGM is necessary to capture the end of injection processes due to its better representation of strain effects and transport phenomenon in diffusion flames. Therefore, the following studies on the effect of chemical mechanisms in predicting combustion recession will be constructed using the 1D FGM approach.

Effect of Chemical Mechanisms on 1D FGM RANS Simulations of ECN "Spray A"

The differences in chemical mechanisms are first visualized through the maximum temperature evolution from 1D FGM simulations shown in Figure 6.6. As expected, the trend of the temperature evolution follows the same result as the 1D flamelet solutions where the Yao mechanism reaches both stages of combustion earliest, and the Luo mechanism shows retarded combustion. The maximum temperature for all mechanisms is brought down to around 2000K, which is consistent with other flamelet based model simulations [70]. The lower temperature compared to the 1D simulation can be seen as a result of a RANS averaging calculation in terms of mixture fraction and progress variable, which results in a lower source term value during the look-up process. Previous studies have also shown lower temperature contours from a RANS turbulence treatment compared to LES [99].

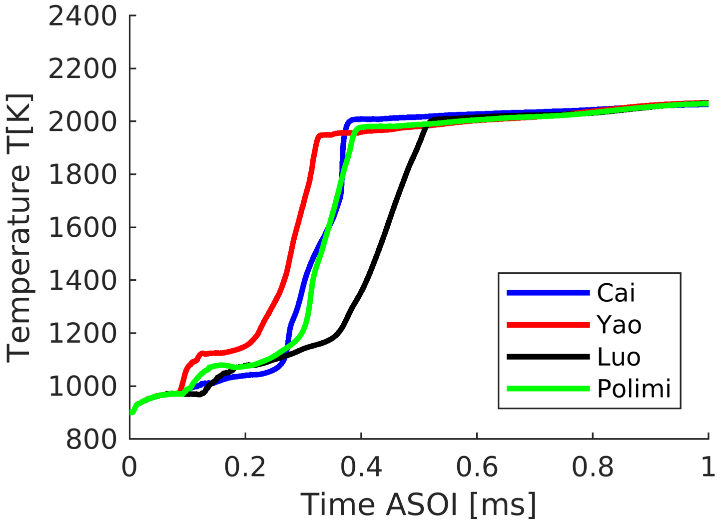

Figure 6.6: "Spray A" baseline conditions time evolution of maximum temperature from 1D FGM using different chemical mechanisms

A more quantitative comparison of IDT and LOL using the definitions outlined previously are shown in Table 6.3. The Yao mechanism predicted a shorter ignition delay time which is consistent with other studies, with the reason for this underprediction stemming from the higher reactiveness of the Yao mechanism in the manifold's ignition region. The Polimi mechanism IDT prediction, although shorter compared to experimental data, is consistent with the LES study performed by Wehrfirtz *et al.* [159]. Similar results for the Luo and Cai mechanism IDT predictions can also be found in previous studies [116] [59]. The IDT results from RANS simulations also indicate that IDT predictions are mainly driven by the ignition behaviour of chemical mechanisms since the 3D simulations have a limited effect on the predictions of IDT. The clear resemblance of IDT predictions between the RANS study and the flamelet solutions study shows the dominant role of the chemical mechanism in spray autoignition predictions. In terms of LOL, both Cai and Yao mechanisms are able to predict these combustion indicators, whereas the Luo and Polimi mechanisms showed a longer LOL. This finding is consistent with earlier flamelet solutions where LOL showed a linear correlation with IDT. It is also worth noting that the experimental LOL in the ECN database is defined using a threshold of 50 % of chemiluminescence levelling-off value, while numerically there are different ways to quantify LOL. Therefore, the quantitative assessment in this study will serve as the guidance for physical trends. Overall, all chemical mechanisms were able to predict both quantities at values close to the experimental data under a RANS FGM framework.

Table 6.3: "Spray A" baseline conditions ignition delay time and flame lift-off length from 1D FGM simulations compared to ECN Sandia experimental measurements.

Mechanism	Cai	Yao	Luo	Polimi	Experiment
IDT (ms)	0.3667	0.315	0.47	0.381	0.40-0.45
LOL (mm)	19.34	17.1	26.78	22.04	15.80-17.90

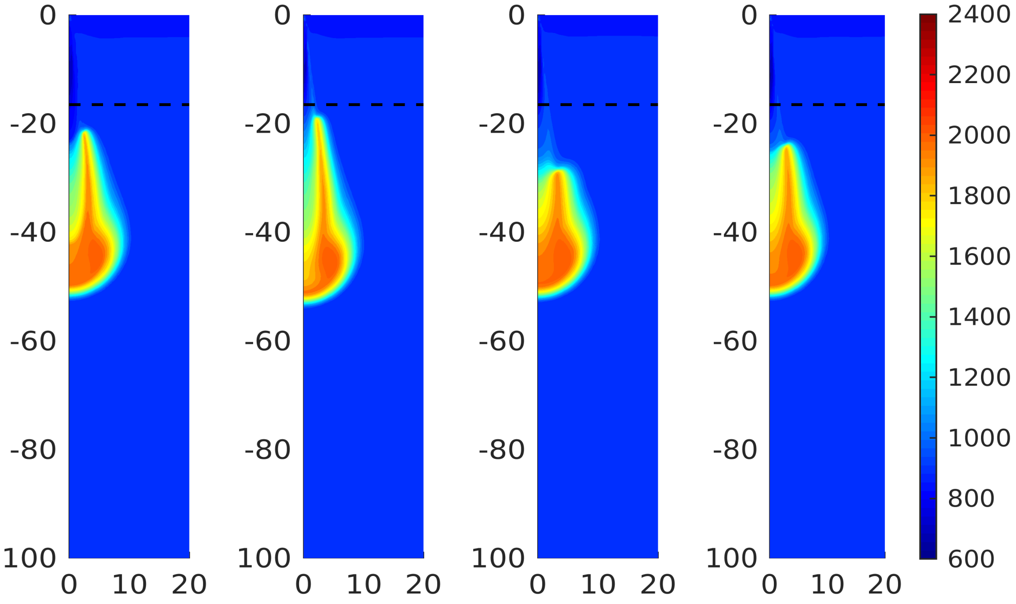

(a) Cai

(b) Yao

(c) Luo

(d) Polimi

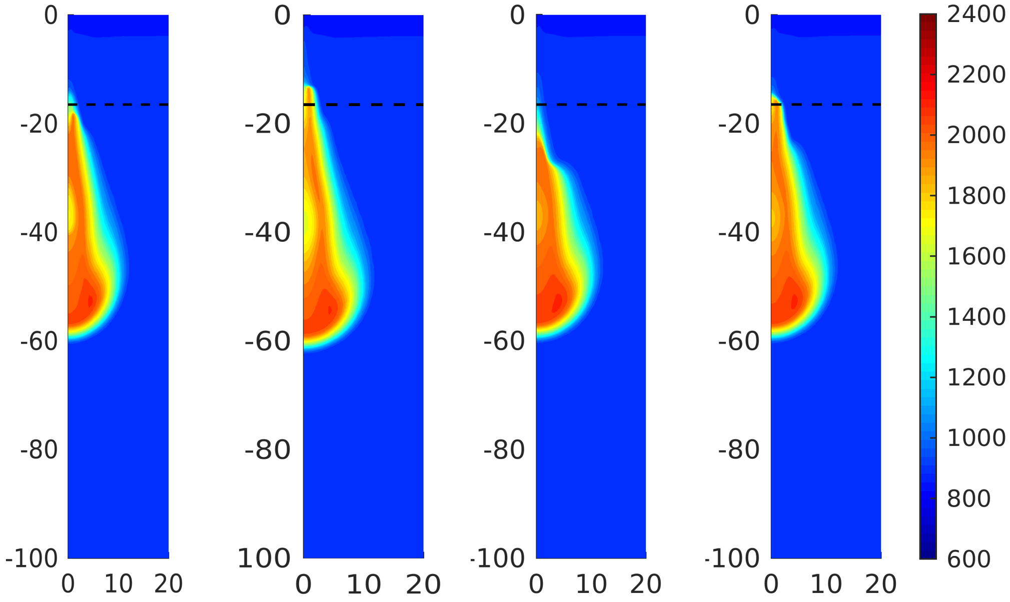

(e) Cai

(f) Yao

(g) Luo

(h) Polimi

Figure 6.7: "Spray A" baseline conditions temperature distributions for all mechanisms. (a) (b) (c) (d): 1.3 ms ASOI (e) (f) (g) (h): 1.8 ms ASOI. Black line: mean measured lift-off length (16.5 mm) from ECN database

In order to help visualize the performance of the different chemical mechanisms in predicting LOL, reactive spray penetration and combustion recession, Figure 6.7 shows the simulated temperature contour from 1D FGM for all mechanisms under "Spray A" baseline conditions. At quasi-steady-state (1.3 ms), some differences are observed in the temperature profiles; however, the overall flame structure is not significantly influenced by the applied chemical mechanisms. The lack of available experimental data also made it difficult to compare the recession distance quantitatively. For the 1D FGM approach, lift-off length is located where the large strain rates and higher scalar dissipation rate exceed the flame extinction limit. Therefore, it is highly dependent on the sensitivity of chemical mechanisms in terms of strain rate as well as the local thermodynamics conditions. Only small differences were noticed under "Spray A" baseline conditions with the Luo mechanism giving a higher LOL and slightly varied flame structure. This is due to weaker low-temperature reactivity which is consistent with the previous manifold study. It is also worth noting that although originating from the same mechanism, the Luo mechanism and the Cai mechanism exhibit different behaviour in terms of flame predictions which again shows the importance of including low temperature chemistry under "Spray A" baseline conditions. Figure 6.7 also shows the end of injection (1.8 ms ASOI) transient predictions using all four chemical mechanisms. Combustion recession is clearly captured by all mechanisms with all flames retracting back to the nozzle tip passing through the LOL. Further analysis is shown in Figure 6.8 with the OH mass fraction plotted along the injector axis. It can be seen the increase in OH mass fraction near the nozzle for all chemical mechanisms clearly show that the mixture has reached second-stage ignition indicating combustion recession. The distinct spikes in OH mass fraction shown for all chemical mechanism, but especially the Cai and the Yao mechanisms, can be seen as separate autoignition pockets upstream of the LOL, which is consistent with the experimental study conducted by Knox *et al.* [64]. Additionally, it can be seen from mixture fraction-temperature space in Figure 6.9 that the low temperature combustion tracer CH_2O is active for all mechanisms indicative that low temperature reactions are occurring towards the end of injection which will eventually lead to combustion recession. As seen earlier with the axial OH distribution, the Cai mechanism has a much higher concentration of CH_2O and at much higher temperatures which is consistent with the strong prediction of combustion recession. It can also be seen from Figure 6.9 that the Yao and Polimi mechanisms have a broader distribution of CH_2O over a range of mixture fractions leading to less pronounced peaks of OH compared to the Cai mechanism. More interestingly, the predictions of combustion recession align well with the flamelet solutions where the Cai mechanism showed much higher OH concentrations when autoignition is established, corresponding to higher chemical source term at intermediate stage combustion. The Yao mechanism retracts further up to the nozzle tip, which shows stronger ignition behaviour corresponding to a higher source term in igniting regions. The Polimi mechanism showed similar predictions to the Cai mechanism in terms of flame retraction; however, the OH concentration is much lower compared to the Cai mechanism. The Luo mechanism again shows lower OH concentration as well as a shorter combustion recession. This further indicates that for the RANS 1D FGM approach, low temperature chemistry behaviour plays a significant role in both steady-state flame structure and end of injection combustion recession predictions. Although capable of predicting combustion recession, the current 1D FGM implementation does not include turbulent chemistry interactions in the manifold, which could explain the flame is not travelling all the way to the nozzle tip. We note, however, that due to the limited availability of relevant experimental data, the exact flame retraction distance is not well quantified currently. However, the combustion recession predictions here closely agree with previous RANS CMC split injection studies using the Yao mechanism [19] and the well-stirred reactor model study using the Cai mechanism [59] under “Spray A ” conditions. Particular strength was found for this 1D FGM implementation in the capability of incorporating different chemical mechanisms and the ability to predict combustion recessions.

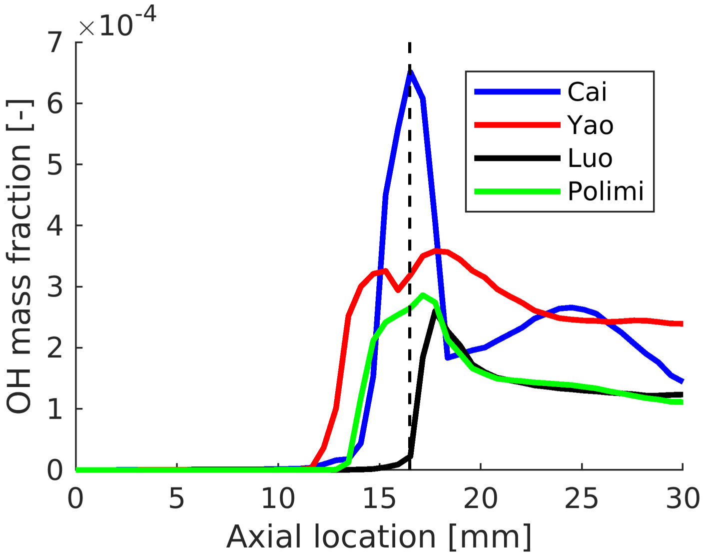

Figure 6.8: “Spray A” baseline conditions OH mass fraction comparison from 1D FGM using different chemical mechanisms at 1.8 ms ASOI. Black line: mean measured lift-off length (16.5 mm) from ECN database

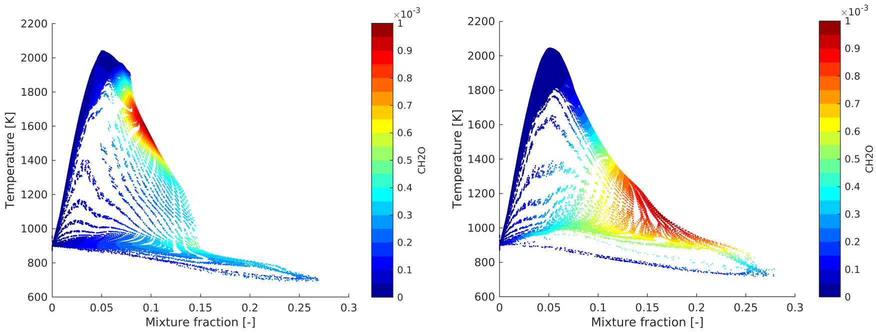

(a) Cai

(b) Yao

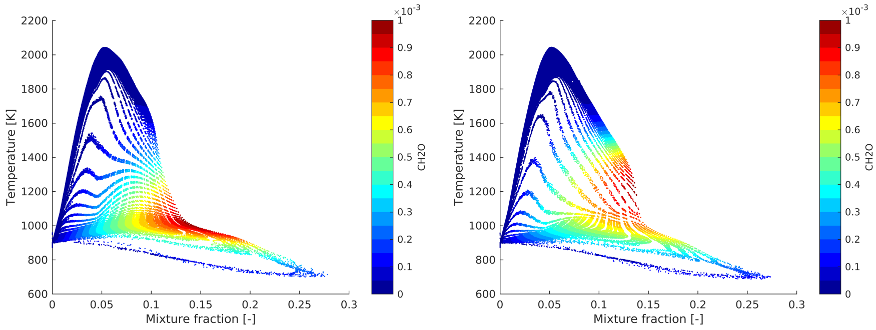

(c) Luo

(d) Polimi

Figure 6.9: “Spray A” baseline conditions scatter point presentation in ZT plane, coloured by CH_2O at t=1.3 ms.

6.5 Summary

Three-dimensional diesel “Spray A” simulations have been performed in this study under a RANS FGM framework. The objectives of this study were to: (1) compare the ability of two different tabulation methods: the 0D igniting homogeneous reactor approach and 1D igniting counterflow diffusion flame approach, under a RANS FGM framework to predict combustion recession, (2) study the effect of chemical mechanisms in predicting flame structure and combustion recession using the chosen FGM approach. All Simulations were conducted using Eulerian-Lagrangian spray models. Only the baseline conditions of low-temperature diesel combustion corresponding to the “Spray A” experiments were tested.

Non-reacting evaporating spray characteristics were validated against experimental results from the ECN database with the chosen spray sub-models showing good agreement for global parameters such as liquid and vapour penetration and also local parameters of radial mixture fraction distribution.

Reactive simulations were carried out using a newly implemented FGM model in CONVERGE with flamelet solutions generated from both CONVERGE and CHEM1D. The study of tabulation method showed that both the HR and the ICDF methods are capable of qualitatively capturing the flame structure at steady-state. However, higher source terms were found for the HR case, which leads to shorter ignition delay and LOL than the ICDF approach. Higher temperature contours were also found in the HR approach when compared to the ICDF approach owing to the exclusion of diffusion and transport phenomenon during a reaction. The lack of strain effects in diffusion flame also resulted in the failure of the HR FGM approach to predict combustion recession. This indicates the significant role that diffusion processes still play in flame predictions, and particularly on the end of injection processes such as combustion recession, even at the very high temperature and pressure conditions typical of diesel engine combustion. It was concluded, therefore, that in order to capture the end of injection transient phenomenon in diesel sprays, the ICDF tabulation approach for the FGM model is more appropriate.

Three skeletal mechanisms and one reduced chemical mechanism were tabulated using the ICDF approach and 3D reacting simulations were performed under “Spray A” baseline conditions. The diesel spray flame structures predicted by all chemical mechanisms were qualitatively similar. The differences of progress variable source term retrieved from the manifold of each mechanism resulted in slight differences of flame stabilization locations which effected the LOL predictions. The IDT analysis from the 3D simulations shows similar results to the 1D flamelet results, which indicates chemical kinetics is one of the driving factors for the predictions of IDT in the FGM approach. Both the Cai mechanism and the Polimi mechanism showed good predictability in IDT and LOL. With a higher chemical source term in the ignition region, the Yao mechanism predicted an earlier IDT and a shorter LOL. Whereas the Luo mechanism consistently overestimated the IDT and LOL due to lower chemical source term values presented in the manifold throughout all regions.

Finally, the effect of chemical mechanisms was further presented in the predictions of combustion recession. The results showed that low-temperature chemistry is a driving force for second-stage ignition in diesel spray end-of-injection processes. Clear evidence was found through the comparison of OH quantities obtained from the Cai mechanism and the Luo mechanism. Originating from the same detailed chemistry, the Cai mechanism presented a stronger prediction for combustion recession due to its better incorporation of low-temperature chemistry. In the current FGM framework, the Yao mechanism predicted the furthest combustion recession phenomenon due to its higher chemical source term in ignition regions which agrees with prior experimental observations showing that combustion recession is driven by a series of auto-ignition events.

Although this study has given increased physical insights for the prediction of combustion recession using the FGM approach, there is still room for improvement in terms of the combustion model. The next step of this study would be to include $\widetilde{Z''^2}$ through tabulation or the combustion modelling processes. As highlighted by previous studies, this could increase the diffusion processes in near nozzle regions, creating a stronger entrainment flux resulting in further combustion recession.

When I'm working on a problem, I never think about beauty. I think only how to solve the problem. But when I have finished, if the solution is not beautiful, I know it is wrong.

— R. Buckminster Fuller

7

Simulation of ECN Diesel "Spray A" Using RANS and LES Conditional Source-term Estimation

Contents

The content in this chapter is a result of the collaborative efforts of the author and Dr Riyaz Ismail. The author is responsible for the underlying development of the CSE code and implementation of the combustion model to the CFD solver. Dr Riyaz Ismail is responsible for the chemistry reduction and tabulation techniques using the flamelet generated manifolds. Figure 7.21, Figure 7.28,

Figure 7.29, Figure 7.30 and Figure 7.32 are shared between the author and Dr Riyaz Ismail. However, the analysis on the results is the author's independent work. The content in this chapter has been submitted to Combustion Theory and Modelling and Proceedings of Combustion Institute.

7.1 Overview

First proposed by Bushe and Steiner [18], Conditional Source-term Estimation (CSE) is a combustion model which invokes the CMC hypothesis. A more detailed model description will be included in Section 7.2. Previous CSE studies have shown that the model is able to predict flame characteristics successfully for both premixed and non-premixed combustion modes [71] [44]. The inclusion of a second conditioning variable also successfully enabled CSE to accurately simulate partially premixed lifted jet flames [28]. However, most of these investigations were based on methane flames. Therefore the extension of the combustion model in complex hydrocarbon fuels is attractive and worth investigating.

This work provides an assessment of the performance of the novel Conditional Source-term Estimation with Flamelet Generated Manifold (CSE-FGM) combustion model in the diesel spray context. The objectives of this chapter are: (i) assessment of the application of CSE to an igniting diesel spray in both RANS and LES contexts (ii) comparison of the CSE numerical results with available experimental results and previous numerical simulations. First both RANS and LES results for "Spray A " baseline condition are provided. A further assessment of the new CSE approach is presented comparing the measured quantities. The experimental data is taken from the engine combustion network (ECN). In particular, ignition delay, lift-off and flame location are discussed. The flame's temporal evolution, ignition behaviour and stabilization mechanism are also investigated. The main differences of the predicted flame structure described by the representative species and temperature distribution are elaborated in detail.

7.2 Formulation

For simulations that are not fully resolved i.e. RANS and LES, obtaining filtered or averaged reaction rates directly from filtered or averaged values of the scalar field can lead to considerable discrepancies compared to fully resolved results. CSE seeks closure of the chemical source term using the same first order conditional moment closure hypothesis used in CMC. However, instead of solving transport equations for conditionally averaged scalars, CSE estimates conditional means from unconditionally averaged scalars. Similar to CMC, the mean conditional chemical source term for species k is written as:

$$\overline{\dot{\omega}_k|\eta} \approx \dot{\omega}_k(\overline{T|\eta}, \overline{Y_k|\eta}, \overline{\rho|\eta}) \tag{7.1}$$

where η is the discretised conditioning variable, which for non-premixed combustion is chosen as mixture fraction. $\overline{T|\eta}$,$\overline{Y_k|\eta}$ and $\overline{\rho|\eta}$ are the conditional temperature, mass fraction of species k and density respectively. The mean unconditionally averaged chemical source term is therefore:

$$\bar{\dot{\omega}}_k(\vec{x}, t) = \int_0^1 \langle \dot{\omega}_k|\eta \rangle (\eta, \vec{x}, t)\tilde{P}(\eta, \vec{x}, t)d\eta \tag{7.2}$$

In this equation, $\tilde{P}(\eta, \vec{x}, t)$, Favre averaged PDF of mixture fraction, is usually assumed to be a β-function [42]. Similarly the unconditionally averaged scalar at any spatial location $\vec{x}$ and time t, such as Favre averaged species mass fraction $\tilde{Y}_k$ can be expressed as

$$\tilde{Y}_k(\vec{x}, t) = \int_0^1 \langle Y_k|\eta \rangle (\eta, \vec{x}, t)\tilde{P}(\eta, \vec{x}, t)d\eta \tag{7.3}$$

The conditionally averaged scalars are then computed through inversion of Equation 7.3. At this point it is necessary to discuss properties and tools that can simplify the inversion process. DNS studies have shown that the spatial gradient of conditional means are small, therefore it is reasonable to assume some spatial homogeneity of the conditional means for many flows [18]. With this assumption a group of localised cells, referred to as an ensemble, may be selected in the flow field with statistical homogeneity in conditional averages:

$$\langle Y_k|\eta\rangle(\vec{x},t) \approx \langle Y_k|\eta\rangle_A \qquad x \in A \tag{7.4}$$

where $\langle Y_k|\eta\rangle_A$ is the ensemble conditional average of species k mass fraction. Equation 7.3 is then rewritten as:

$$\tilde{Y}_k(\vec{x},t) = \int_0^1 \langle Y_k|\eta\rangle_A \tilde{P}(\eta,\vec{x},t)d\eta \tag{7.5}$$

In practice, these ensembles are defined as CSE domains and the division of CSE domains ultimately depends on particular flow characteristics. In non-premixed combustion, ensembles are typically divided along the axial direction, taking the advantage of weak radial dependence of conditional averages [158]. In order to produce an independent solution, while minimising the computational cost, the number of ensembles is best determined through a sensitivity analysis [71]. To compute conditional averages, Equation 7.5 can be treated as a Fredholm equation of the first kind with $\tilde{P}(\eta,\vec{x},t)$ as the kernel [151]. Using numerical expression the equation can be noted as:

$$\vec{b} = \mathbf{A}\vec{\alpha} \tag{7.6}$$

Where $\vec{b}$ is the unconditional Favre mean mass fraction of species k at $\vec{x}$ position. $\mathbf{A}$ is an $N \times M$ matrix of the integrated PDF over some interval of the mixture fraction, where N is the number of points in each ensemble and M being the number of bins in mixture fraction space, and α stands for the conditional mean at the Mth mixture fraction bin. In matrix notation, $\mathbf{A}$ can be computed using:

$$A_{jm} = \int_{\eta 1}^{\eta 2} \tilde{P}(\eta_m,\vec{x},t)d\eta \tag{7.7}$$

The solution of Equation 7.6: $\vec{\alpha} = \mathbf{A}^{-1}\vec{b}$, is sensitive to any perturbations in the system which makes it an ill-posed problem [48]. There are several ways of addressing this issue. Bushe and Steiner [18] proposed to minimize the residual of Equation 7.5 and the conditional averages' derivatives with respect to mixture fractions. A more common method, *Tikhonov Regularisation*, was later introduced by Grout *et al.* [44]. This regularization method is based on prior knowledge of the solution, and can be applied to Equation 7.6 by reformulating it into a minimization problem (a least-square problem):

$$\vec{\alpha} = argmin \left\| \begin{bmatrix} A \\ \lambda I \end{bmatrix} \vec{\alpha} - \begin{bmatrix} \vec{b} \\ \lambda \vec{\alpha}^0 \end{bmatrix} \right\|_2^2 , \tag{7.8}$$

where notation $\|\cdot\|_2$ is the L2 norm of a vector, I is the identity matrix, λ is the regularization parameter, which is evaluated based on the characteristics of the inversion problem, and $\vec{\alpha}^0$ is the prior knowledge of solution which may take any initial value as the solution will be independent of this. However, values close to the final solution of $\vec{\alpha}$ can provide a faster convergence which could significantly reduce the computational cost. An option for prior solution would be using solutions from the previous time-step and the regularization parameter is set to [44]:

$$\lambda = \frac{Tr(A^T A)}{I} \tag{7.9}$$

where Tr is the trace of the matrix. In this study the regularization solution is set to be the flamelet solution. Finally LU decomposition can be applied to α to solve Equation 7.6. CSE is more computationally efficient compared to CMC owing to this inversion process. It also possesses the known advantage of CMC that no assumptions are made regarding flame regimes. Similar to CMC, doubly Conditional Source-term Estimation (DCSE) can also be used to predict combustion instabilities such as reignition and extinction. Dovizio *et al.* [28],[27] studied both turbulent stratified V-shaped flames and a series of lifted turbulent jet flames using DCSE. The local ignition/extinction phenomenon was successfully captured in both cases. Apart from all the advantages of CSE, directly including detailed chemistry in CSE is still challenging; especially with hydrocarbon fuels, which involve hundred of species and reactions. Inverting each specie in these fuels would be computationally prohibitive and species transport equations will be too stiff for any current ODE solvers to handle. Therefore a reduced chemistry model of some sort is necessary so that a limited number of scalars can represent the detailed chemistry. The entire solving process is depicted in Figure 7.1 which includes the interactions of each component in CSE.

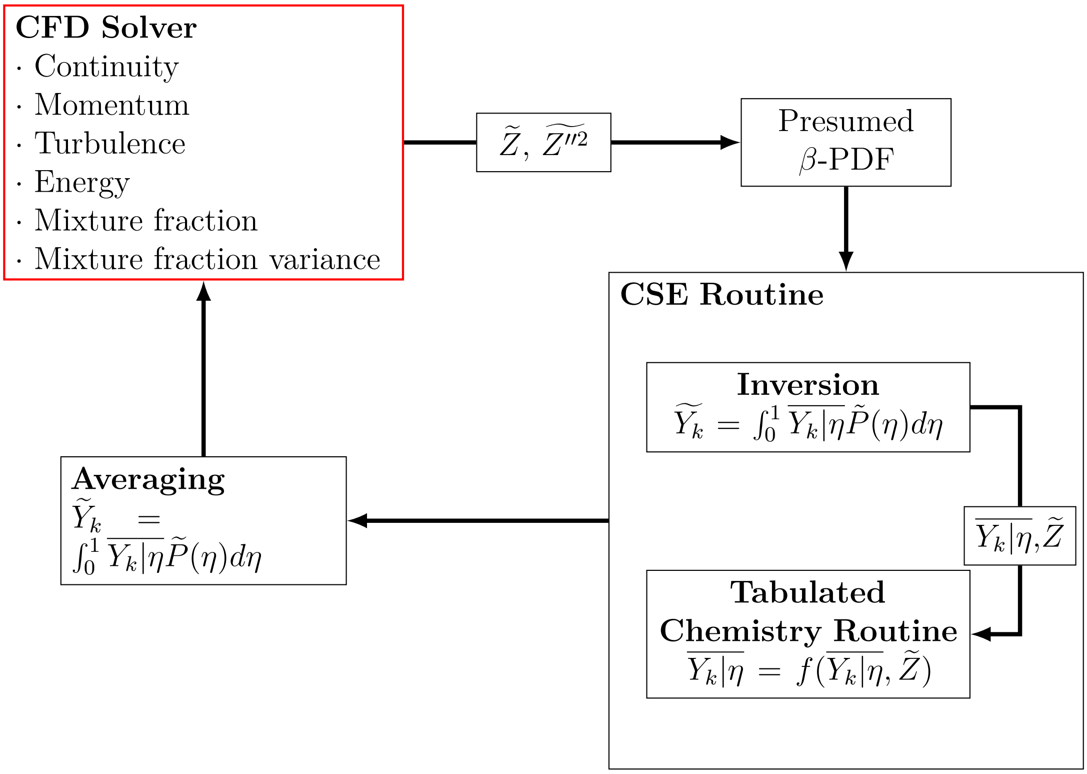

Figure 7.1: CSE routine structure

7.3 Tabulated Chemistry Approach

As mentioned before, a chemistry reduction and tabulation method is essential for the accuracy and speed of a CSE solution. When first implemented, Bushe and Stainer [18] used a single-step chemistry CSE to compare the results with DNS [18]. Later a two-step reduced chemical kinetic mechanism was used to study a piloted methane/air diffusion flame [140]. These studies have shown reasonable agreement with DNS and experimental data and proved the predictive capabilities of CSE. However, a more sophisticated chemistry reduction mechanism is needed for practical fuel studies. The most common models presently used to reduce chemistry include the partial equilibrium (PEA) method [102] and quasi steady-state approximation (QSSA) [75]. In these methods, the species and equations selected to describe the reduced chemical mechanism are derived individually for each mechanism. Another alternative method based on these two traditional methods is Rate-Controlled Constrained Equilibrium (RCCE) [57]. An advantage of this method is that major and minor species are treated as parameters in equations and various reduced mechanisms are generated and tested automatically. Recently, new techniques involving full chemistry tabulation during pre-processing have been developed. These techniques include the Intrinsic Low Dimensional Manifold (ILDM) [78], Invariant Constrained-equilibrium Edge Pre-Image Curve (ICE-PIC) [119] and methods originating from flamelet concepts [94].

Intrinsic Low-Dimensional Manifolds

Because of the wide range of time scales existing in a chemical reacting system, processes in the system can be divided into two categories: processes that occur at slow or intermediate time scales and fast equilibrium processes [77]. The Intrinsic Low-Dimensional Manifold (ILDM) method first introduced by Maas and Pope [78], is based on the fact that reaction systems converge (after the fast processes are completed) onto lower-dimensional manifolds in which reactions proceed only according to longer time scales. For non-premixed combustion these time scales are closely related to turbulent mixing. The idea of ILDM is to find such manifolds that could describe the whole chemical reaction system with a lot less variables. The detailed process of defining these manifolds can be found in [78].

Low dimensional manifolds are usually pre-calculated and stored as look-up tables for combustion applications. Thermochemical properties of the reaction can then be evaluated during combustion simulation via progress variables. These manifolds are generated solely from the reaction system itself, therefore making them applicable to various flame configurations. Maas and Pope [77] used an ILDM to model a perfectly stirred flow reactor, whereas Huang [51] studied natural gas combustion under engine-relevant conditions. Recent developments have made the ILDM an even more promising candidate for CSE application: Gicquel *et al.* [40] used a Flame Prolongation of ILDM (FPI) method to accommodate low temperature conditions, as diffusion processes are required to be included in generating appropriate manifolds for low temperature combustion. A more accurate algorithm, the Slow Invariant Maniflods (SIM) method, was developed by Nafe and Maas [89] to increase the efficiency of generating ILDMs. In addition, the tabulation process has also been studied to reduce the required memory storage. An *in-situ* adaptive tabulation (ISAT) method was used to build manifolds as needed during simulation [113]. Although ILDM has shown promising results in reducing chemical mechanisms, limited applicability has been found with relatively complex fuels such as n-Heptane and n-dodecane. Aglave *et al.* [2] applied ILDM to diesel engine modelling which successfully improved the predictions of pollutants.

7.3.1 Trajectory Generated Low-Dimensional Manifolds

Trajectory Generated Low Dimensional Manifolds (TGLDM) were proposed by Pope and Maas [79] as an alternative way to obtain low dimensional manifolds. TGLDM generates manifolds by integrating the governing ODEs of a chemical reaction system based on physically realizable initial states. The starting point of a manifold is determined by optimization criteria based on conservation of species mass fraction. The manifolds will eventually reach an equilibrium state. Theoretically, if an attractive manifold does exist for a chemical system, trajectories having initial states on the manifold will stay on the manifold. The advantages of TGLDM include that it guarantees a converged solution and the reaction vector always stays tangential to the trajectory. The tabulation process is done before the reaction flow simulation and transport equations are solved for: continuity, momentum and particular species of interests.

TGLDM have been successfully integrated into combustion models such as CSE to study different combustion problems. Huang and Bushe [158] studied methane-air jet at engine relevant conditions based on a two dimensional manifold built on the CO_2 - H_2O plane. Autoignition characteristics were successfully captured using a CSE-TGLDM solver. Wang *et al.* [155] extended the application of the TGLDM model by combining it with a Stochastic Particle Model (SPM)[41] to describe the autoignition of a methane jet more accurately. The resultant method was capable of analyzing fluctuations in ignition delay due to randomly chosen chemical reaction paths. CSE-TGLDM was also implemented in an LES environment which successfully predicted major species and temperature fields, as well as conditional averages of a piloted non-premixed turbulent methane jet flame (Sandia flame D) [156]. Again, most of these studies were conducted using simple fuels such as hydrogen or methane; recently, Asenbaur [4] studied the ignition characteristics of diesel spray using CSE-TGLDM. In her work, the TGLDM table was generated using the averaged mass fractions Y_{Co_2} and Y_{H_2O} with different mixture fraction Z values as progress variables. However, the TGLDM calculation had to be aborted after ignition as the methane assumption used in generating the table was found to be invalid for n-heptane after ignition. N-dodecane manifold generation through TGLDM is also conducted by the author. However, the implementation was found to be unsuccessful. Therefore, for this study a new approach for chemistry tabulation is needed to use the CSE combustion model for a diesel surrogate under engine relavent conditions.

7.3.2 Flamelet Generated Manifold (FGM)

In this study chemistry is included in CSE using the flamelet generated manifold approach. It is worth noting here that FGM is not used as a combustion model, as is common in previous studies, but rather as a chemistry tabulation strategy for CSE. However, the chemistry generation process is identical to the earlier works described in Chapter 5 and Chapter 6. The generation process is stated again here. As shown in Figure 7.2 (a), generating the manifold first starts with solving a transient counter-flow diffusion flame at a strain rate of 500 s^{-1} from an initially mixed (green line), but non-reacting state and then tracking this flame (black lines) through ignition up until quasi steady-state (red line). Once the flamelet solutions are computed, they are parametrised against mixture fraction, Z, and reaction progress variable, c, with a manifold resolution of 100x100 quadratically spaced points (shown in Figure 7.2 (b)). The definition of both mixture fraction, Z, and reaction progress variable, c, is identical to previous FGM studies. A sub-space describing the FGM generation process is shown in Figure 7.3 (a) and the resultant manifold is shown in Figure 7.3 (b).

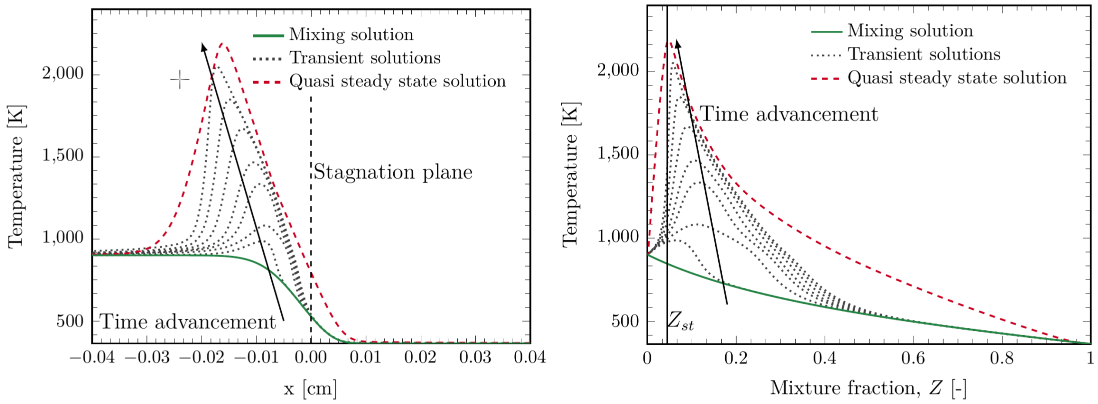

(a) Physical space

(b) Mixture fraction space

Figure 7.2: Temperature evolution for an igniting counter-flow diffusion flame with n-dodecane: a=500 s^{-1}, T_{fuel}=363 K, T_{Ox}=900 K, P_{amb}=6.0 Mpa (a) physical space (b) mixture fraction space

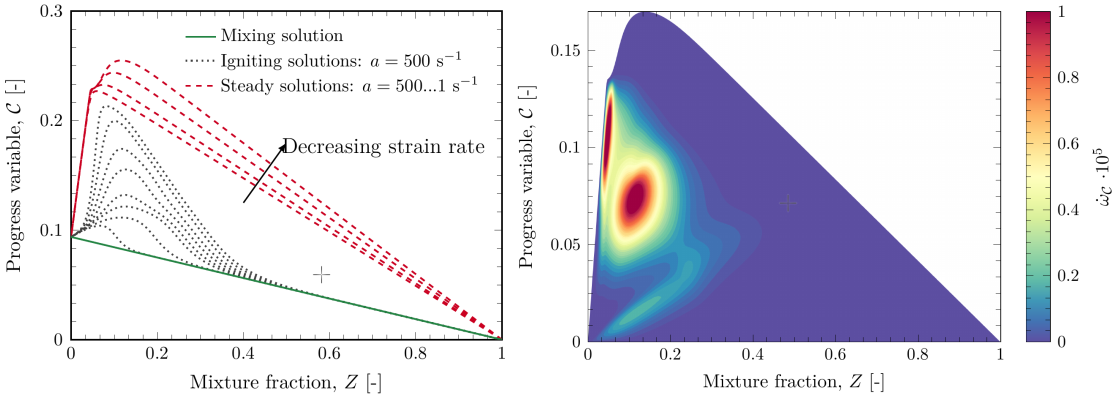

(a) Mixture fraction space

(b) Mixture fraction space

Figure 7.3: (a) Schematic representation of progress variable as a function of mixture fraction (b) reaction rate as a function of progress variable and mixture fraction

7.3.3 Complete CSE-FGM Implementation

The complete interaction of the CSE-FGM combustion model with the CFD code is shown in Figure 7.4. Coupling between the CFD solver and combustion model is achieved by solving three additional transport equations for the progress variable, the mixture fraction and the mixture fraction variance. The Favre averaged mixture fraction ($\widetilde{Z}$), and its variance ($\widetilde{Z''^2}$) are used in the computation of the β-PDF. This along with the Favre averaged progress variable ($\widetilde{\mathcal{C}}$) are parsed into the CSE routine, where the conditionally averaged progress variable ($\langle \mathcal{C}|\eta \rangle$) is computed via inversion as described earlier. The conditionally averaged progress variable along with the Favre averaged mixture fraction are used to lookup the conditionally averaged reaction rate of the progress variable ($\langle \dot{\omega}_{\mathcal{C}}|\eta \rangle$) and conditional species mass fractions ($\langle Y_k|\eta \rangle$) from the FGM table. These are then integrated with the β-PDF to retrieve the respective mean values, which are parsed back into the CFD solver.

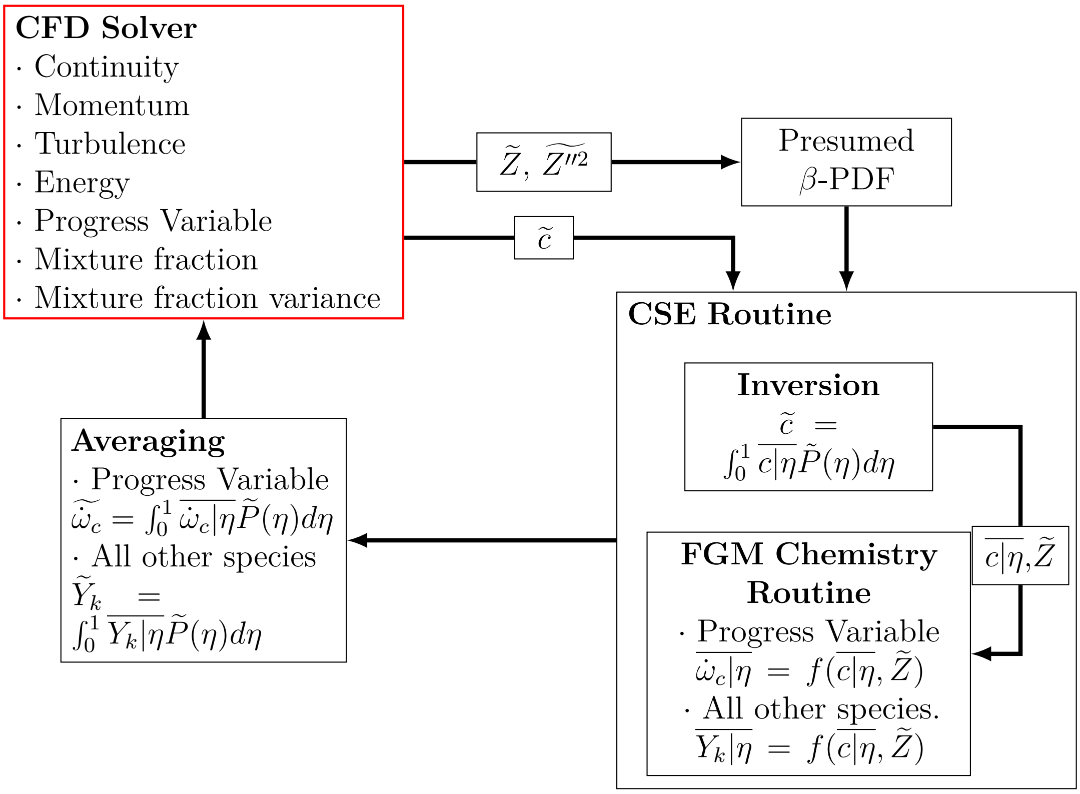

Figure 7.4: CSE-FGM routine structure

7.4 Computational Setup

The computational setup for RANS is identical to that provided in Chapter 4, therefore in this section only LES computational setup will be detailed. For LES simulations in this study, the one-equation, viscosity-based LES model was used.

This involves using the sub-grid turbulent kinetic energy, k_{sgs} to compute the turbulent viscosity as:

$$\nu_t = C_k k_{sgs}^{\frac{1}{2}} \Delta \tag{7.10}$$

where C_k is a model constant and commonly set as 0.05 and Δ is the cube root of the cell volume. The sub-grid kinetic energy is modelled through a transport equation developed by Yoshizawa *et al.* [168] and Menon *et al.* [85] $k_{sgs} = \frac{1}{2}\left(\widetilde{u_i u_i} - \tilde{u}_i \tilde{u}_i\right)$, is modelled with a transport equation as:

$$\frac{\partial \bar{\rho} k_{sgs}}{\partial t} + \frac{\partial \bar{\rho} \tilde{u}_i k_{sgs}}{\partial x_i} = -\tau_{ij} \frac{\partial \tilde{u}_i}{\partial x_j} - \epsilon + \frac{\partial}{\partial x_i}\left(\bar{\rho} \frac{\nu_t}{\sigma_k} \frac{\partial k_{sgs}}{\partial x_i}\right) \tag{7.11}$$

The sub-grid stress tensor is calculated using:

$$\tau_{ij} = -2\nu_t \tilde{S}_{ij} + \frac{2}{3} k_{sgs} \delta_{ij} \tag{7.12}$$

where $\tilde{S}_{ij}$ is the strain rate tensor and δ_{ij} is the Kronecker operator. The sub-grid dissipation in this model, ϵ_{sgs} is given as:

$$\epsilon_{sgs} = C_\epsilon \frac{k_{sgs}^{\frac{3}{2}}}{\Delta} \tag{7.13}$$

where C_ϵ is a model constant and typically set as 1.0.

In LES, the mixture fraction variance can be approximated through a dynamic model:

$$\widetilde{Z''^2} = C_{var} \Delta^2 \left| \frac{\partial \widetilde{Z}}{\partial x_j} \right|^2 \tag{7.14}$$

where C_{var} is a dynamically computed model coefficient.

The computational domain for both RANS and LES is identical. The injector is positioned centrally with injection into the axial direction. All boundaries are set as non-slip walls with constant temperature of 461 K as measured in the experiment. The simulation conditions are set to the 900 K ECN "Spray A "baseline conditions. The injector nozzle diameter is 0.084 mm with a discharge coefficient of 0.89 corresponding to Spray A injector 210677 [103]. For LES, a structured grid is generated at runtime with a base cell size of 1.4 mm. Adaptive mesh refinement is enabled based on both velocity (0.1 ms^{-1}) and temperature (5 K) fluctuations with minimum cell refinement of 0.0875 mm. Furthermore, a conical fixed grid refinement of 0.0875 mm is placed along the injector axis to better resolve this high velocity region. In order to maintain a reasonable runtime, the maximum cell count is limited to 2.6 million cells. These cell sizes were determined through a grid dependence study conducted at non-reacting conditions of the spray. Further details will be presented in Section 7.5.1. A section of the computational domain showing the computational grid and cell refinement can be seen in Figure 7.5 .

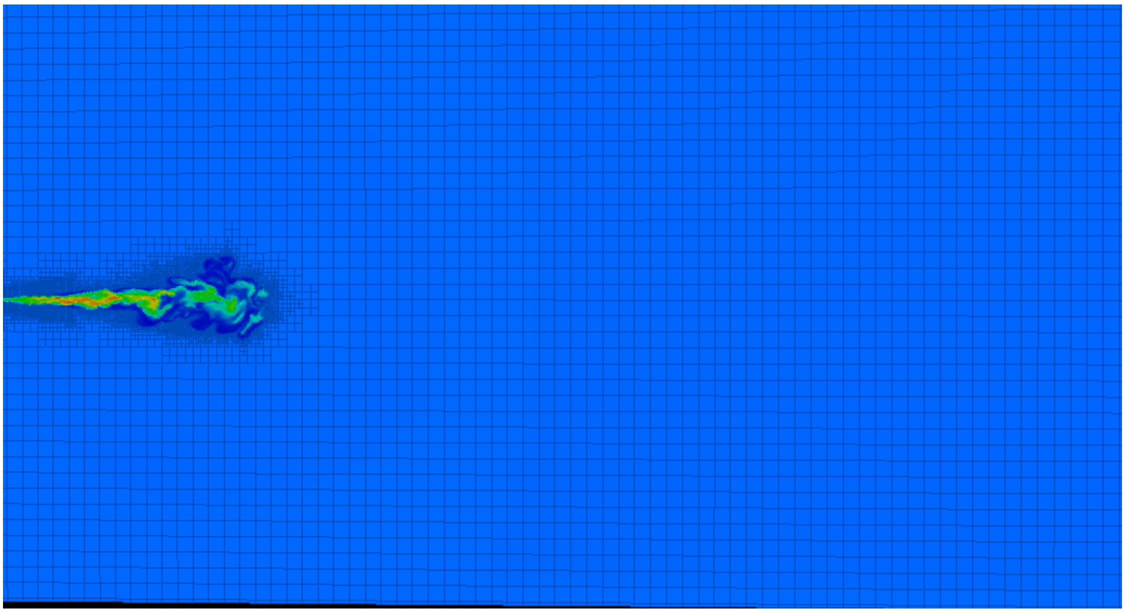

Figure 7.5: Sample section view of spray computational domain with grid refinement methods. The combustion chamber is modelled as a 108 mm cubical geometry.

7.5 Non-reacting Spray

7.5.1 LES Grid Dependence

The non-reacting spray simulation process is similar to the RANS solving process where a grid dependence study of the LES computational setup was first conducted. The mesh size of the LES sensitivity study is varied from 0.125 mm to 0.0625 mm. The detailed grid setup for grid dependence test is given in Table 7.1. For the study of the LES grid dependence, only a single realisation for each grid is conducted.

Previous study of LES non-reacting spray has shown a single realisation of LES can sufficiently represent the ensemble averaged values in terms of grid convergence [164].

Table 7.1: LES grid dependence parameters

Mesh	Coarse	Medium	Fine
Grid size [mm]	0.125	0.0875	0.0625
Max cell number$\cdot 10^6$ [-]	1.4	2.6	5.0
Spray parcels$\cdot 10^6$ [-]	0.8	2.4	3.2
Computational cost [hour]	252	672	1440

For all grid sizes, the liquid penetration shown in Figure 7.6 is seen to be more sensitive during the transient period of the spray. Similar trend is observed for the RANS simulations previously shown in Chapter 4 where, at a coarse grid, the liquid penetration spikes around 0.2 ms. Significant differences were observed for the RANS non-reacting simulation at steady-state for coarse grid. The LES simulation results are comparable to experimental data over the injection duration where the liquid penetration is shown to be insensitive to grid size after the transient period. Compared to liquid penetration, vapour penetration is more sensitive to grid sizes. Figure 7.7 shows the vapour penetration for all grid sizes where both medium and coarse grid size overpredicted the vapour penetration length. An improved prediction is achieved when using the finest grid size of 0.0625 mm. However, the medium grid size of 0.0875 mm also shows good agreement with the experimental measurements after 0.5 ms. For the balance of computational cost and accuracy a grid size of 0.0875 mm it then chosen for further studies. Similar grid sizes for LES diesel spray simulations were also found in the literature [99].

7.5.2 Non-reacting Vaporising Spray

The non-reacting spray studies also follow a similar process as the RANS studies shown in Chapter 4. However, for LES simulations, it is necessary to simulate multiple realisations for quantitative predictions. In this study, the initial random perturbations responsible for the event-to-event variability are obtained by perturbing a random seed, which affects the spray collision and break-up models. The

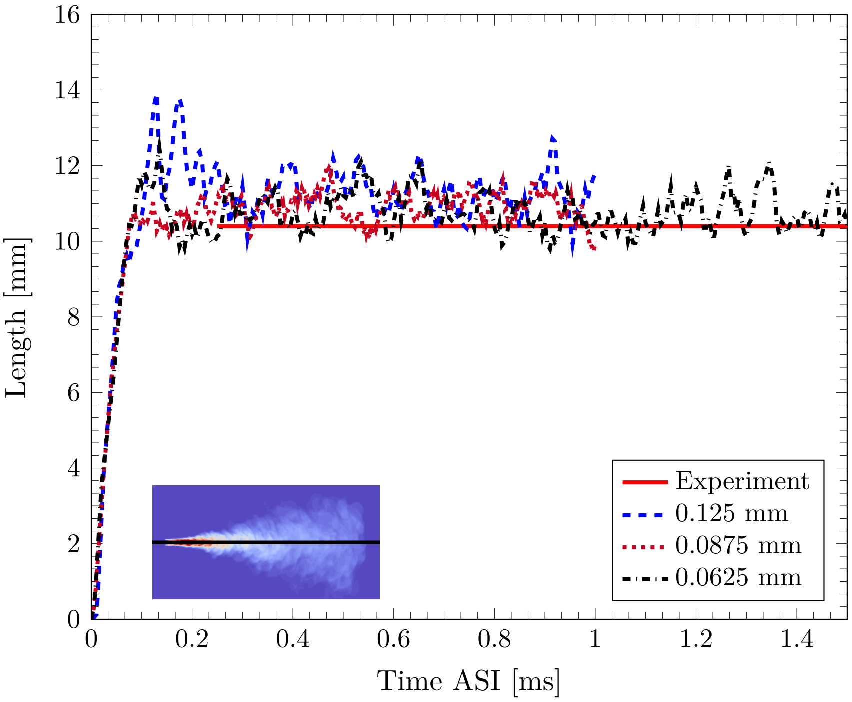

Figure 7.6: Liquid penetration length as a function of grid size. Liquid length is defined as the axial location of 97% liquid mass threshold. Experimental data repeated from [103].

effect of the random seed in the spray is expected to mimic the variations observed from one injection to the next in a realistic injector. Although this method is purely numerical, studies have shown the results from the random seed perturbations is comparable to the pertubations initiated by varying the initial ambient turbulent kinetic energy in the combustion chamber [3] [19]. In order to reduce the LES realisations while obtaining the correct statistics of the energy-containing scales of motion. Different techniques for statistical averaging for three-dimensional spray LES simulations have been extensively explored in the literature. Both time averaging and spatial averaging can be considered depending on the configuration investigated. Habchi *et al.* [45] showed ensemble averaging of 30 LES realisations is not sufficient to represent axial and radial mixture fraction distributions. However, combining realisation ensemble averaging with spatial averaging using azimuthal planes for each realisation can greatly improve the simulation accuracy. Senecal *et al.* [127] simulated ECN “Spray A” with 20 LES realisations and the results indicate that having 9 realisations is a large enough sample to capture experimental

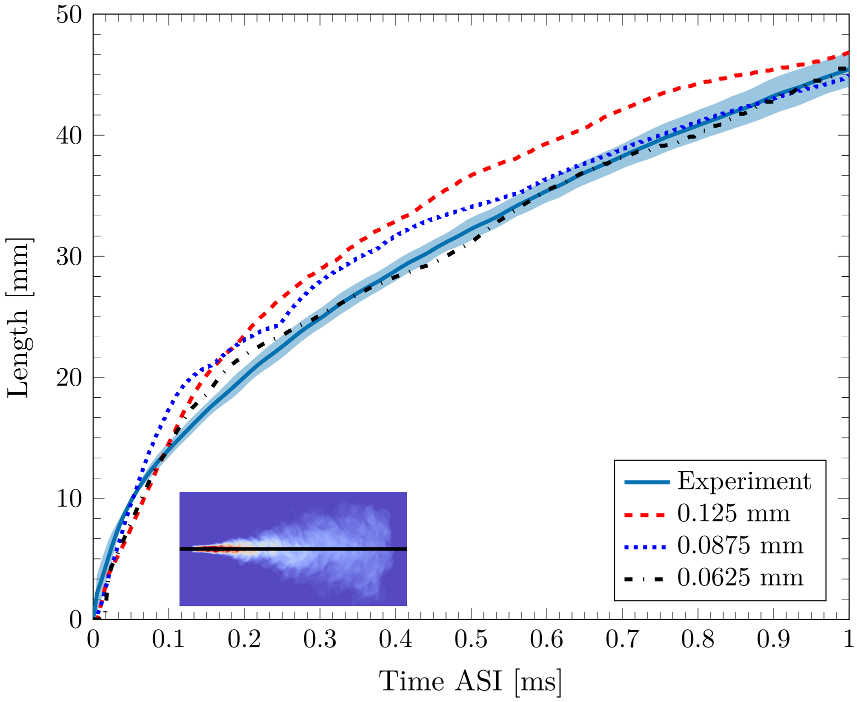

Figure 7.7: Simulation vapour penetration length as a function of grid size. Vapour length is defined as axial location of 0.1% vapour mass threshold. Shaded area represents experimental uncertainty. Experimental data repeated from [103].

velocity and mixture fraction distribution with mean absolute errors of 2.0 ms^{-1} and 0.005 respectively around 95% of the time. A more recent study from Pei *et al.* [99] found that with five LES realizations, a 98% to 99% similarity to an equivalent of 16 LES realizations for larger scale fluctuations (e.g. mixture fraction and velocity magnitude) and temperature can be achieved. For variables with shorter scale fluctuations, more LES realizations are necessary. Blomberg *et al.* [19] also used 5 realisations for each case under engine relevant conditions for a split injection diesel spray to capture the combustion recession at the end of injection. Since the computational domain and boundary conditions employed in the present study is axisymmetric, it is natural to make use of this statistical axi-symmetry to reduce the requirement for the number of LES realizations.

Before discussing the details of simulation results it is worth noting that stabilization of the gas jet is measured as the time when the head of the jet passes out of the test section. The test section is chosen to match the experimental test window which is from 17.85 mm to 50 mm in the axial direction. In the experiments, mixture fraction is measured using Rayleigh Scattering with samples captured at long delays (3.2-7.0 ms) after the start of injection and ensemble averaged over 20-40 injections depending on the test condition [107]. This is to ensure the measured jet is at steady-state, so that jet transients do no affect measurements. Experimental velocity measurements are taken with time-resolved PIV and ensemble averaged over approximately 20 injections at defined time instances after the start of injection [84]. Velocity measurements in the near nozzle region are not considered accurate as the proximity of the liquid jet generates high intensity Mie scattered light that interfere with tracer particle imaging. Additionally, the PIV particle density is too low in this region as not enough particles have been entrained in the spray. As such, only velocity measurements downstream of $x = 20$ mm will be considered.

As it is computationally prohibitive to run simulations for long durations (3.2-7.0 ms) as in the experiment, as well as quasi steady-state experimental reacting data being available before 1.5 ms – the following three approaches are used to validate the computational model with experimental measurements:

- Mixture fraction: temporal and spatial averaging of 1 LES realisation using 25 temporal samples between 1.5-2.0 ms and 12 azimuthal planes for each sample.

- Velocity field: ensemble and spatial averaging of 5 LES realisations and 12 azimuthal planes for each realisation at 1.0 ms ASI.

- Temperature field: ensemble and spatial averaging of 5 LES realisations and 12 azimuthal planes

Figure 7.9 qualitatively shows the difference in mixture fraction distribution between the 5 realisations. Spatial averaging is applied in the azimuthal direction for each realisation as illustrated in Figure 7.8. Each plane is 60 mm long and 30 mm wide, which is then discretized by 0.08 mm to preserve resolution.

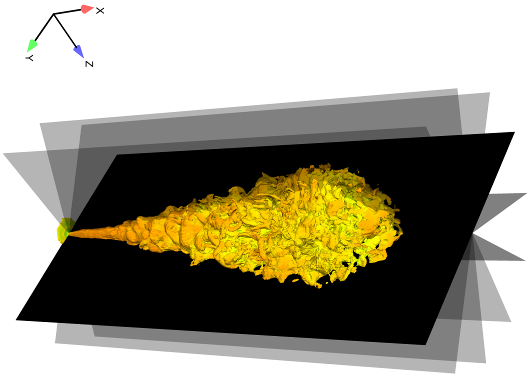

Figure 7.8: ISO volume of spray jet showing azimuthal averaging planes.

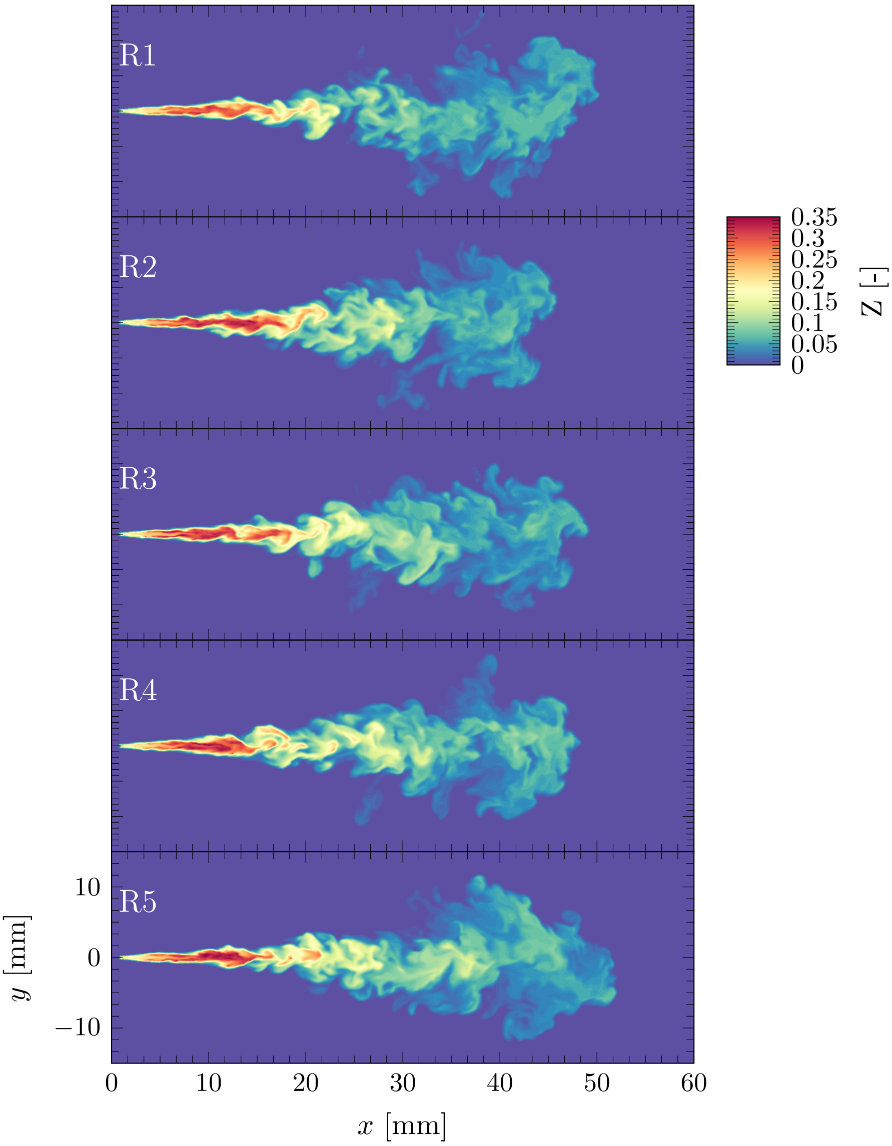

Figure 7.9: Mixture fraction distribution at 1.0 ms ASI for 5 LES realisations perturbed by a random number seed. Simulation run at the 900 K non-reacting "Spray A " baseline condition.

Figure 7.10 and Figure 7.11 compared the liquid and vapour lengths of the individual LES realisation, the ensemble averaged LES and the experiments. The uncertainty is not provided for the liquid penetration as only a mean value is provided from the experiment. The liquid penetration is well matched by the LES simulation for the given configuration. Vapour penetration length is slightly overpredicted by the LES model early in the injection duration. At steady-state both the liquid penetration and vapour penetration are well predicted compared to the experiment.

Figure 7.12 shows the simulated spray centreline axial mixture fraction comparing to the experiment. Underprediction was found across the axial distance. The standard deviation between simulation and experiment is, comparable and the predicted results fall within experimental variance. The underprediction in centreline mixture fraction is likely attributed to the early sampling time in the simulations [127]. The LES samples were collected under 2 ms while experimental mixture fraction is measure at a later stage (3.2 -7.0 ms). Previous study has shown that an increased spatial resolution can help improving the centerline mixture fraction prediction [159]. The velocity fields which are sampled at the same time instance after start of injection (1.0 ms) between simulation and experiment are shown in Figure 7.13. There is good agreement between the ensemble averaged simulations and experimental measurements across the axial distance. As expected, simulation variance is high due to the low number of samples (5).

From Figure 7.14, it can be seen that the radial profiles of simulated mixture fraction and velocity are in good agreement with experimental measurements at all chosen axial locations. The simulation underpredicts the centreline mixture fraction, however, mean and variance predictions are improved at locations away from the centreline. Similar results for the same conditions were found in other LES studies [128],[127].

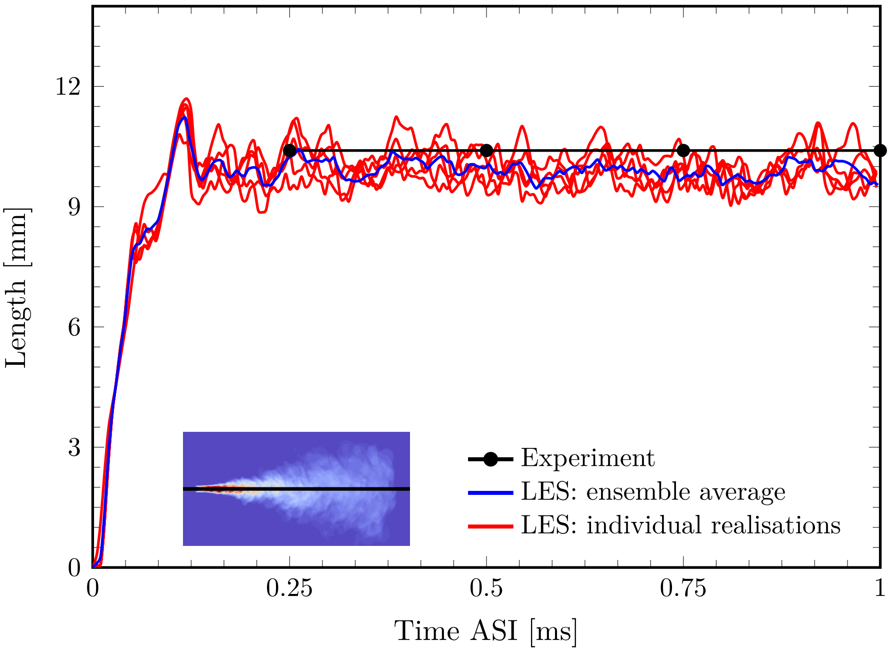

Figure 7.10: Experimental and simulation liquid penetration lengths. Liquid length is defined as the axial location of 97% liquid mass threshold. Simulation run at the 900 K non-reacting "Spray A " baseline condition.

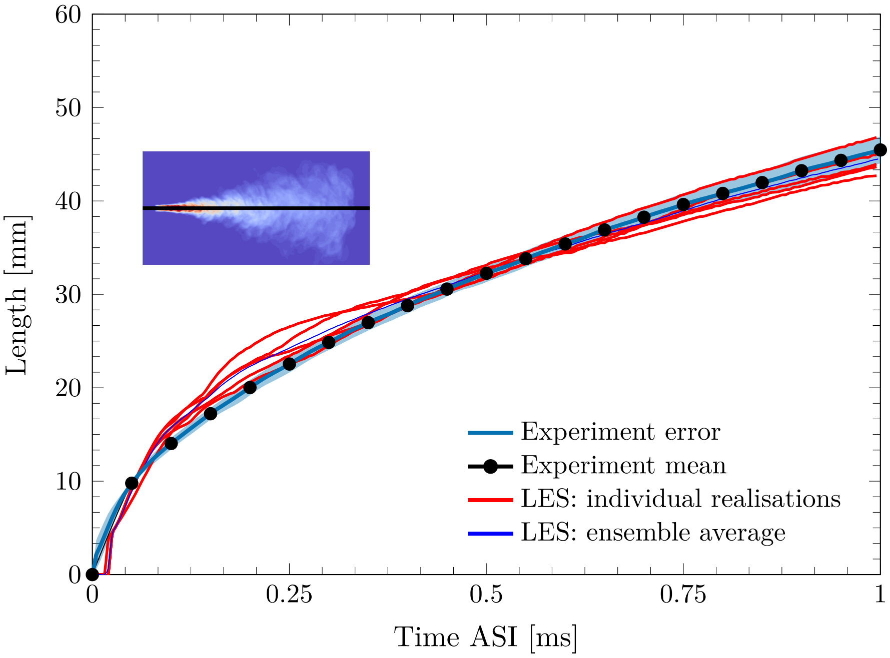

Figure 7.11: Experimental and simulation vapour penetration lengths. Vapour length is defined as axial location of 0.1% vapour mass threshold. Shaded area is the experimental uncertainty. Simulation run at the 900 K non-reacting "Spray A " baseline condition.

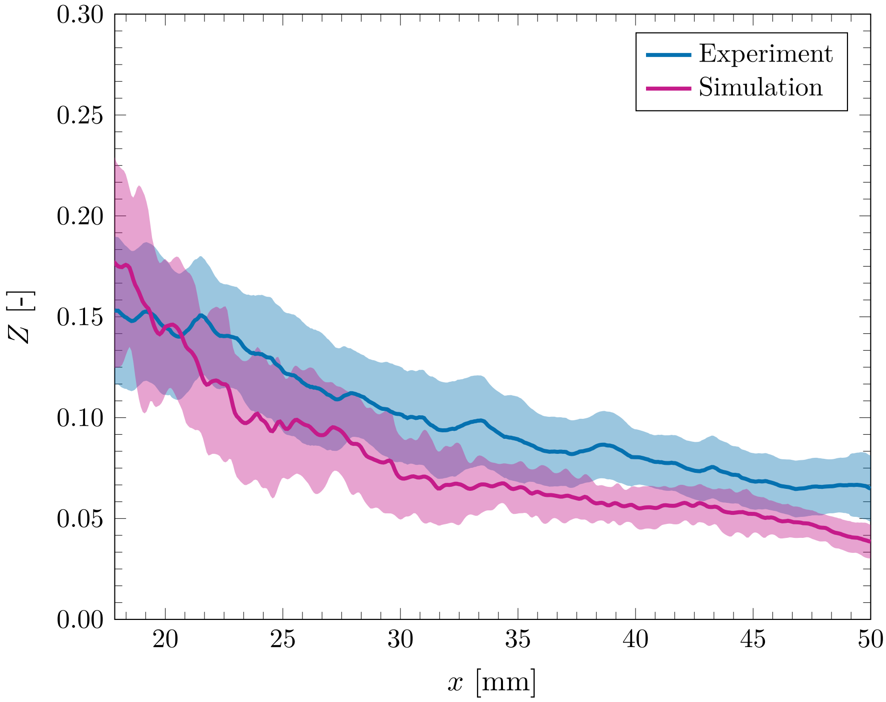

Figure 7.12: Axial comparison of experimental and simulation mixture fraction distribution. Shaded area represents standard deviation. Simulation run at the 900 K non-reacting “Spray A ” baseline condition.

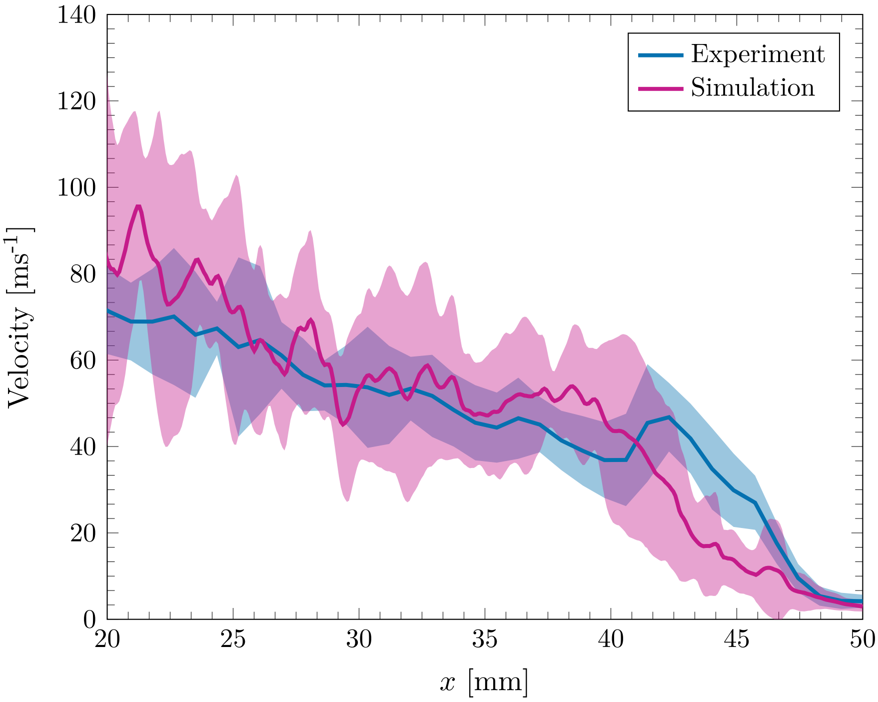

Figure 7.13: Axial comparison of experimental and simulation velocity fields at 1.0 ms ASI. Shaded area represents standard deviation. Simulation run at the 900 K non-reacting “Spray A ” baseline condition.

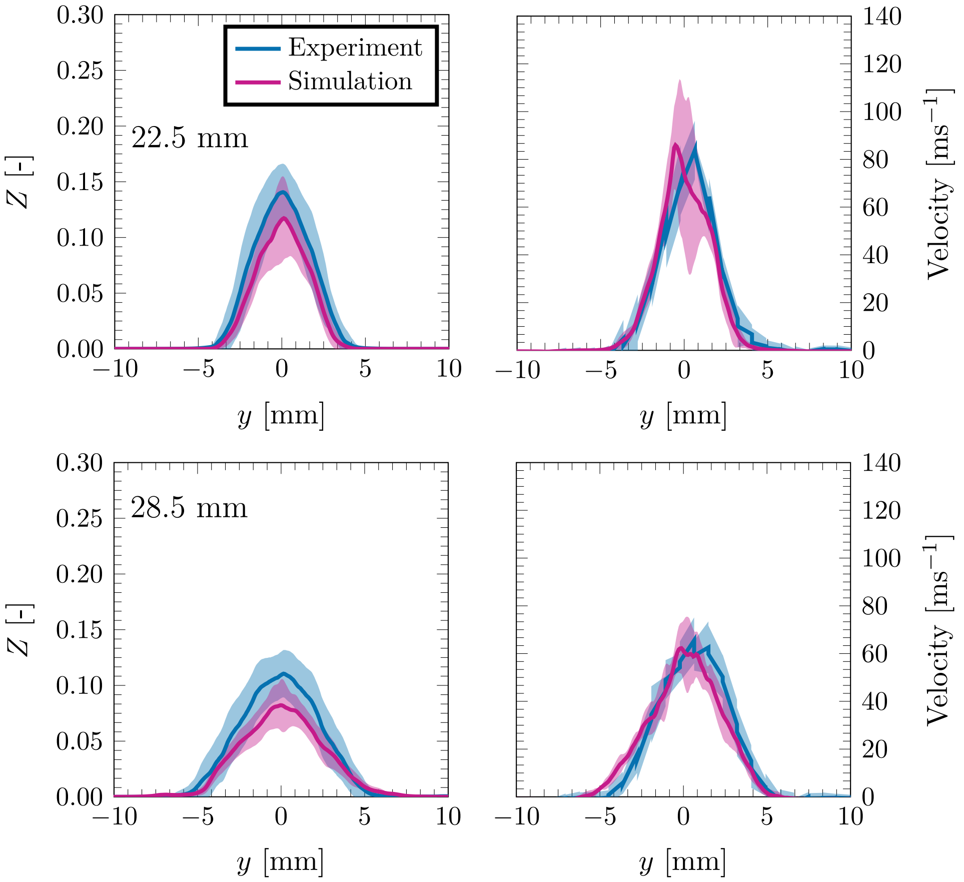

Figure 7.14: Radial profiles of mixture fraction (left) and axial velocity (right) for experiment and simulation at three axial positions. Shaded area represents standard deviation.

7.6 Reacting Spray Study

In this section, the validation and comparison of combustion models are carried out following the ECN modelling standards. Simulations are performed using the reduced n-dodecane kinetic mechanism of Yao *et al.* [166]. Before conducting the 3D simulation of diesel spray using the above chemical mechanism, a mechanism validation test is conducted in terms of the ignition delay times for homogeneous mixtures with varying equivalence ratios and initial temperatures. The same tests were conducted by Yao *et al.* [166] during the development of a skeletal mechanism, however the current study is completed using the CONVERGE 0D chemistry tool and its ODE solver, therefore confirming the numerical consistency of the current study. Figure 7.15 shows the ignition delay time comparison between CONVERGE

0D results and the available shock tube experimental results from Vasu *et al.* [149] at 20 bar. The results are consistent with those obtained by Yao *et al.* [167] where, at higher temperatures, there exists an overestimation of the ignition delay time, and at lower temperatures the present mechanism shows reasonable result compared to the experiments. For engine relevant conditions (60 bar) similar 0D studies are also conducted which are not included in this chapter. In order to further explore the capabilities of the mechanism, a study of the flame is carried out using the 1D chemistry solver CHEM1D under the investigated 3D simulation conditions. Figure 7.16 depicts the temporal evolution of the maximum temperature over the duration of the injection. The results indicate that the current mechanism is capable of capturing different stages of low temperature combustion. First stage and second stage ignition are substantially increased by the reduction of the ambient gas temperature. This observation is consistent with previous flamelet calculations [35] and simulation studies using reduced chemistry [159].

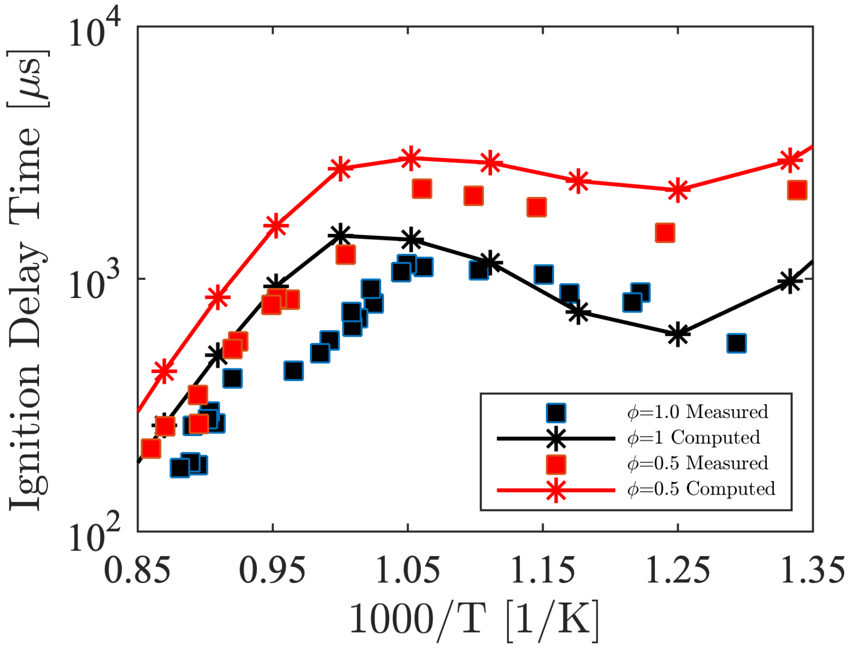

Figure 7.15: Comparison between measured ignition delay times in n-dodecane [149] and computed values from CONVERGE using Yao mechanism at $p = 20$ bar and $\phi = 0.5$ and $\phi = 1.0$ [167]

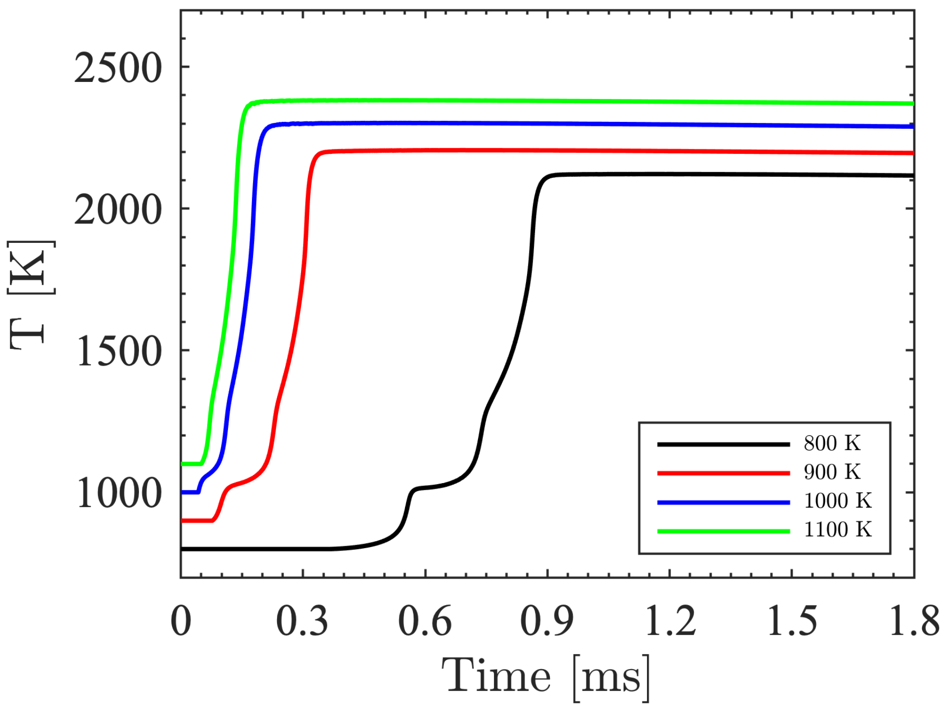

Figure 7.16: Temperature evolution of Yao mechanism under investigated conditions using 1D-FGM

7.6.1 Flame Temporal Evolution and Ignition Study

Table 7.2 quantitatively shows the comparison of measured and simulated ignition delay and flame lift-off length. The definition of these two parameters are the same as described before in Chapter 5. It can be seen that both the CSE-FGM RANS and LES simulations are able to successfully capture both combustion metrics to a high degree of accuracy. For the RANS study, a slight overprediction is observed for flame lift-off prediction.

Figures 7.17 and 7.18 show the temporal evolution of mixture fraction and temperature field between RANS and LES for the ECN "Spray A" 900 K baseline condition. The black lines in Figure 7.18 temperature contour represent stoichiometric mixture fraction (Z_{st}=0.045). It can be observed from both figures that a significant fluctuation of mixture fraction and temperature field is present in the LES simulations compared to those of RANS simulations at the same timestep. This can result in different ignition behaviour, which will be examined in detail later. It is also

Table 7.2: Ignition delay time and flame lift-off length for ECN "Spray A" baseline condition. Experimental data repeated from [103].

Baseline (900 K, 15% O_2)	Experiment	CSE-FGM/LES	CSE-FGM/RANS
Ignition delay time [ms]	0.40-0.45	0.408	0.413
Flame lift-off length [mm]	15.80-17.90	18.08	19.31

worth noting that for RANS simulations the Z_{st} line crosses the middle of the high temperature field, which is closer to the jet centerline, overlapping more of the high temperature region compared to LES simulations. The LES Z_{st} line is located at the edge of the flame where high temperature reactions exist. The reason for this is that the LES simulation is a single realization with spatial averaging which resulted in a thin flame due to very fine mesh. In contrast, RANS is an ensemble averaged simulation which thickens the flame and moves the Z_{st} line to the center of the flame. Additional studies for ensemble averaged LES results will be investigated later.

Previous experimental studies have identified that the combustion of a diesel spray can be divided into two stages [24]. Due to the complex physical processes included in spray combustion modelling, understanding autoignition or two stage ignition processes are very challenging. Therefore the capability of the CSE-FGM combustion model in capturing this critical event is further investigated. The first stage of ignition in this study is defined as events where the temperature rise is less than 400 K above the ambient temperature, therefore making it easier to distinguish from the main high temperature combustion event. In order to better illustrate the typical two-stage ignition behaviour of the n-dodecane fuel jet, Figure 7.19 divides the LES simulated flame evolution into two different parts. At 0.30 ms ASI, a slight increase of temperature is observed at the outer edge of the jet (Z_{st}) around 20mm downstream of the nozzle. This can be seen as the beginning of low temperature reactions where low temperature heat release is observed. The onset of second-stage ignition takes place approximately at 0.40 ms ASI and occurs in the head of the jet where the velocity field is relatively low. The vapour temperature here rises 300-400

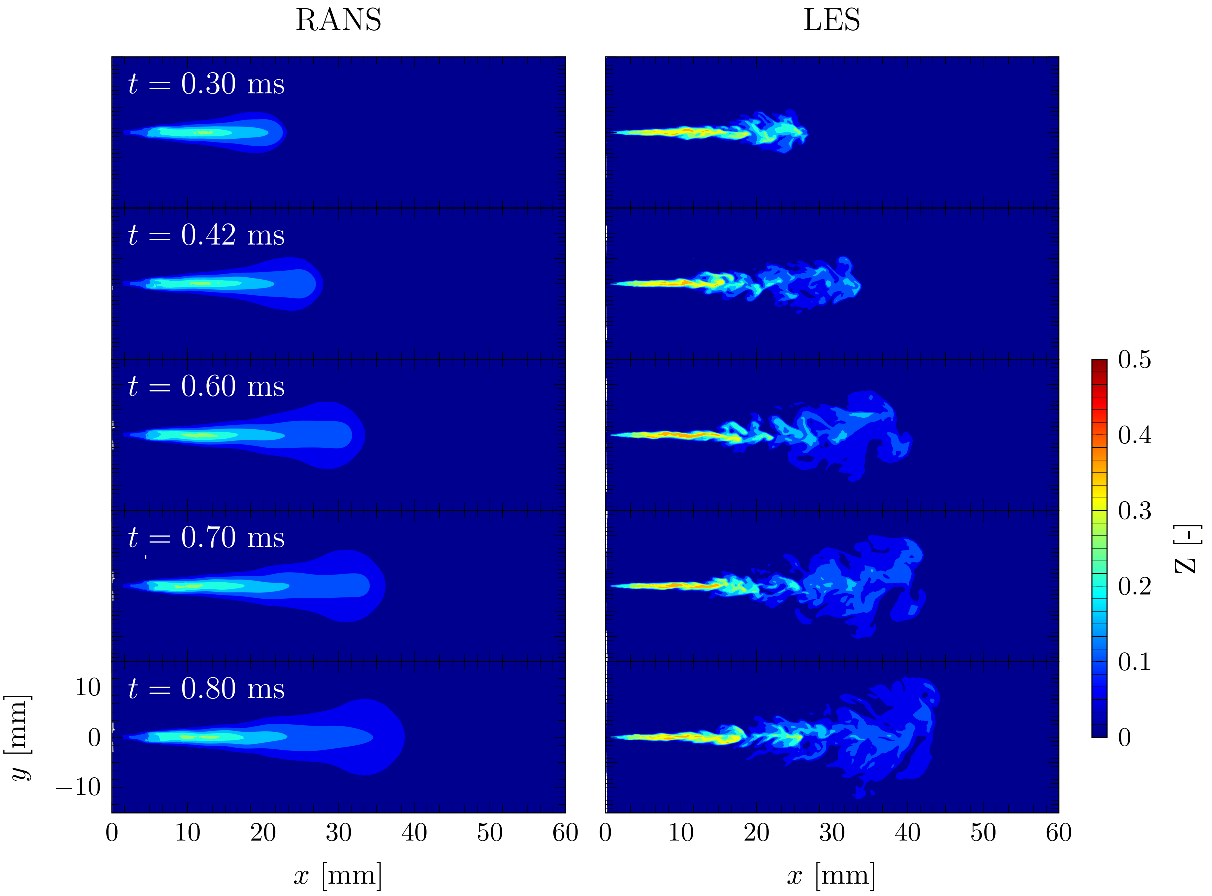

Figure 7.17: Instantaneous mixture fraction fields for CSE-FGM RANS (left) and LES (right) simulations at the 900K "Spray A " baseline condition. The time after start of injection is shown at the top left of image. The black line is the stoichiometric mixture fraction contour

K above the ambient temperature and volumetric ignition takes place with multiple ignition kernels.The higher temperature region (around 1000K) region exists entirely within the Z_{st}. This is followed by the expansion of a high temperature diffusion flame (0.6-0.8 ms), which eventually stabilizes downstream of the injector. It can be observed from Figure 7.18 that at around 0.7 ms the flame has approached quasi-steady state. This finding is consistent with the chemical mechanism study from Chapter 6 and other studies [3][166]. Additionally, at approximately $x = 30$ mm, the diffusion flame begins to thicken radially. This phenomenon has been observed in previous studies [99] and is attributed to the recirculation zone behind the head of the jet. These vortices enhance turbulence levels locally and lead to thickening of the flame in this area.

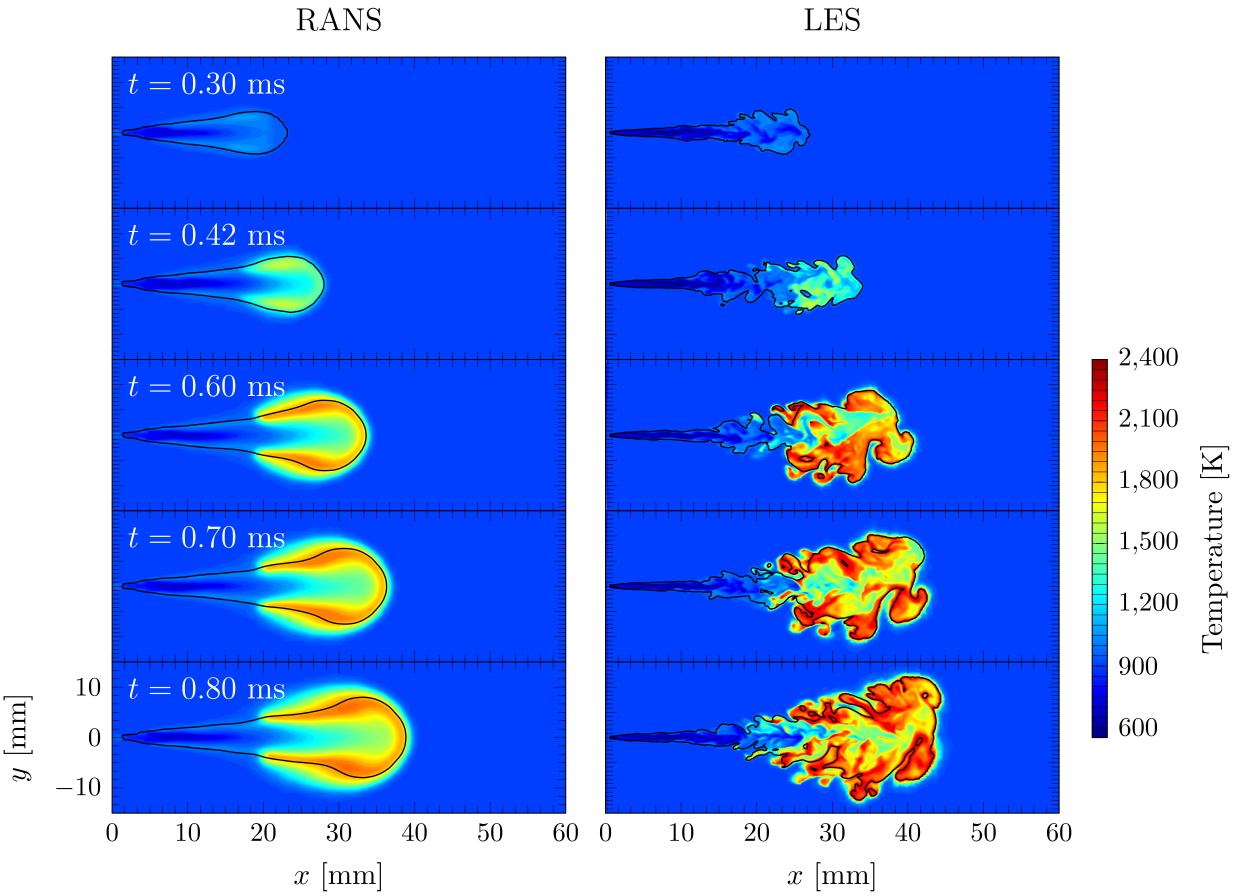

Figure 7.18: Instantaneous temperature fields for CSE-FGM RANS (left) and LES (right) simulations at the 900K "Spray A " baseline condition. The time after start of injection is shown at the top left of image.

Following the study of flame spatial transient behavior, the temporal evolution of scatter plot of the temperature in mixture fraction space are given in Figure 7.20. For both RANS and LES at 0.19 ms, all the points are clustered around the mixing line. Prior to second stage combustion at around 0.40 ms, both RANS and LES points are in rich mixture. Minor species are also given here to assist the study of ignition behaviour. It is worth noting that LES predicts an abrupt transition in the mixture fraction space for certain temperatures during the main combustion stage, whereas RANS gives a smoother transition of temperature at different mixture fractions. This is likely due to the single LES realisation that promotes an abrupt transition in the ignition process. For RANS, the "ensemble averaging" process likely smooths out this apparent abrupt transition. At second

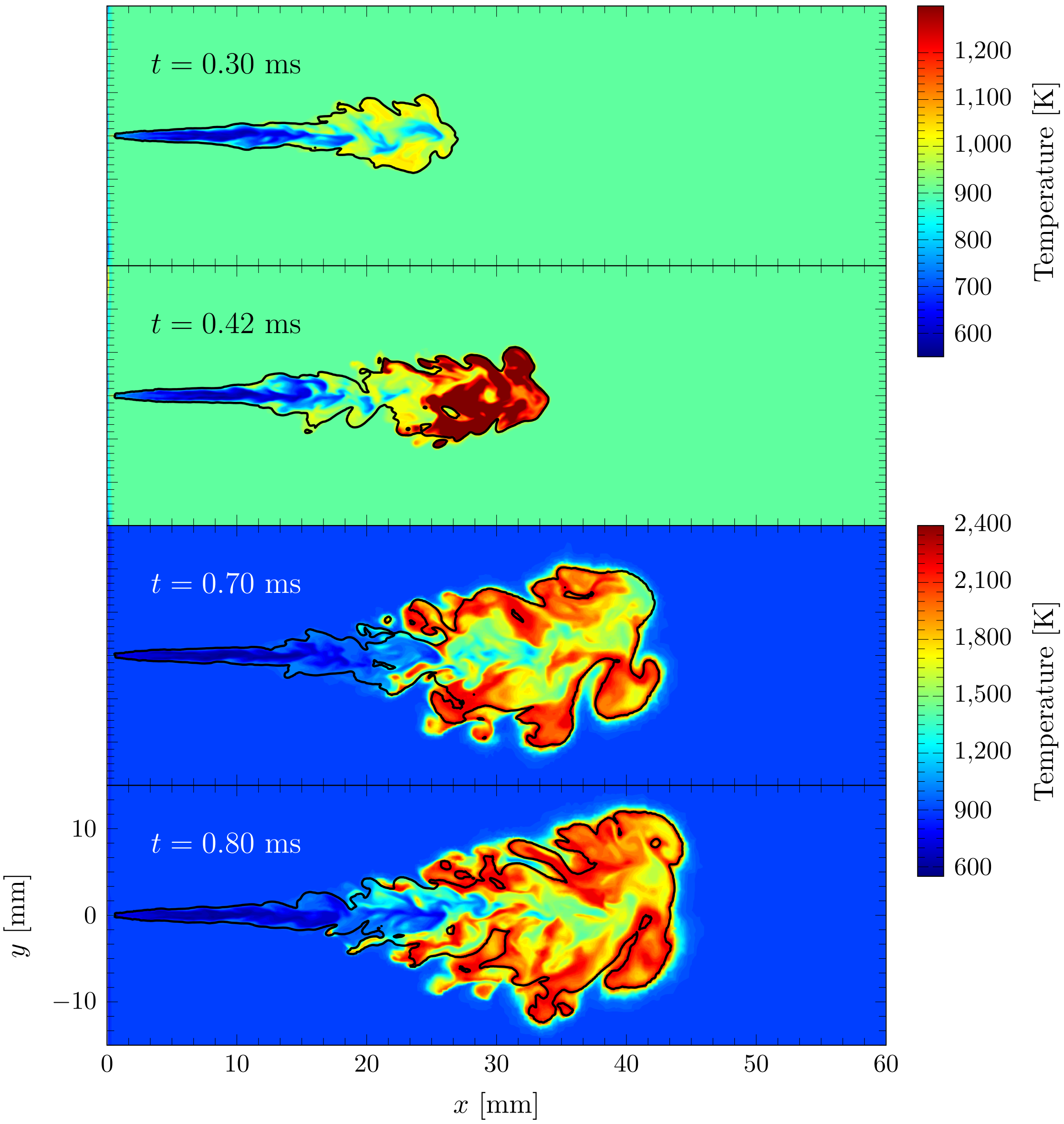

Figure 7.19: LES Contour plot of termperature for first stage (top two) and second stage(bottom two) ignitions at the 900K "Spray A" baseline conditions. The black line represents Z_{st}

stage combustion, both RANS and LES shows the combustion event favouring a mixture fraction of less than 0.15. The temperature continues to rise and the mean termperature becomes closer to the equilibrium state.

To further the understanding of n-dodecane spray ignition processes, several key intermediate species, such as hydrogen peroxide (H_2O_2), hydroxyl (OH) and formaldehyde (CH_2O) were included alongside the LES temperature-mixture fraction plot in Figure 7.21. The black solid lines indicate the position of stoichiometric mixture fraction. The combustion process of n-dodecane follows [171], where the generation of H_2O_2 and CH_2O is identified as the first stage of ignition, and the disappearance of H_2O_2 and the formation of OH is identified as the second stage ignition. With these chemical properties in mind, at 0.19 ms, low temperature reactions have been initiated at the edge of spray jet. These reactions first occur in leaner mixtures as these are at the highest temperature in the unburnt flow field. Figure 7.21 sub-label (i) shows a minor increase in conditional temperature at 0.19 ms ASI. At 0.30 ms ASI, first stage ignition is underway as indicated by the increase in formaldehyde mass fraction. The low temperature reactions, here coupled with the high scalar dissipation rate in this region, initiate a turbulent cool-flame which transports species and heat release to colder and richer mixtures. This is demonstrated by the shift in conditional temperature (ii), from leaner to richer mixtures. This is also consistent with Figure 7.19, where ignition happens in a lean mixture and the high temperature region expands and penetrates into a more fuel-rich mixture. Second stage ignition is initiated with multiple high temperature points seen over a broad range of rich mixture fractions. The consumption of hydrogen-peroxide at the head of the spray also signifies the onset of second-stage ignition as its decomposition is critical in promoting high temperature reactions. At 0.44 ms the highly stratified flow field, formed from high temperature ignition, initiates turbulent flame propagation (iii) from richer to leaner mixtures. The consumption of formaldehyde and hydrogen-peroxide are clearly seen at the head of the spray. Additionally, the decomposition of H_2O_2 to OH and its associated hot-spots confirm the occurrence of high temperature reactions and volumetric ignition. This follows a previous numerical study of a non-premixed flame, where following a localised autoignition event, the reaction zone will propagate around the kernel [82]. It is also clearly seen that several ignition spots are observed inside the rich mixture region; these spots then expand and finally connect at a later stage. The ignition behaviour and temporal flame structure presented here are consistent with previous experimental studies [104][107][103] and numerical studies [99] [162].

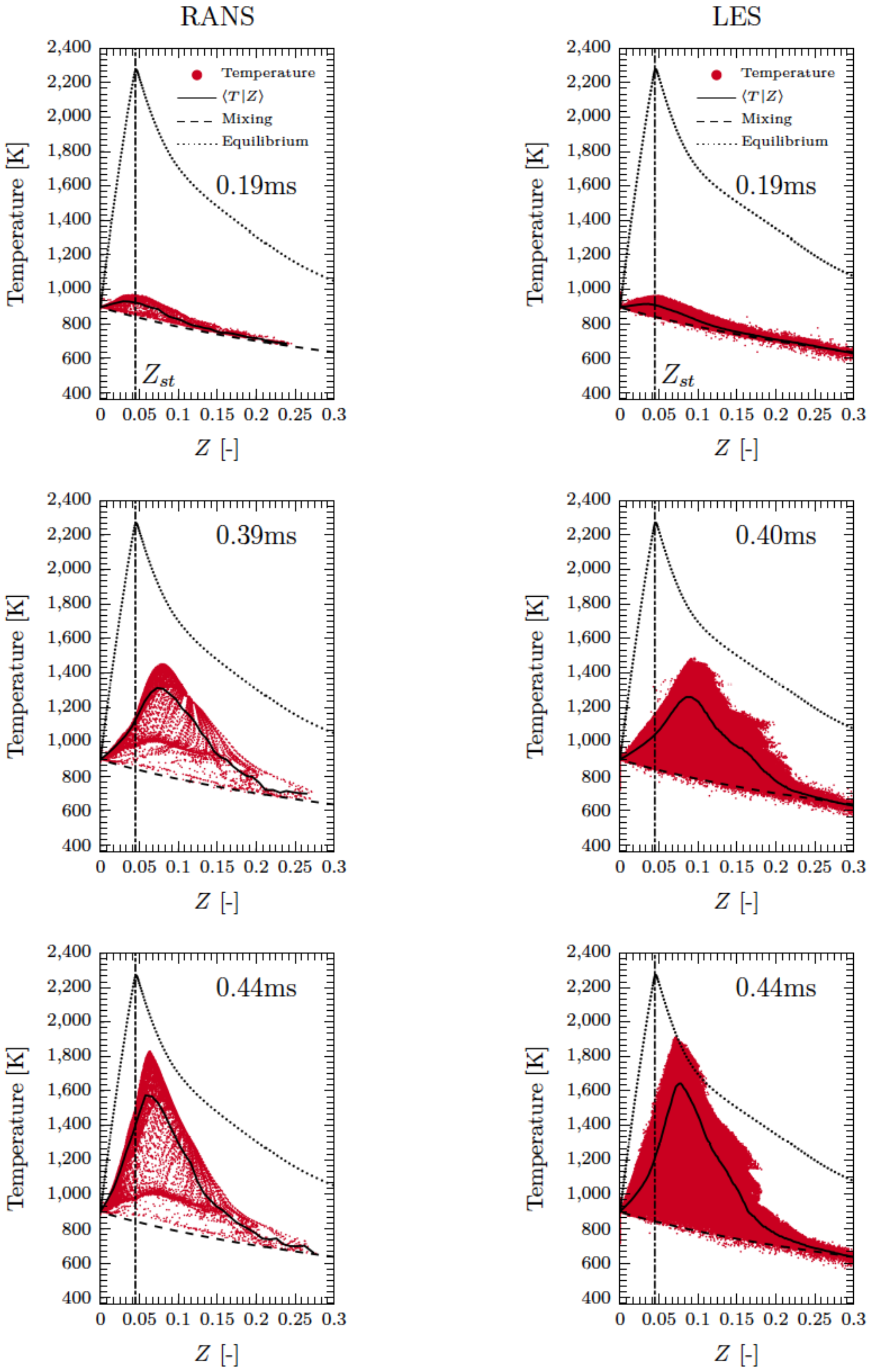

Figure 7.20: Temporal evolution of scatter plot of temperature versus mixture fraction between RANS (left) and LES (right) for the 900K "Spray A" baseline condition.

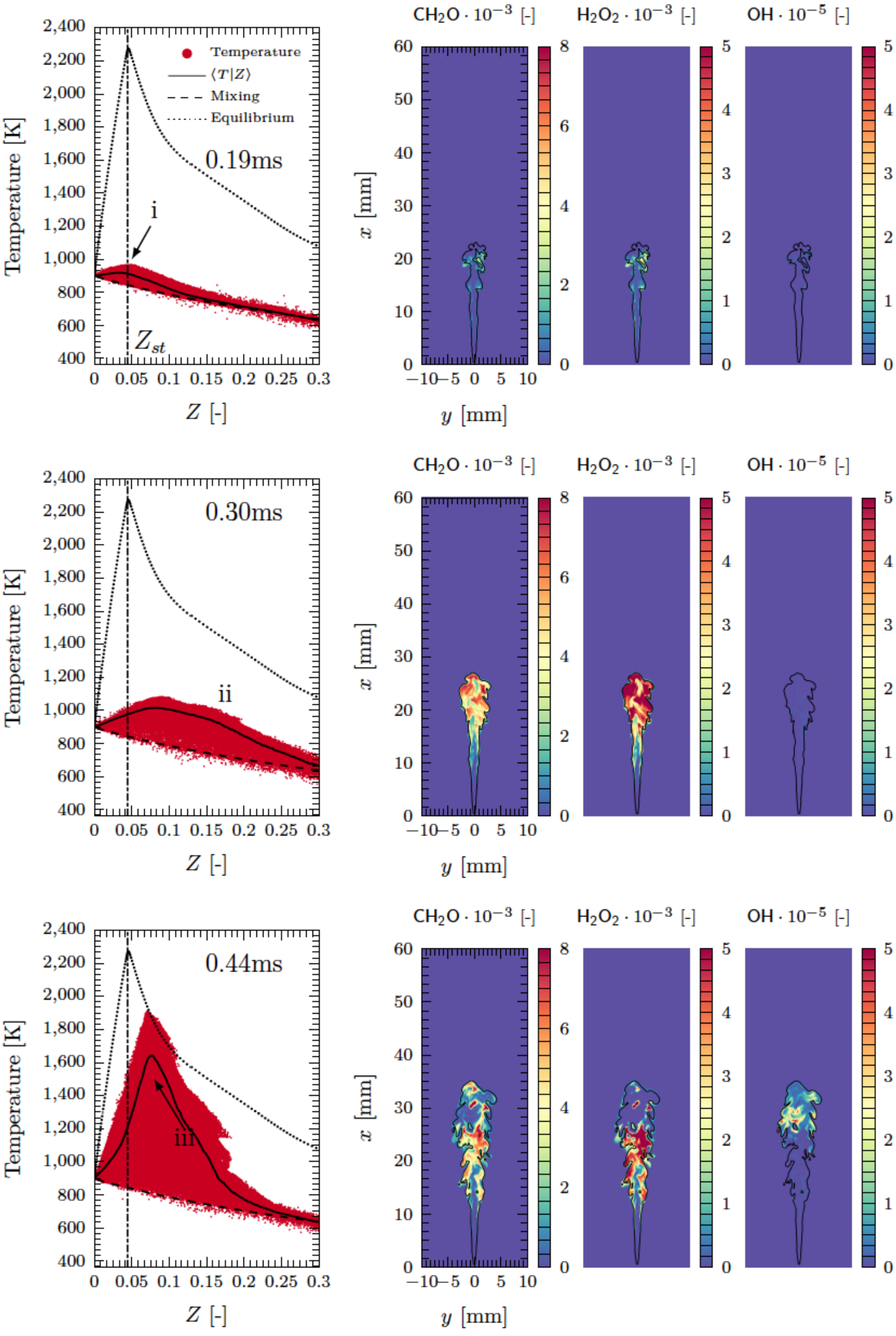

Figure 7.21: Scatter plot in Z-T space with X-Y cut-planes of (1) Formaldehyde, (2) Hydrogen-peroxide and (3) Hydroxyl. The solid black line in cut-planes is the contour of stoichiometric mixture fraction.

While the previous discussion of flame temporal evolution and ignition discussion concentrated only on the analysis of the computational results, it is also possible to compare the simulation results with experimental results. Due to the difficult conditions of this flame, limited experimental information is available. Various diagnostic techniques have been used in different institutions, such as high-speed schlieren, Mie-scattering and chemiluminescence imaging. Despite substantial efforts in experimental studies, only partial sets of data can be provided, with only one or two species available simultaneously. Quantitative experimental measurements of local mixture-fraction, species mass fractions, velocity field and temperature field are not yet possible for reacting conditions. For the study of flame temporal evolution, Figure 7.22 and 7.23 shows comparison between simulations and the experimental schlieren images for the 900 K standard "Spray A" conditions. To aid the visualisation of the high temperature reaction, the border of the high-temperature chemiluminescence (blue line) is overlaid on the simultaneously-acquired schlieren images. The details of image processing and experimental set up can be found in [105]. The ignition delay to high temperature combustion in the experiment is marked by the first combustion luminosity, which appears around 410 μs ASI. Both RANS and LES accurately predicted the ignition event. Second stage ignition region is well matched between the experiments and the simulations. For the flame evolution, even if a quantitative assessment is not possible, the computed distributions from both RANS and LES show a good agreement throughout the evolution of the flame. LES shows a more disperse field compared to RANS. It is worth noting that no ensemble averaged schlieren image is available for this condition therefore ensemble averaged LES comparison is not provided.

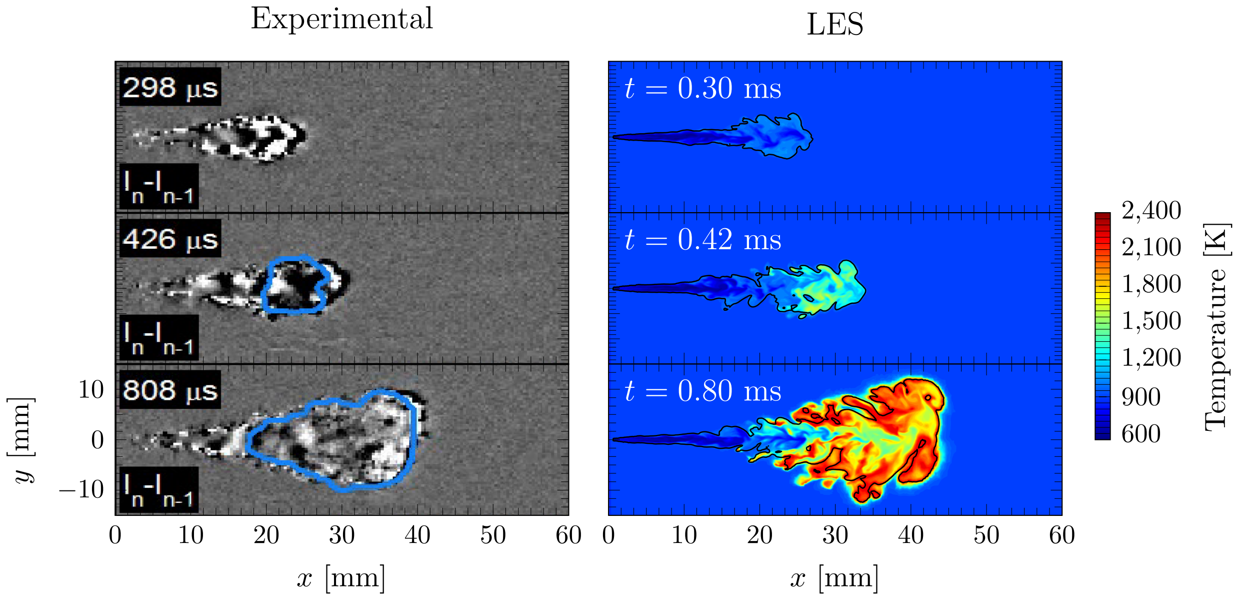

Figure 7.22: Schlieren image (left) and instantaneous temperature fields for single realisation CSE-FGM LES (right) simulations at the 900K "Spray A" baseline condition. The time after start of injection is shown at the top left of image. The blue line in experimental study shows luminosity border. The black line is the stoichiometric mixture fraction contour. The experimental images are corrected by its background intensity (I_n-I_{n-1}).

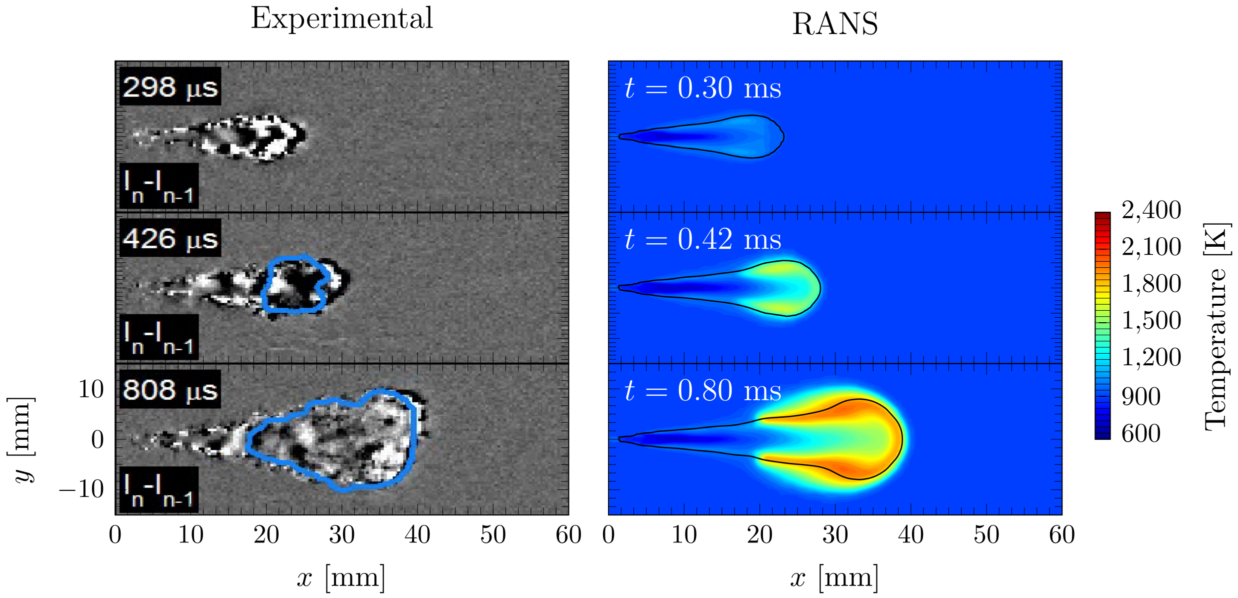

Figure 7.23: Schlieren image (left) and instantaneous temperature fields for CSE-FGM RANS (right) simulations at the 900K "Spray A" baseline condition. The time after start of injection is shown at the top left of image. The blue line in experimental study shows luminosity border. The black line is the stoichiometric mixture fraction contour. The experimental images are corrected by its background intensity (I_n-I_{n-1}).

In order to compare the diesel spray ignition behaviour between the experimental data and the simulation result, the formaldehyde (CH_2O) field is presented. Skeen *et al.* [134] performed simultaneous single-shot planar laser-induced florescence (PLIF) and Schlieren imaging on the 900K "Spray A " baseline condition. Figure 7.24 shows the experimental spatial distribution of formaldehyde (left) from a single injection and a single LES realisation of formaldehyde concentration (right). As the PLIF results from the experiments is qualitative, no quantitative comparisons can be made at this point. Initial formaldehyde formation was observed at the periphery of the penetrating jet, followed by convection to the core. This corresponds to the first stage ignition and heat release. In the CFD simulations, the initial formation of formaldehyde is seen near the periphery of the jet at approximately the same location. This is followed by the penetration of the jet with high concentration CH_2O regions forming due to convection along the centerline of the nozzle. The subsequent consumption of CH_2O corresponds to the main ignition event and the high CH_2O concentration region stabilizes at a certain distance from the nozzle. The CFD model is able to predict the same trend. The high concentration region in simulations is predicted a few millimeters downstream in comparison to the experiments. This is due to the fact that the model is slightly overpredicting the lift-off lengths at this condition and is also subject to variations in multiple realisations. It must be noted that the experiments were carried out for a single injection event. The resolution in the CFD grid is much higher than that of the imaging. In order to have a more consistent comparison between experiments and simulations, an ensemble average over multiple injection is preferable. Due to the unavailability of image resolution, spatial filtering of the LES CH_2O contours was not carried out in this study. The further upstream appearance of formaldehyde can be attributed to the relatively reactive chemical mechanism used in this study, which is consistent with previous chemical mechanism studies performed by Armin *et al.* [159]. Additional experimental studies from Maes *et al.* [80] also reported formaldehyde fluorescence signals up to 10 mm axial position downstream of the injector tip which is the location of the laser sheet. More importantly, a void region is clearly visible at 0.49 ms for both the simulation and experiment giving clear indications of second stage of ignition. This further shows, that the CSE-FGM combustion model is capable of not only capturing ignition delay and flame lift-off length, but that it also describes accurately some of the underlying physical processes in high pressure diesel fuel spray combustion.

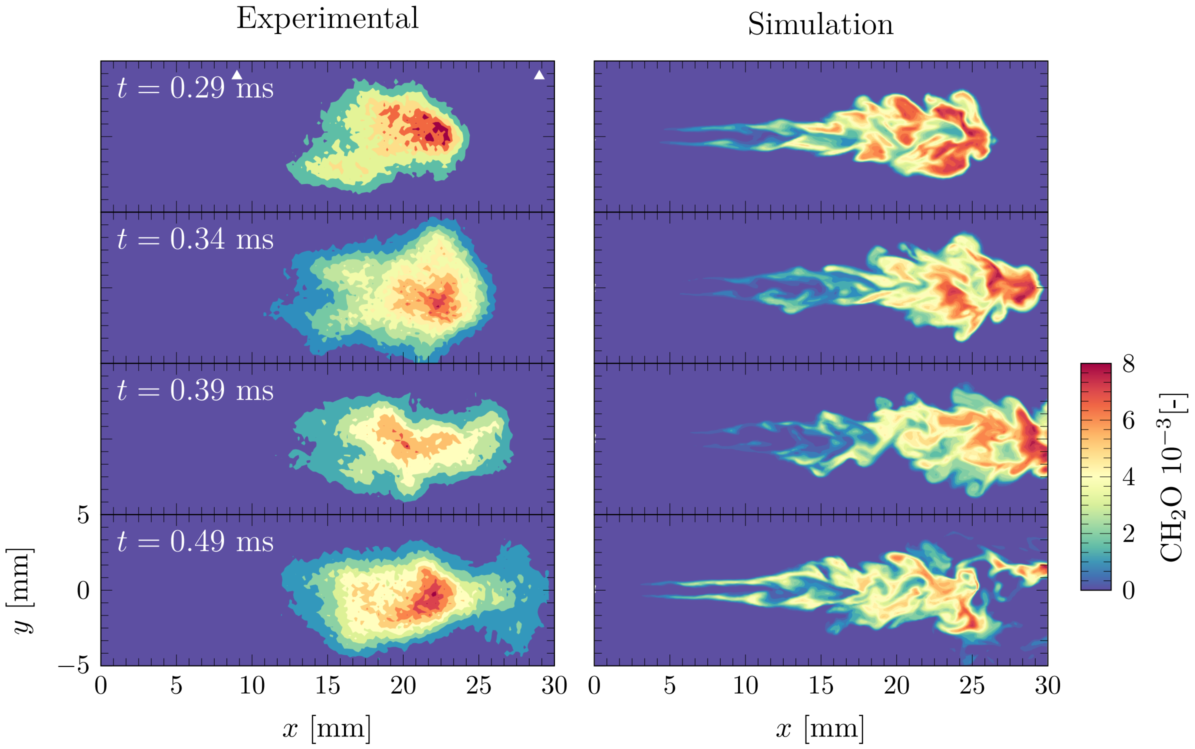

Figure 7.24: Comparison of single injection false color images of formaldehyde PLIF [134] (left) and single realisation LES (right) spatial formaldehyde distribution for the 900K "Spray A" baseline condition at various timings during ignition. White mark indicates the laser sheet. The colour bar in this figure only applies to the LES simulation as there is no quantitative data from experiments.

7.6.2 Realisation Variations

Following the study of the transient spray ignition processes, the variation with different LES realizations, ensemble-average of 5 realizations, and RANS predictions are presented to qualitatively study the differences between the LES and RANS models, and also to quantify the differences between LES realizations. Figure 7.25 presents a comparison of mixture fractions and temperature fields between different LES realizations, ensemble-averaged 5 LES realizations, and RANS predictions at 0.7

ms for the 900 K “Spray A” baseline condition. The RANS contour clearly presents a smoother flame structure with axis-symmetric features for both mixture fraction and temperature. The single realisation prediction of LES shows a completely asymmetric structure where substantial fluctuations are present between realisations. The ensemble average of 5 LES realizations shows a much smoother contour like RANS. It is also worth noting that for the ensemble averaged LES simulations, the Z_{st} line crosses is closer to the jet centerline overlapping more of the high temperature region compared to single LES simulation realisation. This is close to the behaviour of the RANS simulation. However, the distribution of the temperature is still quite different when comparing the ensemble-averaged LES with RANS. Ensemble averaged LES results show a higher temperature region around 40 mm downstream, away from the spray axis, and relatively low-temperature regions around the flame lift-off region and the leading flame region close to the spray axis. The predictions of RANS present similar temperature magnitude along the stoichiometric mixture fraction line. However, it should be noted that the jet penetration is different for the RANS and LES predictions, which will have some influence on the flame locations and temperature distributions. The realization variation was also examined in the mixture fraction space and only a very subtle difference was observed, therefore it not shown here. Although RANS CSE-FGM is capable of observing global flame characteristics, the mixing field is better resolved with the LES calculations, therefore predictions are expected to be both quantitatively and qualitatively better than RANS. With this in mind, the further study of the flame stabilization mechanism will be focused using the CSE/LES simulations.

7.6.3 Flame Stabilisation

The presence of high convection and diffusion in a transient diesel spray flame has raised various questions about the flame stabilization mechanisms. Figure 7.26 highlights the main characteristics of a typical stabilized spray flame and their visual definition. Available numerical simulations and experimental data have suggested autoignition events upstream of (or near) the lift-off length play a significant role in

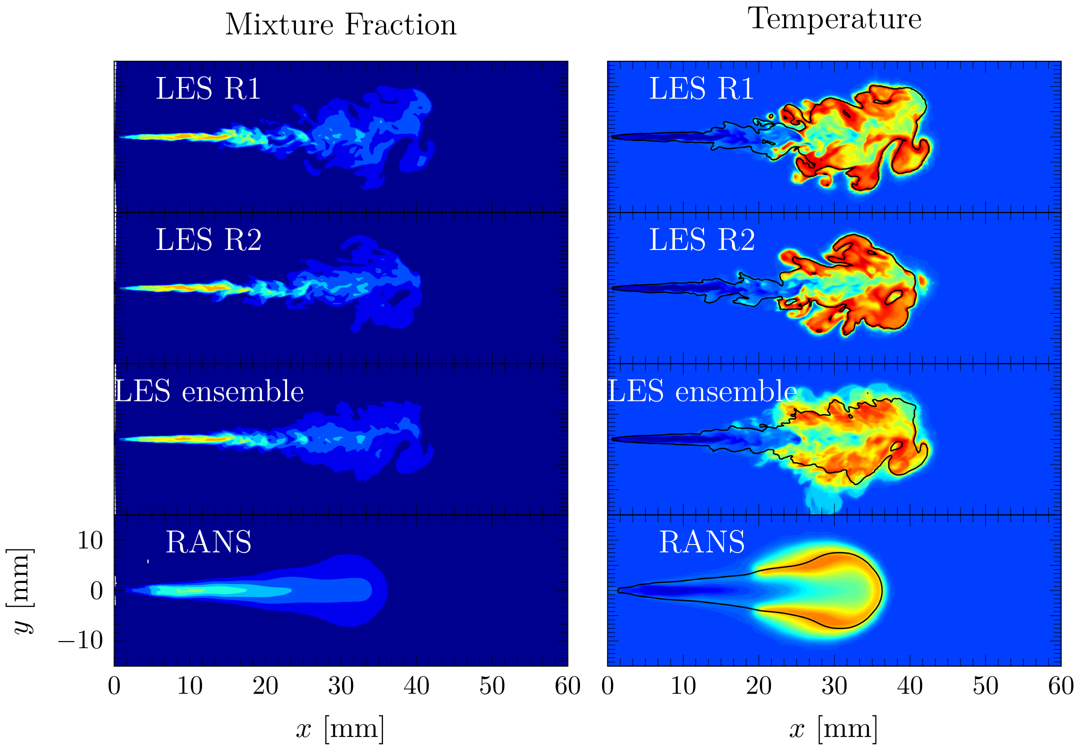

Figure 7.25: Realization variation, ensemble average of 5 LES calculations and RANS results of mixture fraction field (left) and temperature field (right) at 0.7ms for the 900K "Spray A " baseline condition. The black line is the stoichiometric mixture fraction contour . Mixture fraction and Temperature contour colour schemes are the same as Figure 7.17 and Figure 7.18.

flame stabilization [133][106][99][90]. Therefore, it is critical to have an accurate prediction of flame lift-off length, hence capturing the underlying flame stabilization mechanism. As mentioned before, experimental flame lift-off length is given by the OH* chemiluminescence; in contrast, the CFD flame lift-off is provided by the OH concentration. More recently, Maes *et al.* [80] performed experimental measurements using planar laser-induced fluorescence (PLIF) of ground state OH at various ECN "Spray A" conditions giving the opportunity for direct qualitative comparison between experimental and simulation lift-off length. For the experimental study, ensemble averaged images of 5-20 injections depending on the test condition were obtained. The experimental setup and measurement technique were discussed in detail in [80]. Figure 7.27 compares the simulated ground state OH mass fraction with the measured ensemble averages OH-PLIF results. The white arrows in the figure indicate the approximate limits of the laser sheet. It is worth noting that the

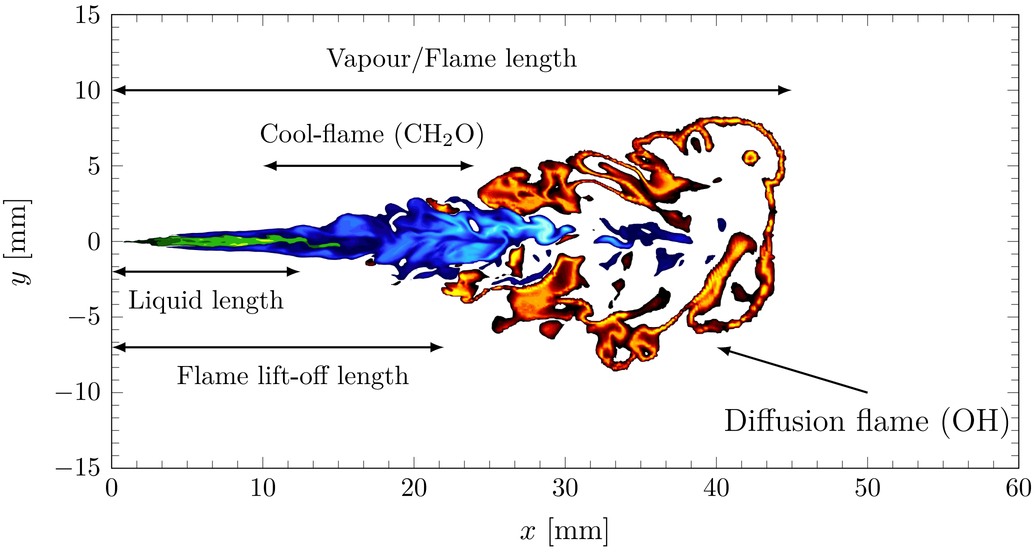

Figure 7.26: Schematic of a stabilized spray flame: green is the n-dodecane fuel, blue is the cool-flame and is defined by presence of formaldehyde and orange is the high temperature diffusion flame which is defined by the presence of hydroxyl.

less bright OH branch on the right for the experimental data is attributed to the attenuation of the excitation laser light by the spray. The simulation well captured the OH field, as shown by the two distinct branches of OH where each branch expands in the radial direction as the axial distance is increased. In addition, the onset of OH is comparable between simulation and experiment at approximately $x = 15$ mm. However, the simulation predicts higher concentrations of OH further downstream compared to the experiment. This is likely to be caused by the experimental measurement technique as the laser sheet intensity distribution used in the experiment is known to improve the represented signal at near lift-off location.

As mentioned before, the LES simulations suggested a quasi steady-state flame is established around 0.7 ms ASI, which is consistent with the experiment where more coherent images are observed after 0.7 ms [80]. Therefore, for the comparison of quasi steady-state flame structure, the OH distribution at 1.2 ms ASI is compared to the 4.7 ms OH PLIF measurements. The simulation is again qualitatively comparable to the experiment with two branches expanding in both radial and axial directions. However, the onset location of OH is underpredicted at this time instance as well as the OH field being more diffuse than the separate OH

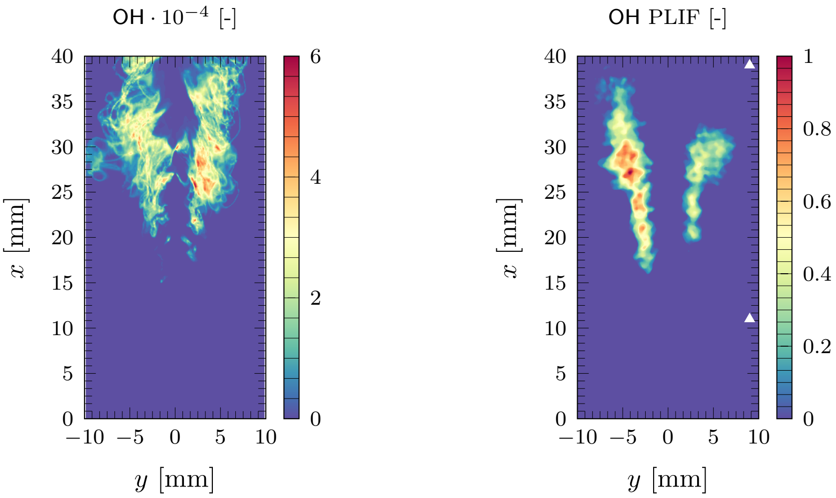

Figure 7.27: Comparison of (a) CSE-FGM/LES spatially averaged OH mass fraction and (b) ensemble-averaged experimental PLIF OH measurements at 0.8 ms ASI. Laser sheet location is marked by white triangles. Experimental data repeated from [80].

branches seen in the experiment. This could be attributed to the experimental methodology, where it can be seen from [80] that differences in optical setup resulted in qualitatively different OH distributions at the same test condition. These differences are shown in Figure 7.29, where the OH structure as measured by IFP Energies nouvelles (IFPEn) is considerably more diffuse than that of Eindhoven University of Technology (TU/e). In general, the typically observed spray structure has a fuel rich core enveloped by a high temperature field as indicated by the presence of OH. The onset presence of OH (18.94 mm) is also reported in the experiment approximately 1.55 mm downstream of the onset OH* (17.39 mm). This is an important consideration as it will influence confidence in the CFD flame lift-off length in that the threshold may not be a suitable enough criteria to make absolute comparisons against experimental measurements based on OH.

Previously, Pet *et al.* investigated the effect of implied convection, diffusion, and reaction terms on stabilization mechanisms [99]. The study suggested the diesel spray stabilization mechanism can be perceived as autoignition controlled but modulated by flame propagation. This indicates flame lift-off length is regulated by the axial distance at which flow conditions do not support the formation and growth of ignition kernels. Scalar dissipation rate measures the mixing rate of fuel

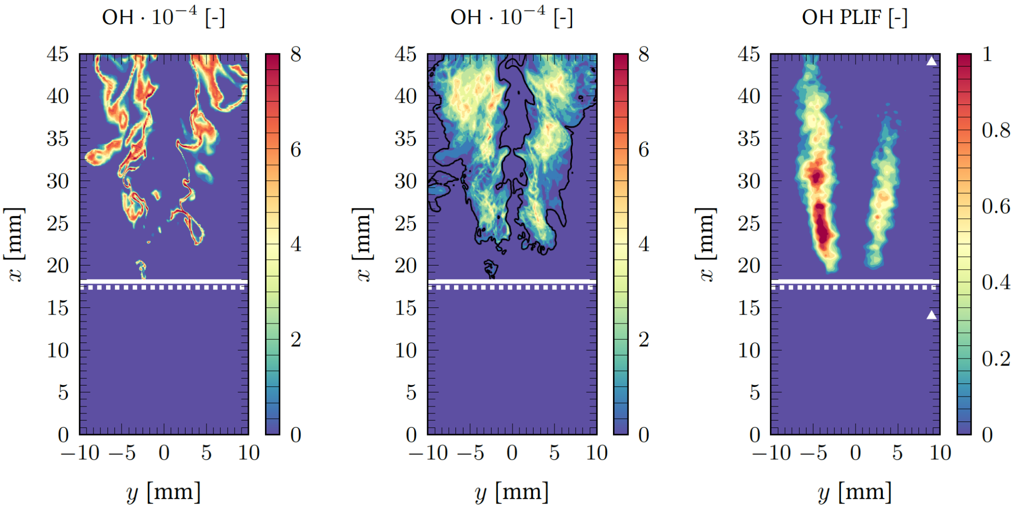

(a) (b) (c)

Figure 7.28: Comparison of (a) CSE-FGM/LES instantaneous OH mass fraction field at 1.20 ms ASI, (b) spatially-averaged CSE-FGM/LES OH mass fraction field at 1.20 ms ASI, (c) ensemble-averaged OH PLIF measurements at 4.70 ms ASI. The white solid line denotes CSE-FGM/LES flame lift-off value, the white dashed line denotes steady-state experimental flame lift-off value (based on OH) from Maes *et al.* [80]. Laser sheet location marked by white triangles. Experimental images reproduced from [80]

and oxidizer, which significantly impact the flow field, and therefore has a strong influence on the autoignition and flame structure. The filtered scalar dissipation rate $\tilde{\chi}$ in LES can be decomposed into resolved ($\tilde{\chi}_r$) and the subgrid part ($\tilde{\chi}_{sgs}$) is given by Tillou *et al.* [145]:

$$\tilde{\chi} = \tilde{\chi}_{sgs} + \tilde{\chi}_r = 2D\left|\frac{\partial \tilde{Z}}{\partial x}\right|^2 + \frac{D_t}{\Delta^2}\widetilde{Z''^2} \tag{7.15}$$

Where D is the molecular diffusivity of the mixture, D_t is the turbulent diffusivity, and Δ is the grid size. The process of flame stabilization can be visualised by tracking an ignition kernel near the flame lift-off length. Figure 7.30 focuses on the temperature and scalar dissipation rate evolution near the flame lift-off location for the CSE-FGM/LES model at quasi steady-state (around 1 ms ASI). Large fluctuations in the scalar field indicate the highly unsteady nature of the diesel spray jet. Low and high scalar dissipation rates are seen to evolve within the flame structure. At 0.95 ms, one can notice that there is an ignition spot upstream of

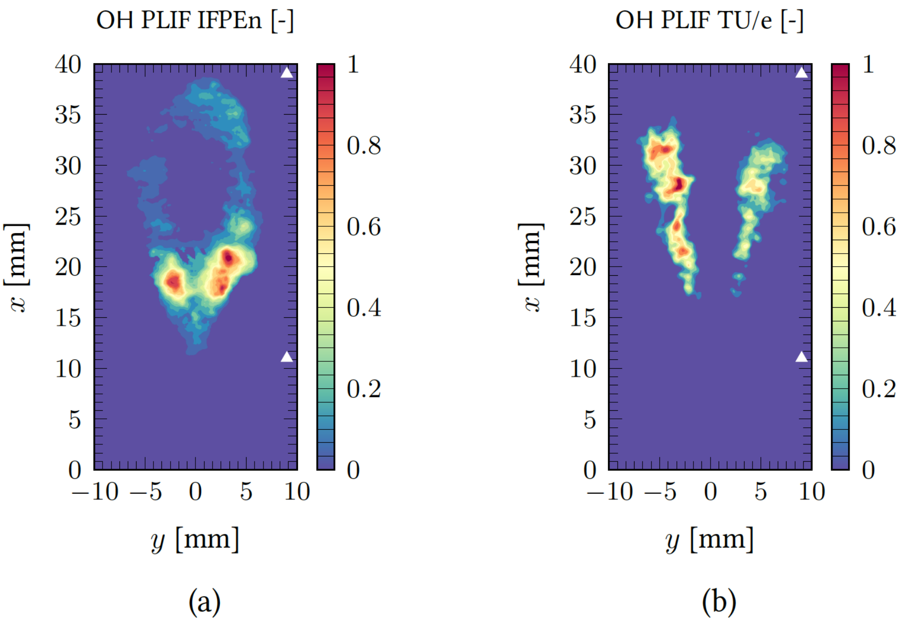

(a) (b)

Figure 7.29: Comparison of ensemble-averaged experimental PLIF OH measurements at 0.7 ms ASI for (a) IFPEn and (b) TU/e. Laser sheet location is marked by white triangles. Experimental images reproduced from [80].

the flame (marked by (i)). Figure 7.31 provides the radial profiles of termperature and scalar dissipation rate at this location. This indicates that the ignition is indeed occurring in regions of low scalar dissipation rate. Further tracking of the ignition spot from 0.95 ms to 0.99 ms shows its expansion and connection to the main flame. The ignition spot moves further downstream driven by convection, which merges with other gas pockets and finally the main flame (iv) at 1.02 ms ASI. In addition to ignition taking place, extinction also occurs in this flame. This is observed by tracking an ignited gas pocket denoted by sub-label (A) at 0.95 ms ASI in Figure 7.30. The radial profiles of temperature and scalar dissipation at this point (Figure 7.32) show similar behaviour to that seen in Figure 7.31. However, at 0.97 ms ASI, convection of the vapour jet upstream leads to large scalar gradients in the region around point (A) and local extinction of the flame occurs as highlighted by (B). The observation obtained here suggests that diesel spray flame stabilization can be controlled by autoignition.

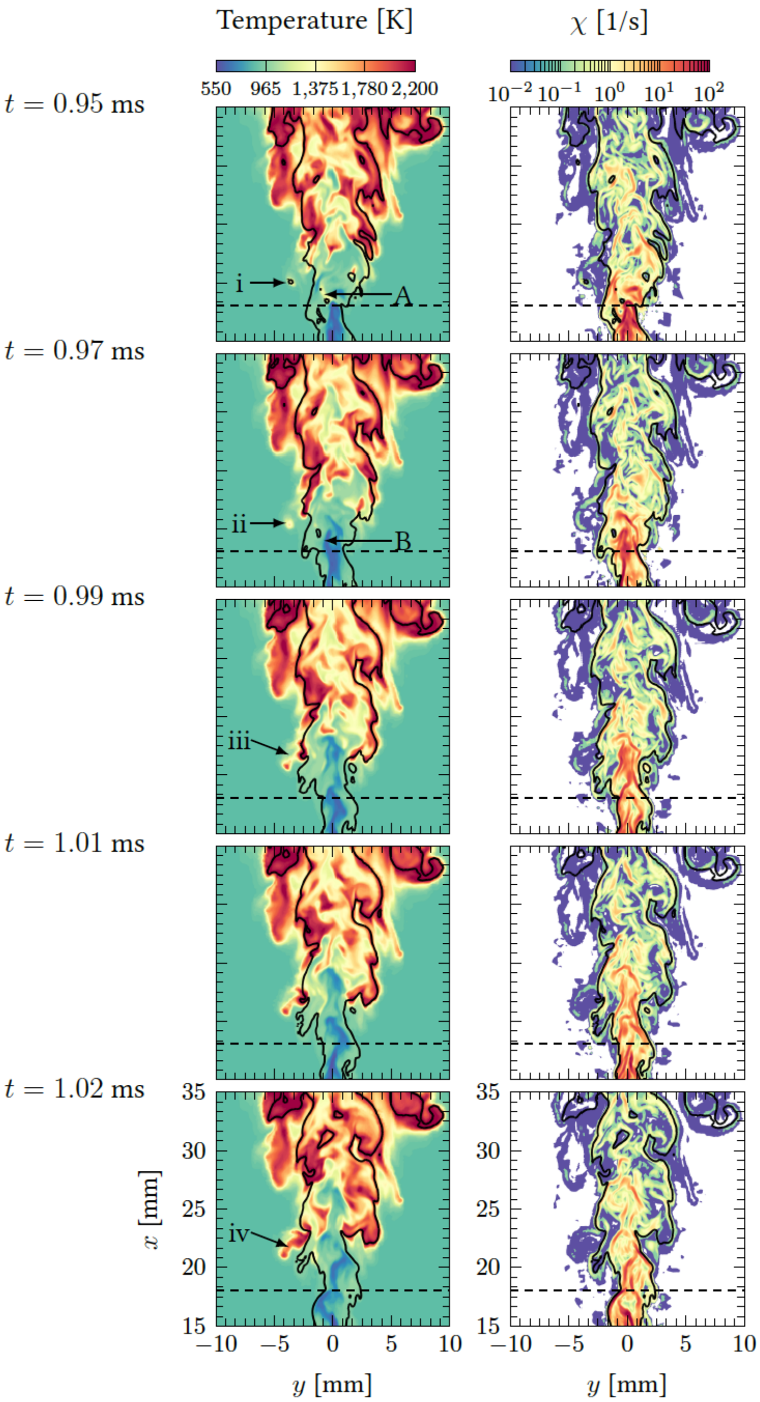

Figure 7.30: Temperature (left) and scalar dissipation (right) evolution near the flame lift-off length. The black dashed line marks the simulations flame lift-off length. The solid black line is the contour of stoichiometric mixture fraction.

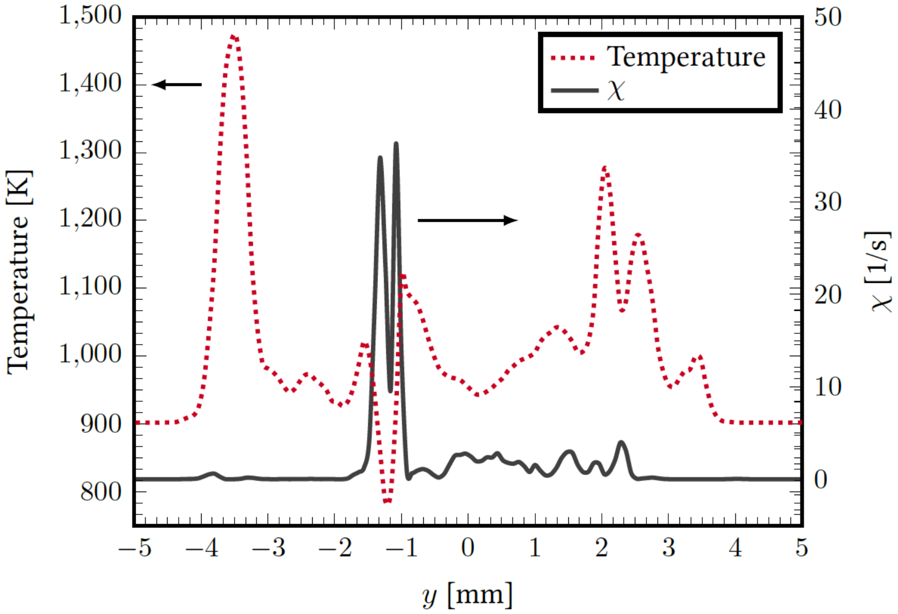

Figure 7.31: Radial scalar dissipation at 0.95 ms ASI at point (i) in Figure 7.30

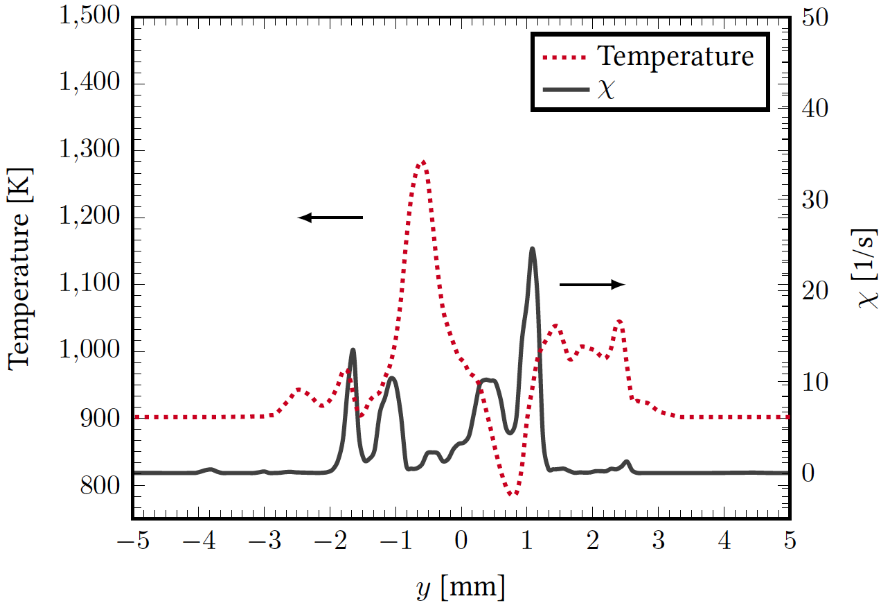

Figure 7.32: Radial scalar dissipation at 0.95 ms ASI at point (A) in Figure 7.30

7.7 Summary

In this chapter a novel combustion modelling approach (CSE-FGM) was presented and validated against diesel spray flame experiments with both RANS and LES frameworks. The approach combines the conditional moment hypothesis with a tabulated chemistry given by the unsteady flamelet generated manifold. This approach enables the combustion model, conditional source-term estimation, to be extended to a more complicated fuel. Extensive validation of the CSE-FGM was carried out for the 900 K ECN “Spray A” conditions with a 54 species 268 reactions n-dodecane chemical mechanism covering the low temperature combustion region for the diesel fuel surrogate. The findings are summarized in the following:

- The CSE-FGM based combustion modelling approach has successfully demonstrated the capability of realistically predicting the essential structure of the diesel-fueled transient spray combustion processes. The unique structure of spray jet flame consisting of liquid fuel jet, a low temperature oxidation zone, and a high oxidation zone can be well captured.

- Both RANS and LES are capable of quantitatively predicting the autoignition time and flame lift-off length with slight overprediction in RANS simulations.

- The LES simulation suggest two stage ignition is indeed captured by the CSE-FGM combustion model. In LES, multiple ignition kernels were found in the mixing layer compared to only one location shown in RANS predictions. The LES temperature field showed reasonably good agreement with the experimental schlieren images in terms of the location and size of the flame propagation.

- The comparison of the simulated formaldehyde field with experiments showed that the major formaldehyde occurrence prior to ignition is observed at the tip of the fuel-rich gas jet. Second stage ignition is well captured by the consumption of formaldehyde near the time of autoignition.

- Analysis of the flame stabilization mechanism showed good agreement for the OH field compared to experiments. Both autoignition and local extinction were found near the flame lift-off length which suggests the flame stabilization is controlled by autoignition but modulated by flame propagation

From a combustion modelling viewpoint it can be argued that CSE-FGM offers a feasible tool for detailed combustion analysis of diesel spray flames. Both RANS and LES can provide reasonably good global predictions of the flame. The LES simulation requires more computational power compared to the RANS simulation. In this study, each 1.5 ms reacting LES realisation requires 3420 core hours on an Intel Xeon (2017, E5-2680V3, 2.5GHz) processor, while a RANS simulation under the same conditions only 53 core hours is needed. The LES approach is more data-rich given the opportunity to explore more local and unsteady phenomenon present in a transient diesel jet. Overall the computationally more expensive LES simulations were shown to better represent the experimental data available to date.

Imagination is more important than knowledge. Knowledge is limited. Imagination encircles the world.

— Albert Einstein

8

Conclusions

Contents

8.1 Conclusions

The objective of this study was to cover several questions with regard to the understanding of diesel fuel spray combustion modelling. Some key diesel spray physical phenomenon is explored in particular - combustion recession at the end of diesel spray injection was studied in details. The engine combustion network defined "Spray A" conditions were explored for the study of engine relevant diesel spray combustion. First, the effect of the grid resolution in high-velocity fuel spray and the sensitivity of different physical models to integral spray quantities and mixture formation is investigated in a RANS context. The mesh resolution requirements for the present "Spray A" case was shown. A minimum cell size of 0.25 mm was required for a converged simulation. The applicability and influence of break-up, collision, turbulence models traditionally used in RANS simulations have been explored. The numerical results showed that the induced gas jet and the local mixture formation, after the liquid fuel has been evaporated, was best represented using KH-RT break-up model, $k - \epsilon$ turbulence model with modified constants and NTC collision model.

For the study of combustion recession, different combustion models were explored in order to better predict combustion recession under the RANS framework. All models were interfaced with a well-established commercial three-dimensional flow field solver, an approach which allows for the inclusion of detailed chemistry in the simulation of turbulent reacting flows at a reasonable computational cost. The ability to include detailed chemistry forms the basis for quantitative pollutant formation predictions, although pollutant predictions are outside the current project scope. As coupled models are applied to investigate auto-igniting liquid fuel sprays, detailed chemistry is, however, a prerequisite for the accurate description of the ignition processes. The performance and validity of the method employed were tested on the one hand by investigating the influence of air temperature on ignition delay at diesel engine relevant conditions, for which experimental data from a high pressure and temperature open combustion chamber has been reported. Numerical results are further compared with experimental data gathered from an optically accessible, constant-volume, closed, high-temperature, high-pressure chamber, for which the comprehensive set of validation data comprises liquid and gas phase spray penetration, ignition delay and location, as well as a pressure signal, indicative of the combustion, generated heat release. Furthermore, with respect to the physical mechanisms concerning the interaction between the turbulent flow field and the flame, the study sought to develop a deeper understanding and identification of the governing parameters and processes in this modelling approach relating to the turbulence-chemistry interaction. First, a flamelet generated manifold method developed by Wehrfrit *et al.* [159] was implemented in CONVERGE solver. The findings regarding FGM for the prediction of diesel spray include:

- Reactive simulations using the FGM model and two combustion models available in CONVERGE, the well-stirred SAGE model and the RIF model show overprediction in the ignition delay time and flame lift-off length for both the SAGE and RIF models. The FGM model underpredicted the ignition delay time but gave the best prediction for flame lift-off length. Combustion recession was predicted by all three models with the RIF and FGM models being able to better capture individual pockets of OH inline with experimental observations.

- The FGM model performance was further examined using two different chemical kinetics mechanisms for n-Dodecane, the Cai mechanism [20] with 57 species and 197 reactions and the Yao mechanism [166] with 54 species and 268 reactions, over different ambient temperature conditions. For low temperature conditions, 800 K, the Yao mechanism overpredicted both IDT and LOL whereas the Cai mechanism predicted autoignition but underpredicted the IDT while closely matching the flame LOL. Combustion recession was not captured according to the Cai mechanism at 800 K, which is consistent with the previous modelling works using both the SAGE and RIF models as well as the available experimental data.

- Both mechanisms captured the IDT and flame LOL with acceptable accuracy at the higher ambient temperatures of 900 K and 1000 K, with the Cai mechanism slightly underpredicting the IDT and the Yao mechanism slightly overpredicting the IDT. These minor differences can be explained by the differences in species manifolds for these two chemical mechanisms. In terms of combustion recession, both mechanisms were able to capture the second stage ignition required for this transient phenomenon in the FGM model, whereas the SAGE and RIF models were not able to capture second stage ignition using the Yao mechanism. The Yao mechanism was able to predict combustion recession further upstream towards the near nozzle region. Both mechanisms show clear signs of separated ignition pockets through OH mass fraction plots along the spray centerline. In general, the study shows that the tabulated chemistry FGM model is able to capture similar trends of combustion recession to those shown in the experimental data available in the literature.

The results of this work also indicated that low temperature reaction mechanisms play a significant role in predicting the likelihood of second-stage ignition and combustion recession events near the injector nozzle region. Because of the nature of FGM type combustion model, it is possible to explore the more complicated chemical mechanism. Therefore additional studies were performed to elucidate further the effects of different chemical mechanisms for n-Dodecane – including the reduced chemical mechanism from Ranzi *et al.* [116] (130 species and 2395 reactions referred to as to the Polimi mechanism) – in the prediction of combustion recession was performed. Multidimensional reactive spray simulations were performed using both an FGM model based on the homogeneous reactor tabulation method and a newly implemented FGM model, based on the igniting counterflow diffusion flame tabulation method, using the CONVERGE CFD solver. The effect of the tabulation method on reactive spray prediction and the efficacy in predicting combustion recession by each chemical mechanism under an FGM framework follows:

- The study of tabulation method showed that both the HR and the ICDF methods are capable of qualitatively capturing the flame structure at steady-state. However, higher source terms were found for the HR case, which leads to shorter ignition delay and LOL than the ICDF approach. Higher temperature contours were also found in the HR approach when compared to the ICDF approach owing to the exclusion of diffusion and transport phenomenon during a reaction. The lack of strain effects in diffusion flame also resulted in the failure of the HR FGM approach to predict combustion recession. This indicates the significant role that diffusion processes still play in flame predictions, and particularly on the end of injection processes such as combustion recession, even at the very high temperature and pressure conditions typical of diesel engine combustion. It was concluded, therefore, that in order to capture the end of injection transient phenomenon in diesel sprays, the ICDF tabulation approach for the FGM model is more appropriate than the HR approach.

- The differences in the progress variable source term retrieved from the manifold of each mechanism resulted in slight differences of flame stabilisation locations which effected the LOL predictions. The IDT analysis from the 3D simulations showed similar results to the 1D flamelet results, which indicates that chemical kinetics is one of the driving factors for the predictions of IDT in the FGM approach. Both the Cai mechanism and the Polimi mechanism show good predictability in IDT and LOL. With a higher chemical source term in the ignition region, the Yao mechanism predicted earlier IDT and shorter LOL. Whereas the Luo mechanism consistently overestimated the IDT and LOL due to lower chemical source term values presented in the manifold throughout all regions.
- Low-temperature chemistry is a driving force for second-stage ignition in diesel spray end-of-injection processes. Clear evidence was found through the comparison of OH quantities obtained from the Cai mechanism and the Luo mechanism. Originated from the same detailed chemistry, the Cai mechanism presented a stronger prediction for combustion recession due to its better incorporation of low-temperature chemistry. In the current FGM framework, the Yao mechanism predicted the furthest combustion recession phenomenon due to its higher chemical source term in ignition regions which agrees with prior experimental observations showing combustion recession is driven by a series of auto-ignition events.

Although this study has given increased physical insights for the prediction of combustion recession using the FGM approach, there is still room for improvement in terms of the combustion model. The inclusion of $\widetilde{Z''^2}$ in the tabulation process which, as highlighted by previous studies, could increase the diffusion processes in near nozzle regions creating a stronger entertainment flux resulting in further combustion recession. Therefore, a state of the art combustion model based on conditional source-term estimation has been coupled with flamelet generated manifold for diesel chemistry, therefore predict the highly transient nature of diesel fuel spray combustion. The newly implemented combustion model was verified extensively showing good predictability for the transient diesel spray flame:

- The CSE-FGM based combustion modelling approach has successfully demonstrated the capability of realistically predicting the essential structure of the diesel-fueled transient spray combustion processes. The unique structure of spray jet flame consisting of liquid fuel jet, a low-temperature oxidation zone, and a high oxidation zone can be well captured.

- Both RANS and LES are capable of quantitatively predict the autoignition time and flame lift-off length with slight overprediction in RANS simulations.

- The LES simulation suggest two-stage ignition is indeed captured by the CSE-FGM combustion model. In LES multiple ignition kernels were found in the mixing layer compared to only one location shown in RANS predictions. The LES temperature field showed reasonably good agreement with the experimental schlieren images in terms of the location and size of the flame propagation.

- The comparison of the simulated formaldehyde field with experiments showed that the major formaldehyde occurrence prior to ignition is observed at the tip of the fuel-rich gas jet. Second stage ignition is well captured by the consumption of formaldehyde near the time of autoignition.

- Analysis of the flame stabilisation mechanism showed good agreement for the OH field compared to experiments. Both autoignition and local extinction were found near the flame lift-off length, which suggests the flame stabilisation is controlled by autoignition but modulated by flame propagation

8.2 Future Work

The future work developed from this study should focus on the further development of the combustion model. The present study showed that the CSE-FGM approach was able to capture and to accurately predict key characteristics of a transient diesel spray jet. For the current combustion model, future work should include:

- Testing different methods of inversion and regularisation for future studies. As the conditional average given by the CSE routine is very sensitive to the numerical process. Different inversion and regularisation methods can be used to improve both the accuracy and efficiency of the CSE routine. Recent studies from Hong *et al.* [147] used an iterative solver which reduced computational times by order of magnitude during the inversion phase of CSE in comparison with the conventional LU-decomposition method.

- An investigation of progress variable composition. As mentioned before, one of the difficulties of using CSE is the need for generating and parametrising the low-dimensional manifolds. This is particularly challenging for complicated hydrocarbon fuels such as n-dodecane and n-heptane. In the present study, the manifold is gathered using FGM, which parametrised by the reaction progress and mixture fraction. The progress variable is defined in a combination of representative species which may not be optimal for all stages of flame ignition, flame evolution and flame stabilisation. One alternative way to gather a more sophisticated parametrisation variable is through statistical methods, for example, principal component analysis (PCA), artificial neural networks (ANNS). The tabulation of combustion chemistry through systematically defined progress variable could lead to a more accurate representation of the chemical process using manifold [38][141].

- Doubly conditioning. A recent study from Bushe [17] suggests that when sufficient conditional variables are provided, the spatial variations in the conditional averages can be ignored. Therefore the inclusion of a second conditioning variable can also be investigated, strengthening the application of CSE.

References

[1] B. Abramzon and W. Sirignano. Droplet vaporization model for spray combustion calculations. *International Journal of Heat and Mass Transfer*, 32(9):1605 – 1618, 1989.

[2] R. Aglave, U. Riedel, and J. Warnatz. Turbulence-chemistry interactions in CFD modelling of diesel engines. *Combustion Theory and Modelling*, 12(2):305–325, 2008.

[3] M. M. Ameen, Y. Pei, and S. Som. Computing statistical averages from large eddy simulation of spray flames. *SAE Technical Paper, 2016-01-0585*, 1, 2016.

[4] S. Asenbauer. *Examining Spray Models for Conditional Source-term Estimation Combustion Simulation.* PhD thesis, University of British Columbia, 2015.

[5] H. Barths, C. Hasse, G. Bikas, and N. Peters. Simulation of combustion in direct injection diesel engines using a eulerian particle flamelet model. *Proceedings of the Combustion Institute*, 28(1):1161 – 1168, 2000.

[6] J. C. Beale and R. D. Reitz. Modeling spray atomization with the Kelvin-Helmholtz/Rayleigh-Taylor hybrid model. *Atomization and Sprays*, 9(6), 1999.

[7] P. Beard, J.-M. Duclos, C. Habchi, G. Bruneaux, K. Mokaddem, and T. Baritaud. Extension of lagrangian-eulerian spray modeling: Application to high pressure evaporating diesel sprays. *SAE Technical Paper, 2000-01-1893*, 06, 2000.

[8] C. Bekdemir, E. Rijk, L. Somers, P. Goey, and B. Albrecht. On the application of the flamelet generated manifold (FGM) approach to the simulation of an igniting diesel spray. *SAE Technical Papers, 2010-01-0358*, 04, 2010.

[9] A. Berlemont, M. S. Grancher, and G. Gouesbet. On the lagrangian simulation of turbulence influence on droplet evaporation. *International Journal of Heat and Mass Transfer*, 34(11):2805 – 2812, 1991.

[10] R. Bilger, S. Starner, and R. Kee. On reduced mechanisms for methane air combustion in nonpremixed flames. *Combustion and Flame*, 80(2):135 – 149, 1990.

[11] R. W. Bilger. Conditional moment closure for turbulent reacting flow. *Physics of Fluids A: Fluid Dynamics*, 5(2):436–444, 1993.

[12] M. K. Bobba, C. L. Genzale, and M. P. B. Musculus. Effect of ignition delay on in-cylinder soot characteristics of a heavy duty diesel engine operating at low temperature conditions. *SAE Int. J. Engines 2009-01-0946*, 2:911–924, 04 2009.

[13] G. Borghesi, E. Mastorakos, and R. S. Cant. Complex chemistry DNS of n-heptane spray autoignition at high pressure and intermediate temperature conditions . *Combustion and Flame*, 160(7):1254 – 1275, 2013.

[14] G. Borghesi, E. Mastorakos, C. B. Devaud, and R. W. Bilger. Modeling evaporation effects in conditional moment closure for spray autoignition. *Combustion Theory and Modelling*, 15(5):725–752, 2011.

[15] R. Borghi. Computational studies of turbulent flows with chemical reaction. *Murthy S.N.B. (eds) Turbulent Mixing in Nonreactive and Reactive Flows.*

[16] K. Bray. The challenge of turbulent combustion. *Symposium (International) on Combustion*, 26:1–26, 1996.

[17] W. K. Bushe. Spatial gradients of conditional averages in turbulent flames. *Combustion and Flame*, 192:314 – 339, 2018.

[18] W. K. Bushe and H. Steiner. Conditional moment closure for large eddy simulation of nonpremixed turbulent reacting flows. *Physics of Fluids*, 11(7):1896–1906, 1999.

[19] S. C. Blomberg, L. Zeugin and M. Bolla. Modeling Split Injections of ECN “Spray A” Using a Conditional Moment Closure Combustion Model with RANS and LES. *SAE Int. J. Engines 2016-01-2237*, 9(4), 01 2016.

[20] L. Cai, L. Kroger, and H. Pitsch. Reduced and optimzed mechanism for n-dodecane oxidation. *15th International Conference on Numerical Combustion*, 04, 2015.

[21] C. M. Cha, G. Kosaly, and H. Pitsch. Modeling extinction and reignition in turbulent nonpremixed combustion using a doubly-conditional moment closure approach. *Physics of Fluids*, 13(12), 2001.

[22] Chem1D. One-dimensional laminar flame code, Eindhoven University of Technology. *URL http://www. combustion. tue. nl/chem1d.*

[23] R. Clift, J. R. Grace, and M. E. Weber. *Bubbles, drops, and particles.* Courier Corporation, 2005, isbn: 9781306324786.

[24] R. N. Dahms, G. A. Paczko, S. A. Skeen, and L. M. Pickett. Understanding the ignition mechanism of high-pressure spray flames. *Proceedings of the Combustion Institute*, 36(2):2615 – 2623, 2017.

[25] J. M. Desantes, J. J. Lopez, J. M. Garcia-Oliver, and D. Lopez-Pintor. Experimental validation and analysis of seven different chemical kinetic mechanisms for n-dodecane using a rapid compression-expansion machine. *Combustion and Flame*, 182:76 – 89, 2017.

[26] K. Domelevo and L. Sainsaulieu. A numerical method for the computation of the dispersion of a cloud of particles by a turbulent gas flow field. *Journal of Computational Physics*, 133(2):256 – 278, 1997.

[27] D. Dovizio and C. Devaud. Doubly Conditional Source-term Estimation (DCSE) for the modelling of turbulent stratified V-shaped flame. *Combustion and Flame*, 172, 10, 2016.

[28] L. J. W. Dovizio D. and D. C. B. Doubly Conditional Source-term Estimation (DCSE) applied to a series of lifted turbulent jet flames in cold air. *Combustion and Flame*, 162(5), 05, 2015.

[29] F. Ducros, P. Comte, and M. Lesieur. Large-eddy simulation of transition to turbulence in a boundary layer spatially developing over a flat plate. *Journal of Fluid Mechanics*, 326:1, 1996.

[30] P. Ducros, V. Ferrand, F. Nicoud, D. Darracq, and T. Poinsot. Large-eddy simulation of shock/turbulence interaction. *Journal of Computational Physics*, 152:517, 1999.

[31] U. Egüz, S. Ayyapureddi, C. Bekdemir, B. Somers, and P. de Goey. Modeling fuel spray auto-ignition using the fgm approach: Effect of tabulation method. *SAE Technical Paper, 2012-01-0157*, 04, 2012.

[32] U. Egüz, S. Ayyapureddi, C. Bekdemir, B. Somers, and P. de Goey. Manifold resolution study of the FGM method for an igniting diesel spray. *Fuel*, 113:228–238, 2013.

[33] M. Fairweather and R. Woolley. First- and second-order elliptic conditional moment closure calculations of piloted methane diffusion flames. *Combustion and Flame*, 150(1–2):92 – 107, 2007.

[34] X. Fang, R. Ismail, and M. Davy. A study on kinetic mechanisms of diesel fuel surrogate n-dodecane for the simulation of combustion recession. *SAE Technical Paper, 2019-01-0202*, 04, 2019.

[35] X. Fang, R. Ismail, M. H. Davy, and J. Camm. Numerical studies of combustion recession on ECN diesel Spray A. *ASME. Internal Combustion Engine Division Fall Technical Conference*, 2018-9597.

[36] C. Felsch, M. Gauding, C. Hasse, S. Vogel, and N. Peters. An extended flamelet model for multiple injections in DI Diesel engines . *Proceedings of the Combustion Institute*, 32(2):2775 – 2783, 2009.

[37] J. H. Frank, S. A. Kaiser, and M. B. Long. Reaction-rate, mixture-fraction, and temperature imaging in turbulent methane/air jet flames. *Proceedings of the Combustion Institute*, 29(2):2687–2694, 2002.

[38] L. L. Franke, A. K. Chatzopoulos, and S. Rigopoulos. Tabulation of combustion chemistry via artificial neural networks (ANNs): Methodology and application to LES-PDF simulation of sydney flame L. *Combustion and Flame*, 185:245 – 260, 2017.

[39] C. Fureby. Towards large eddy simulations of flows in complex geometries. *AIAA paper 98–2806*, 1998.

[40] O. Gicquel, N. Darabiha, and D. Thevenin. Laminar premixed hydrogen/air counterflow flame simulations using flame prolongation of ILDM with differential diffusion. *Proceedings of the Combustion Institute*, 28:1901–1908, 2000.

[41] D. T. Gillespie. Exact stochastic simulation of coupled chemical reactions. *The Journal of Physical Chemistry*, 81(25):2340–2361, 1977.

[42] S. S. Girimaji. Assumed β-pdf model for turbulent mixing: Validation and extension to multiple scalar mixing. *Combustion Science and Technology*, 78(4-6):177–196, 1991.

[43] G. Godsave. Studies of the combustion of drops in a fuel spray—the burning of single drops of fuel. *Proceedings of the Combustion Institue*, 4(1):818–830, 1953.

[44] R. W. Grout, W. K. Bushe, and C. Blair. Predicting the ignition delay of turbulent methane jets using conditional source-term estimation. *Combustion Theory and Modelling*, 11(6):1009–1028, 2007.

[45] C. Habchi and G. Bruneaux. LES and Experimental investigation of Diesel sprays. 01, 2012.

[46] K. Han and K. Y. Huh. First and second order lagrangian conditional moment closure method in turbulent nonpremixed flames. *Proceedings of the Combustion Institute*, 35(2), 2015.

[47] Z. Han and R. D. Reitz. Turbulence modeling of internal combustion engines using rng k-epsilon models. *Combustion Science and Technology*, 106(4-6):267–295, 1995.

[48] P. C. Hansen. Numerical tools for analysis and solution of fredholm integral equations of the first kind. *Inverse Problems*, 8(6):849, 1992.

[49] R. Hasegawa and H. Yanagihara. HCCI Combustion in DI Diesel Engine. *SAE Technical Paper, 2003-01-0745*, 03, 2003.

[50] C. Hollmann and E. Gutheil. Modeling of turbulent spray diffusion flames including detailed chemistry. *Symposium (International) on Combustion*, 26(1):1731 – 1738, 1996.

[51] J. Huang. *Natural gas combustion under engine-relevant conditions.* PhD thesis, University of British Columbia,01, 2006.

[52] K. Y. Huh and A. Gosman. A phenomenological model of diesel spray atomization. *Proc. Int. Conf. on Multiphase Flows*, 1991.

[53] K. Jansen. Large-eddy simulation of flow around a NACA 4412 airfoil using unstructured grids. *Stanford University Center for Turbulence Research, Annual Research Briefs*, page 225, 1996.

[54] D. Jarrahbashi, S. Kim, and C. Genzale. Simulation of combustion recession after end-of-injection at diesel engine conditions. *Journal of Engineering for Gas Turbines and Power*, 139, 03 2017.

[55] D. Jarrahbashi, S. Kim, B. W. Knox, and C. L. Genzale. Computational analysis of end-of-injection transients and combustion recession. *International Journal of Engine Research*, 0(0):1468087417701280, 0.

[56] H. J. Kaltenbach. Large-eddy simulation of flow around an airfoil on a structured mesh. center for turbulence research. *Stanford University Center for Turbulence Research, Annual Research Briefs*, page 51, 1995.

[57] J. C. Keck and D. Gillespie. Rate-controlled partial-equilibrium method for treating reacting gas mixtures. *Combustion and Flame*, 17(2):237 – 241, 1971.

[58] N. Kim, K. Jung, and Y. Kim. Multi-environment PDF modeling for n-dodecane spray combustion processes using tabulated chemistry. *Combustion and Flame*, 192:205 – 220, 2018.

[59] S. Kim, D. Jarrahbashi, and C. Genzale. The role of turbulent-chemistry interaction in simulating end-of-injection combustion transients in diesel sprays. *SAE Technical Paper, 2017-01-0838*, 03, 2017.

[60] S. Kimura, O. Aoki, H. Ogawa, S. Muranaka, and Y. Enomoto. New Combustion Concept for Ultra-Clean and High-Efficiency Small DI Diesel Engines. *SAE Technical Paper, 1999-01-3681*, 10, 1999.

[61] A. Klimenko and R. Bilger. Conditional moment closure for turbulent combustion. *Progress in Energy and Combustion Science*, 25(6), 1999.

[62] A. Y. Klimenko. Multicomponent diffusion of various admixtures in turbulent flow. *Fluid Dynamics*, 25(3):327–334, 1990.

[63] B. Knox and C. Genzale. Effects of End-of-Injection Transients on Combustion Recession in Diesel Sprays. *SAE Int. J. Engines, 2016-01-0745*, 9(2):932–949, 01, 2016.

[64] B. Knox, C. Genzale, L. Pickett, and J. Garcia-Oliver. Combustion Recession after End of Injection in Diesel Sprays. *SAE Int. J. Engines 2015-01-0797*, 8(2), 2015.

[65] C. Koci, G. Martin, T. Bazyn, and W. Morrison. The Influence of Diesel End-of-Injection Rate Shape on Combustion Recession. *SAE Int. J. Engines 2015-01-0795*, 8(2), 2015.

[66] S. Kook, C. Bae, P. C. Miles, D. Choi, and L. M. Pickett. The influence of charge dilution and injection timing on low-temperature diesel combustion and emissions. *SAE Technical Paper, 2005-01-3837*, 10, 2005.

[67] A. Krisman, E. R. Hawkes, M. Talei, A. Bhagatwala, and J. H. Chen. A direct numerical simulation of cool-flame affected autoignition in diesel engine-relevant conditions. *Proceedings of the Combustion Institute*, 36(3):3567 – 3575, 11, 2016.

[68] A. Kronenburg. Double conditioning of reactive scalar transport equations in turbulent nonpremixed flames. *Physics of Fluids*, 16(7):2640–2648, 2004.

[69] A. Kronenburg, R. Bilger, and J. Kent. Modeling soot formation in turbulent methane–air jet diffusion flames. *Combustion and Flame*, 121(1–2):24 – 40, 2000.

[70] P. Kundu, M. M. Ameen, and S. Som. Importance of turbulence-chemistry interactions at low temperature engine conditions. *Combustion and Flame*, 183:283 – 298, 2017.

[71] J. Labahn and C. Devaud. Investigation of conditional source-term estimation applied to a non-premixed turbulent flame. *Combustion Theory and Modelling*, 17(5):960–982, 2013.

[72] F. Leach, M. Davy, A. Weall, and B. Cooper. Comparing the effect of a swirl flap and asymmetric inlet valve opening on a light duty diesel engine. *SAE Technical Paper, 2017-01-2429*, 10, 2017.

[73] A. M. Lippert, S. Chang, S. Are, and D. P. Schmidt. Mesh independence and adaptive mesh refinement for advanced engine spray simulations. *SAE Technical Paper, 2005-01-0207*, 04, 2005.

[74] F. Liu. A robust and accurate algorithm of the β-pdf integration and its application to turbulent methane-air diffusion combustion in a gas turbine combustor simulator. *International journal of thermal sciences*, 41(8):763–772, 2002.

[75] T. Lu and C. K. Law. A criterion based on computational singular perturbation for the identification of quasi steady state species: A reduced mechanism for methane oxidation with NO chemistry . *Combustion and Flame*, 154(4):761 – 774, 2008.

[76] Z. Luo, S. Som, S. M. Sarathy, M. Plomer, W. J. Pitz, D. E. Longman, and T. Lu. Development and validation of an n-dodecane skeletal mechanism for spray combustion applications. *Combustion Theory and Modelling*, 18(2):187–203, 2014.

[77] U. Maas and S. B. Pope. Implementation of simplified chemical kinetics based on intrinsic low-dimensional manifolds. *Symposium (International) on Combustion*, 24(1):103 – 112, 1992.

[78] U. Maas and S. B. Pope. Simplifying chemical kinetics: Intrinsic low-dimensional manifolds in composition space. *Combustion and Flame*, (88):239 – 64, 1992.

[79] U. Maas and S. B. Pope. Simplifying chemical kinetics: Trajectory generated low-dimensional manifolds. *Combustion and Flame*, 1992.

[80] N. Maes, M. Meijer, N. Dam, B. Somers, H. B. Toda, G. Bruneaux, S. A. Skeen, L. M. Pickett, and J. Manin. Characterization of spray a flame structure for parametric variations in ecn constant-volume vessels using chemiluminescence and laser-induced fluorescence. *Combustion and Flame*, 174:138 – 151, 2016.

[81] A. Masri, R. Dibble, and R. Barlow. The structure of turbulent nonpremixed flames of methanol over a range of mixing rates. *Combustion and Flame*, 89(2):167 – 185, 1992.

[82] E. Mastorakos. Ignition of turbulent non-premixed flames. *Progress in Energy and Combustion Science*, 35(1):57 – 97, 2009.

[83] F. Mauß, D. Keller, and N. Peters. A lagrangian simulation of flamelet extinction and re-ignition in turbulent jet diffusion flames. *Symposium (International) on Combustion*, 23(1):693 – 698, 1991.

[84] M. Meijer and L. Somers. Engine Combustion Network: "Spray A" basic measurements and advanced diagnostics. *Proceedings of the 12th International Conference on Liquid Atomization and Spray Systems, ICLASS 2012*, 09.

[85] S. Menon, P.-K. Yeung, and W.-W. Kim. Effect of subgrid models on the computed interscale energy transfer in isotropic turbulence. *Computers and Fluids*, 25(2):165 – 180, 1996.

[86] M. P. B. Musculus and K. Kattke. Entrainment waves in diesel jets. *SAE Int. J. Engines 2009-01-1355*, 2:1170–1193, 04 2009.

[87] M. P. B. Musculus, T. Lachaux, L. M. Pickett, and C. A. Idicheria. End-of-injection over-mixing and unburned hydrocarbon emissions in low-temperature-combustion diesel engines. *SAE Technical Paper, 2007-01-0907*, 04, 2007.

[88] J. D. Naber and D. L. Siebers. Effects of gas density and vaporization on penetration and dispersion of diesel sprays. *SAE Technical Paper*, 02, 1996.

[89] J. Nafe and U. Maas. A general algorithm for improving ildms. *Combustion Theory and Modelling*, 6(4):697–709, 2002.

[90] S. Navarro-Martinez and A. Kronenburg. Flame stabilization mechanisms in lifted flames. *Flow, Turbulence and Combustion*, 87(2):377–406, 10, 2011.

[91] L. Nicholson, X. Fang, J. Camm, M. Davy, and D. Richardson. Comparison of transient diesel spray break-up between two computational fluid dynamics codes. *SAE Technical Paper, 2018-01-0307*, 04, 2018.

[92] T. Nishimura, K. Satoh, S. Takahashi, and K. Yokota. Effects of fuel injection rate on combustion and emission in a di diesel engine. *SAE Technical Paper*, 08, 1998.

[93] P. O Rourke. *Collective drop effects on vaporizing liquid sprays.* Nov 1981.

[94] J. V. Oijen and L. D. Goey. Modelling of premixed laminar flames using flamelet-generated manifolds. *Combustion Science and Technology*, 161(1):113–137, 2000.

[95] P. J. O'Rourke and A. A. Amsden. The TAB method for numerical calculation of spray droplet breakup, 1987.

[96] S. S. Pandurangi, M. Bolla, Y. M. Wright, K. Boulouchos, S. A. Skeen, J. Manin, and L. M. Pickett. Onset and progression of soot in high-pressure n-dodecane sprays under diesel engine conditions. *International Journal of Engine Research*, 18(5-6):436–452, 2017.

[97] M. A. Patterson and R. D. Reitz. Modeling the effects of fuel spray characteristics on diesel engine combustion and emission. *SAE Technical Paper, 980131*, 1998.

[98] S. Patwardhan, S. De, K. Lakshmisha, and B. Raghunandan. CMC simulations of lifted turbulent jet flame in a vitiated coflow. *Proceedings of the Combustion Institute*, 32(2):1705 – 1712, 2009.

[99] Y. Pei, S. Som, E. Pomraning, P. K. Senecal, S. A. Skeen, J. Manin, and L. M. Pickett. Large eddy simulation of a reacting spray flame with multiple realizations under compression ignition engine conditions. *Combustion and Flame*, 162(12):4442 – 4455, 2015.

[100] N. Peters. Laminar diffusion flamelet models in non-premixed turbulent combustion. *Progress in Energy and Combustion Science*, 10(3):319 – 339, 1984.

[101] N. Peters. Laminar flamelet concepts in turbulent combustion. *Symposium (International) on Combustion*, 21(1):1231 – 1250, 1988.

[102] N. Peters and R. Kee. The computation of stretched laminar methane-air diffusion flames using a reduced four-step mechanism. *Combustion and Flame*, 68(1):17 – 29, 1987.

[103] L. Pickett and G. Bruneaux. Engine combustion network. Combustion Research Facility, Sandia National Laboratories, Livermore, CA. *See http://www. sandia. gov/ECN*, 2018.

[104] L. M. Pickett. Introducing the engine combustion network. *International Multidimensional Engine Modeling Users Group Meeting*, 2008.

[105] L. M. Pickett, C. L. Genzale, G. Bruneaux, L.-M. Malbec, L. Hermant, C. Christiansen, and J. Schramm. Comparison of diesel spray combustion in different high-temperature, high-pressure facilities. *SAE Int. J. Engines, 2010-01-2106*, 3:156–181, 10, 2010.

[106] L. M. Pickett, S. Kook, H. Persson, and Öivind Andersson. Diesel fuel jet lift-off stabilization in the presence of laser-induced plasma ignition. *Proceedings of the Combustion Institute*, 32(2):2793 – 2800, 2009.

[107] L. M. Pickett, J. Manin, C. L. Genzale, D. L. Siebers, M. P. B. Musculus, and C. A. Idicheria. Relationship between diesel fuel spray vapor penetration/dispersion and local fuel mixture fraction. *SAE Int. J. Engines 2011-01-0686*, 4:764–799, 04, 2011.

[108] M. Pilch and C. Erdman. Use of breakup time data and velocity history data to predict the maximum size of stable fragments for acceleration-induced breakup of a liquid drop. *International journal of multiphase flow*, 13(6):741–757, 1987.

[109] T. Poinsot and D. Veynante. *Theoretical and Numerical Combustion.* R.T. Edwards, 2001, isbn:9781930217058.

[110] E. Pomraning, K. Richards, and P. K. Senecal. Modeling turbulent combustion using a rans model, detailed chemistry, and adaptive mesh refinement. *SAE Technical Paper, 2014-01-1116*, 04, 2014.

[111] S. B. Pope. The probability approach to the modelling of turbulent reacting flows. *Combustion and Flame*, 27:299 – 312, 1976.

[112] S. B. Pope. PDF methods for turbulent reactive flows. *Progress in Energy and Combustion Science*, 11(2):119 – 192, 1985.

[113] S. B. Pope. Computationally efficient implementation of combustion chemistry using in situ adaptive tabulation. *Combustion Theory and Modelling*, 1(1):41–63, 1997.

[114] S. B. Pope. Turbulent flows. *Measurement Science and Technology*, 12(11):2020, 2001.

[115] W. Ranz and W. Marshall. Evaporation from drops. *Chemical Engineering Progress*, 48(3):141–146, 1952.

[116] E. Ranzi, A. Frassoldati, A. Stagni, M. Pelucchi, A. Cuoci, and T. Faravelli. Reduced kinetic schemes of complex reaction systems: Fossil and biomass-derived transportation fuels. *International Journal of Chemical Kinetics*, 46(9):512–542, 07, 2014.

[117] R. D. Reitz and R. Diwakar. Effect of drop breakup on fuel sprays. *SAE Technical Paper, 860469*, 1986.

[118] R. D. Reitz and R. Diwakar. Structure of high-pressure fuel sprays. *SAE Technical Paper, 870598*, 1987.

[119] Z. Ren, S. B. Pope, A. Vladimirsky, and J. M. Guckenheimer. The invariant constrained equilibrium edge preimage curve method for the dimension reduction of chemical kinetics. *The Journal of Chemical Physics*, 124(11):114111, 2006.

[120] M. Ruger, S. Hohmann, M. Sommerfeld, and G. Kohnen. Euler/lagrange calculations of turbulent sprays: The effect of droplet collisions and coalescence. *Atomization and Sprays*, 10(1), 2000.

[121] R. Saad and R. Borghi. A simulation with a “cellular automaton” for turbulent combustion modelling. *Symposium (International) on Combustion*, 22(1):569 – 577, 1989.

[122] A. E. Sayed and C. B. Devaud. Conditional Moment Closure (CMC) applied to autoignition of high pressure methane jets in a shock tube. *Combustion Theory and Modelling*, 12(5):943–972, 2008.

[123] D. P. Schmidt and C. Rutland. A new droplet collision algorithm. *Journal of Computational Physics*, 164(1):62 – 80, 2000.

[124] D. P. Schmidt and P. K. Senecal. Improving the numerical accuracy of spray simulations. *SAE Technical Paper, 2002-01-1113*, 03, 2002.

[125] P. Schroll, A. Wandel, R. Cant, and E. Mastorakos. Direct numerical simulations of autoignition in turbulent two-phase flows. *Proceedings of the Combustion Institute*, 32(2):2275 – 2282, 2009.

[126] P. Senecal, E. Pomraning, K. Richards, and S. Som. Grid Convergent Spray Models for Internal Combustion Engine CFD Simulations, 09, 2012.

[127] P. Senecal, E. Pomraning, Q. Xue, S. Som, S. Banerjee, B. Hu, K. Liu, and J. Deur. Large eddy simulation of vaporizing sprays considering multi-injection averaging and grid-convergent mesh resolution. *Journal of Engineering for Gas Turbines and Power*, 136(11):111504, 2014.

[128] P. K. Senecal, E. Pomraning, K. J. Richards, T. E. Briggs, C. Y. Choi, R. M. McDavid, and M. A. Patterson. Multi-dimensional modeling of direct-injection diesel spray liquid length and flame lift-off length using cfd and parallel detailed chemistry. *SAE Technical Paper, 2003-01-1043*, 03, 2003.

[129] P. K. Senecal, K. J. Richards, E. Pomraning, T. Yang, M. Z. Dai, R. M. McDavid, M. A. Patterson, S. Hou, and T. Shethaji. A new parallel cut-cell cartesian cfd code for rapid grid generation applied to in-cylinder diesel engine simulations. *SAE Technical Paper, 2007-01-0159*, 04, 2007.

[130] H. K. Seung, Y. H. Kang, and W. B. Robert. Second-order conditional moment closure modeling of local extinction and reignition in turbulent non-premixed hydrocarbon flames. *Proceedings of the Combustion Institute*, 29(2):2131 – 2137, 2002.

[131] T.-H. Shih, W. W. Liou, A. Shabbir, Z. Yang, and J. Zhu. A new k-ϵ eddy viscosity model for high reynolds number turbulent flows. *Computers and Fluids*, 24(3):227 – 238, 1995.

[132] D. L. Siebers and B. Higgins. Flame lift-off on direct-injection diesel sprays under quiescent conditions. *SAE Technical Paper, 2001-01-0530*, 03, 2001.

[133] M. J. Skeen, S. and L. Pickett. Visualization of Ignition Processes in High-Pressure Sprays with Multiple Injections of n-Dodecane. *SAE Int. J. Engines 2015-01-0799*, 8(2), 01 2015.

[134] S. A. Skeen, J. Manin, and L. M. Pickett. Simultaneous formaldehyde PLIF and high-speed schlieren imaging for ignition visualization in high-pressure spray flames. *Proceedings of the Combustion Institute*, 35(3):3167 – 3174, 2015.

[135] S. Som, G. D'Errico, D. Longman, and T. Lucchini. Comparison and standardization of numerical approaches for the prediction of non-reacting and reacting diesel sprays. *SAE Technical Paper, 2012-01-1263*, 04, 2012.

[136] D. B. Spalding. Mixing and chemical reaction in steady confined turbulent flames. *Symposium (International) on Combustion*, 13:649–657, 1971.

[137] D. B. Spalding. Development of the eddy-break-up model of turbulent combustion. *Symposium (International) on Combustion*, 16(1):1657–1663, 1977.

[138] C. Speziale. Turbulence Modeling for Time-Dependent RANS and VLES: A Review. *AIAA Journal*, 36:173 – 184, 1998.

[139] G. Stahl and J. Warnatz. Numerical investigation of time-dependent properties and extinction of strained methane and propane-air flamelets. *Combustion and Flame*, 85(3-4):285–299, 1991.

[140] H. Steiner and W. K. Bushe. Large eddy simulation of a turbulent reacting jet with conditional source-term estimation. *Physics of Fluids*, 13(3):754–769, 2001.

[141] J. C. Sutherland and A. Parente. Combustion modeling using principal component analysis. *Proceedings of the Combustion Institute*, 32(1):1563 – 1570, 2009.

[142] F. Tanner. Liquid jet atomization and droplet breakup modeling of non-evaporating diesel fuel sprays. *SAE Technical Paper, 970050*, 1997.

[143] F. Tanner and G. Weisser. Simulation of liquid jet atomization for fuel sprays by means of a cascade drop breakup model. Technical report, SAE Technical Paper, 1998.

[144] F. X. Tanner. Development and validation of a cascade atomization and drop breakup model for high-velocity dense sprays. *Atomization and sprays*, 14(3), 2004.

[145] J. Tillou, J.-B. Michel, C. Angelberger, and D. Veynante. Assessing les models based on tabulated chemistry for the simulation of diesel spray combustion. *Combustion and Flame*, 161(2):525 – 540, 2014.

[146] S. Tonini, M. Gavaises, and A. Theodorakakos. Modelling of high-pressure dense diesel sprays with adaptive local grid refinement. *International Journal of Heat and Fluid Flow*, 29(2):427 – 448, 2008.

[147] H. P. Tsui and W. K. Bushe. Conditional source-term estimation using dynamic ensemble selection and parallel iterative solution. *Combustion Theory and Modelling*, 20(5):812–833, 2016.

[148] A. Vallet, A. A. Burluka, and R. Borghi. Development of a eulerian model for the atomization of a liquid jet. *Atomization and Sprays*, 11(6), 2001.

[149] S. Vasu, D. Davidson, Z. Hong, V. Vasudevan, and R. Hanson. n-dodecane oxidation at high-pressures: Measurements of ignition delay times and oh concentration time-histories. *Proceedings of the Combustion Institute*, 32(1):173 – 180, 2009.

[150] D. Veynante and L. Vervisch. Turbulent combustion modeling. *Progress in Energy and Combustion Science*, 28(3):193 – 266, 2002.

[151] A. S. T. W. L. Jeffrey, B. D. Cecile and K. J. Daun. Inverse analysis and regularisation in conditional source-term estimation modelling. *Combustion Theory and Modelling*, 18(3):474–499, 2014.

[152] Y. P. Wan, H. Pitsch, and N. Peters. Simulation of autoignition delay and location of fuel sprays under diesel-engine relevant conditions. *SAE Technical Paper, 971590*, 05, 1997.

[153] B. L. Wang, M. J. Bergin, B. R. Petersen, P. C. Miles, R. D. Reitz, and Z. Han. Validation of the generalized rng turbulence model and its application to flow in a hsdi diesel engine. *SAE Technical Paper, 2012-01-0140*, 04, 2012.

[154] H. Wang, K. Luo, and J. Fan. Direct numerical simulation and CMC (conditional moment closure) sub-model validation of spray combustion. *Energy*, 46(1):606–617, 2012.

[155] M. Wang, A. Frisque, J. Huang, and W. K. Bushe. Trajectory generated low-dimensional manifolds generated using the stochastic particle model. *Combustion Theory and Modelling*, 12(2):249–267, 2008.

[156] M. Wang, J. Huang, and W. K. Bushe. Simulation of a turbulent non-premixed flame using conditional source-term estimation with trajectory generated low-dimensional manifold. *Proceedings of the Combustion Institute*, 31(2):1701 – 1709, 2007.

[157] Y. Wang and C. Rutland. Direct numerical simulation of ignition in turbulent n-heptane liquid-fuel spray jets. *Combustion and Flame*, 149(4):353 – 365, 2007.

[158] H. J. Wang M. and W. K. Bushe. Simulation of a turbulent non-premixed flame using conditional source-term estimation with trajectory generated low-dimensional manifold. *Proceedings of the Combustion Institute*, 31(2):1701 – 1709, 2007.

[159] A. Wehrfritz, O. Kaario, V. Vuorinen, and B. Somers. Large eddy simulation of n-dodecane spray flames using flamelet generated manifolds. *Combustion and Flame*, 167:113 – 131, 2016.

[160] C. K. Westbrook, W. J. Pitz, O. Herbinet, H. J. Curran, and E. J. Silke. A comprehensive detailed chemical kinetic reaction mechanism for combustion of n-alkane hydrocarbons from n-octane to n-hexadecane. *Combustion and Flame*, 156(1):181 – 199, 2009.

[161] Y. M. Wright, M. Bolla, K. Boulouchos, G. Borghesi, and E. Mastorakos. Conditional moment closure for two-phase flows – a review of recent devel-

opments and application to various spray combustion configurations. *AIP Conference Proceedings*, 1642(1):433–440, 2015.

[162] Y. M. Wright, O. Margari, K. Boulouchos, G. De Paola, and E. Mastorakos. Experiments and simulations of n-heptane spray auto-ignition in a closed combustion chamber at diesel engine conditions. *Flow, Turbulence and Combustion*, 84(1):49–78, 2010.

[163] J. Xin, L. Ricart, and R. Reitz. Computer modeling of diesel spray atomization and combustion. *Combustion science and technology*, 137(1-6):171–194, 1998.

[164] Q. Xue, W. Som, P. Senecal, and E. Pomraning. A study of grid resolution and sgs models for les under non-reacting spray conditions. *25th Annual Conference on Liquid Atomization and Spray Systems, Pittsburgh, PA*, 2013.

[165] V. Yakhot, S. A. Orszag, S. Thangam, T. B. Gatski, and C. G. Speziale. Development of turbulence models for shear flows by a double expansion technique. *Physics of Fluids A: Fluid Dynamics*, 4(7):1510–1520, 1992.

[166] T. Yao, Y. Pei, B. Zhong, S. Som, and T. Lu. A Hybrid Mechanism for n-Dodecane Combustion with Optimized Low-Temperature Chemistry. *9th US National Combustion Meeting*, 05, 2015.

[167] T. Yao, Y. Pei, B. J. Zhong, S. Som, T. Lu, and K. H. Luo. A compact skeletal mechanism for n-dodecane with optimized semi-global low-temperature chemistry for diesel engine simulations. *Fuel*, 191:339 – 349, 2017.

[168] A. Yoshizawa and K. Horiuti. A statistically-derived subgrid-scale kinetic energy model for the large-eddy simulation of turbulent flows. *Journal of the Physical Society of Japan*, 54(8):2834–2839, 1985.

[169] X. You, F. N. Egolfopoulos, and H. Wang. Detailed and simplified kinetic models of n-dodecane oxidation: The role of fuel cracking in aliphatic hydrocarbon combustion. *Proceedings of the Combustion Institute*, 32(1):403 – 410, 2009.

[170] R. C. Yu, T.-W. Kuo, S. M. Shahed, and T. W. Chang. The Effect of Mixing Rate, End of Injection, and Sac Volume on Hydrocarbon Emissions from a D.I. Diesel Engine. *SAE Technical Paper, 831294*, 09, 1983.

[171] P. Zhao and C. K. Law. The role of global and detailed kinetics in the first-stage ignition delay in NTC-affected phenomena. *Combustion and Flame*, 160(11):2352 – 2358, 2013.